Superconducting islands and gate-based readout in semiconductor nanowires

van Veen, Jasper

DOI
10.4233/uuid:ebfff02c-f87c-4c8a-9edd-53adb12f4403

Publication date
2019

Document Version
Final published version

Citation (APA)
van Veen, J. (2019). *Superconducting islands and gate-based readout in semiconductor nanowires*. [Dissertation (TU Delft), Delft University of Technology]. https://doi.org/10.4233/uuid:ebfff02c-f87c-4c8a-9edd-53adb12f4403

Superconducting islands and gate-based readout in semiconductor nanowires

Superconducting islands and gate-based readout in semiconductor nanowires

Proefschrift

ter verkrijging van de graad van doctor
aan de Technische Universiteit Delft,
op gezag van de Rector Magnificus prof. dr. ir. T.H.J.J. van der Hagen,
voorzitter van het College voor Promoties,
in het openbaar te verdedigen op donderdag 6 juni 2019 om 15:00 uur

door

Jasper VAN VEEN

Natuurkundig ingenieur, Technische Universiteit Delft, Nederland
geboren te Berkel en Rodenrijs, Nederland

Dit proefschrift is goedgekeurd door de promotoren.

Samenstelling promotiecommissie:

Rector Magnificus,	voorzitter
prof. dr. ir. L.P. Kouwenhoven	Technische Universiteit Delft, promotor
Dr. S. Goswami	Technische Universiteit Delft, copromotor

Onafhankelijke leden:

Prof. dr. ir. T. H. Oosterkamp	Universiteit Leiden
Prof. dr. L. DiCarlo	Technische Universiteit Delft
Dr. M. Blaauboer	Technische Universiteit Delft
Dr. ir. M. Veldhorst	Technische Universiteit Delft
Prof. dr. ir. L. M. K. Vandersypen	Technische Universiteit Delft, reservelid

Overige leden:

Prof. dr. J. Nygård	University of Copenhagen, Denmark

Geprint door Gildeprint, omslag door Jip Pijs

Casimir PhD Series, Delft-Leiden 2019-17, ISBN 978-90-8593-403-5

An electronic version of this dissertation is available at
http://repository.tudelft.nl/.

I do know that everything is interesting if you go into it deeply enough

Richard Feynman

Contents

Summary

Quantum computers can solve some problems exponentially faster than classical computers. Unfortunately, the computational power of quantum computers is currently limited by the number of working qubits. It is difficult to scale up these systems, because qubits are easily affected by noise in their environment. This noise leads to decoherence: loss of the qubit's encoded information. A possible solution to diminish decoherence is using Majorana box qubits, as these qubits are predicted to be insensitive to local noise. However, this promising type of qubit does not exist yet.

With the research described in this thesis, we aim to contribute to the development of Majorana box qubits (MBQs). In these qubits, Majorana zero modes, the basic elements of MBQs, are contained within a superconducting island to suppress Majorana parity fluctuations caused by quasiparticle poisoning. To enable parity readout of the MBQ, these modes are coupled to quantum dots within a nanowire network. To help realize MBQs, we need a better understanding of quasiparticles in superconducting islands, parity-readout techniques, and ways to fabricate nanowire networks. These three aspects are the focus of the experiments presented in this thesis.

To study superconducting islands and readout techniques, we used InAs semiconductor nanowires with an epitaxially grown Al shell. Majorana signatures have already been observed in such nanowires. We addressed quasiparticle dynamics in superconducting islands by measuring the gate-charge modulation of the switching current. We found a consistent $2e$-periodic modulation at zero magnetic field, and an exponential decrease of parity lifetime with increasing magnetic field. We explored MBQ readout, using a quantum dot level as a proxy for a Majorana zero mode, and measured its charge hybridization with another dot using gate-based readout. We showed that we can rapidly discriminate between two settings with different tunnel couplings, demonstrating the potential of gate-based readout to measure MBQs. And, using gate-based readout, we could study charge-transfer processes occurring in hybrid structures of superconducting islands coupled to quantum dots.

Finally, to find a good material platform for nanowire networks, we characterized two two-dimensional systems. We realized quantum point contacts in InSb, which we used to measure the g-factor anisotropy, and effective electron mass in this system. And, we studied the spin-orbit interaction in InAs/GaSb by extracting the difference in density between electrons with different spin orientations.

This thesis finishes with a proposal for a series experiments to realize MBQs. These experiments make use of superconducting islands and the reflectometry setup we developed for gate-based readout.

Samenvatting

Kwantumcomputers zouden sommige problemen exponentieel sneller kunnen oplossen dan klassieke computers. Helaas wordt de rekenkracht van kwantumcomputers momenteel beperkt door het aantal werkende kwantumbits. Het is moeilijk om deze kleine kwantumprocessoren op te schalen, omdat kwantumbits gemakkelijk worden verstoord door ruis in hun omgeving. Die ruis leidt tot decoherentie: het verlies van de opgeslagen kwantuminformatie. Een mogelijke oplossing om decoherentie te verminderen zijn Majorana-box-kwantumbits (MBQs), omdat dit type kwantumbit ongevoelig lijkt te zijn voor lokale ruis. Deze veelbelovende kwantumbit bestaat echter nog niet.

Met het onderzoek in dit proefschrift willen we bijdragen aan de ontwikkeling van MBQs. In deze kwantumbits worden Majoranapariteitsschommelingen (veroorzaakt door vervuiling met quasideeltjes) tegengegaan doordat Majoranatoestanden zich op een supergeleidend eiland bevinden. Door een netwerk van nanodraden zijn de Majoranatoestanden gekoppeld aan kwantumdots, wat het mogelijk maakt om hun pariteit uit te lezen. Om MBQs te helpen realiseren is een beter begrip nodig van quasideeltjes in supergeleidende eilanden, pariteitsuitleestechnieken en manieren om een netwerk van nanodraden te maken. Deze drie aspecten worden met de experimenten in dit proefschrift verder onderzocht.

Om supergeleidende eilanden en uitleestechnieken te bestuderen hebben we halfgeleidende, InAs-nanodraden gebruikt die gedeeltelijk zijn bedekt met een dunne laag aluminium. In zulke draden heeft men al aanwijzingen voor Majoranatoestanden waargenomen. We hebben de dynamica van quasideeltjes in supergeleidende eilanden bestudeerd door de modulatie van de transitiestroom door de gatelading te meten. Deze metingen laten een systematische $2e$-periodieke modulatie bij nul magneetveld zien, en een exponentiële afname van de pariteitslevensduur als functie van het magneetveld. Om het uitlezen van MBQs te onderzoeken hebben we een kwantumdottoestand ter vervanging van de Majoranatoestand gebruikt. Door middel van reflectometrie vanaf de gate hebben we de ladingshybridisatie van deze dot met een andere dot gemeten, en laten zien dat we snel onderscheid kunnen maken tussen twee instellingen met verschillende tunnelamplituden. Dit experiment laat de potentie van deze uitleesmethode voor MBQs zien. Met dezelfde methode hebben we ook ladingsoverdrachtprocessen bestudeerd in supergeleidende eilanden gekoppeld aan kwantumdots.

Om een geschikt materiaal voor nanodraadnetwerken te vinden hebben we twee verschillende tweedimensionale systemen gekarakteriseerd. Door kwantumpuntcontacten in InSb te maken hebben we de g-factoranisotropie en de effectieve elektronenmassa in dit systeem weten te meten. Ook hebben we de spin-baaninteractie in InAs/GaSb kunnen bepalen door het verschil in dichtheid te meten tussen elektronen met verschillende spinoriëntaties.

Dit proefschrift sluit af met een voorstel voor een reeks experimenten om verder toe te werken naar MBQs. Deze experimenten maken gebruik van supergeleidende eilanden en de reflectometrie-meettechniek die we hebben ontwikkeld voor dit onderzoek.

1

Introduction

Light bulb

Gru

1.1. Quantum mechanics and computation

At the end of the 19th century, physicists were puzzled by the emission spectra of hot objects, commonly referred to as blackbodies. Their interest in this problem was not purely academic. At that time, better light bulbs were in high demand. However, a method to measure a lightbulb's (absolute) luminosity was not yet available. By solving the blackbody problem, physicists hoped to construct a method to characterise and improve the performance of light bulbs. In 1859, Gustav Kirchhoff had already shown that the emission spectrum only depends on the temperature of the blackbody. But, an equation describing the precise amount of energy emitted at each wavelength was still missing. In 1896, Wilhelm Wien derived an approximate expression, but his formula disagreed with observations at longer wavelengths. Max Planck solved this discrepancy by invoking that light comes in packages of quantized energy. This observation signaled the start of quantum mechanics. Despite his great contributions to this research field, Planck himself later said: "Briefly summarized, what I did can be described as simply an act of desperation." In the next 30 years, quantum theory was further developed by many, now famous, physicists such as Niels Bohr and Erwin Schrödinger [1].

These days, quantum mechanics is a mature theory, and its predictions have been thoroughly tested. Notable experiments include the double-slit experiment with single electrons, demonstrating particle-wave duality [2]; and the Bell test, showing that local hidden variables cannot account for correlations caused by entangled particles [3]. Motivated by these successes, people started thinking about using quantum mechanical systems to process and transmit information. Richard Feynman, for example, vigorously argued to use a quantum computer to efficiently simulate quantum systems. In a lecture, he said: "nature isn't classical, dammit, and if you want to make a simulation of nature, you'd better make it quantum mechanical, and by golly it's a wonderful problem, because it doesn't look so easy" [4]. Quantum computing is, however, not restricted to simulating quantum systems, and can also be used to speed-up certain algorithms. A well-known example is the factoring algorithm found by Peter Shor in 1994 [5]. It can be used to find the prime factors of a large integer much faster than it would take for any classical algorithm. Nowadays, many quantum algorithms have been identified; an up-to-date list can be found in Ref. 6.

Quantum bits, or qubits for short, form the basic elements for these quantum algorithms. Unlike their classical analogues, qubits can be entangled, and be in a superposition of zero and one [8]. Qubits come in many forms including: photons, trap ions and atoms, spins in semiconductor quantum dots or NV centers in diamond, and superconducting circuits [9]. The solid-state variants are particularly interesting as they are compatible with existing microfabrication techniques, and therefore, regarded scalable [10, 11]. However, to-date, the number of qubits is limited to a few tens, not enough to perform useful algorithms. Feynman turned out to be right: building a quantum computer is not easy. One of the main limitations is dephasing of qubits due to interactions with uncontrolled parts of their environment, like nearby charge and spin switchers. In this process, the stored quantum information gets lost. At the same time, qubits cannot be completely shielded

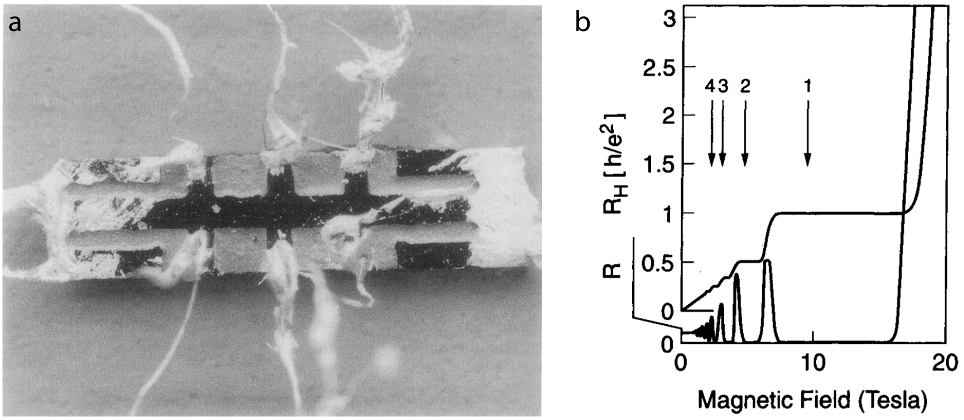

Figure 1.1 – The quantum Hall effect. **a** Micrograph of the Hall bar in which the fractional quantum Hall effect was discovered. **b** Typical magnetic field dependence of the longitudinal (R) and Hall (R_H) resistance. The plateaus in the Hall resistance are so precise that they are now used to define the official resistance standard. Both images are obtained from [7].

from this environment because they need to be controlled and measured. Moreover, measuring and controlling operations themselves can introduce errors in the encoded quantum information. One way to deal with this issue is to use quantum error correction, in which several physical qubits encode one logical qubit. Then, errors can be corrected as long as they occur at low enough rates [12]. Alternatively, qubits and qubit operations can be engineered so that they are robust to noise at a hardware level. This approach relies on topology, and forms the main motivation behind the work presented in this thesis.

1.2. Topologically protecting quantum information

Topology can be used to classify the Hamiltonians of band insulators and superconductors based on their dimensionality and symmetries. A prime example of topology in condensed matter is the quantum Hall effect (QHE), discovered by Klaus von Klitzing in 1980 [13]. It occurs in low-density, two-dimensional systems in a strong perpendicular magnetic field. The hallmark of the QHE is the quantization of the Hall resistance, which is clearly visible in the data shown in Figure 1.1b. The particular sample shown in Figure 1.1a was used for the discovery of the fractional quantum Hall effect. It does not look very clean, which is not so surprising as Horst Störmer said in his Nobel lecture: “The sample was prepared by scratching away parts of semiconducting material with little attention to exact dimensions or tidiness” [7]. Still, the Hall quantization in this sample was measured to an accuracy of a few 10 parts in a billion! Interestingly, this is generally observed, i.e. the quantization is largely insensitive to sample details such as material system, disorder, dimensions and so forth. The underlying reason for this extreme precision is topology.

In a quantum Hall insulator, electrons are transported via edge channels. These edge channels, which result directly from the topology of the sample, are one-way streets; they only conduct in one direction. Electron backscattering is simply not allowed, and hence, the resistance cannot deviate from its quantized value.

Now, one could dream to construct a qubit that is topologically protected against decoherence, just as quantized Hall plateaus are protected against backscattering. To do so, we consider a different topology class; the class of one-dimensional topological superconductors [14]. The elementary quasiparticle excitations in these superconductors are called Majorana modes. These zero energy quasiparticles are their own antiparticle, and are located at the end of the 1D superconductor. Two Majorana modes define one nonlocal fermionic mode which also has zero energy regardless of its occupation, and can be used to encode quantum information. Due to the nonlocal nature of the fermionic modes, local noise cannot perturb the qubit, i.e. the information is topologically protected. As an additional benefit, Majoranas obey non-Abelian statistics upon exchanging them. These exchanges, or braids, can transform the state of the system, and can therefore be used to implement quantum gates. These gates are exact as they only depend on the topology of the braid.

There exist concrete blueprints for realizing topologically protected qubits based on semiconductor nanowires that are proximitized with a conventional superconductor [15–18]. Majorana particles can emerge in this system upon applying a magnetic field [19, 20], and the first Majorana signatures in this system have already been observed [21]. However, to build a Majorana qubit additional elements are needed. Here, we discuss three of these elements based on a proposal known as the Majorana box qubit, see Figure 1.2 [17, 18]. First, the Majoranas are contained within a superconducting island. These islands have finite charging energy E_C, leading to a preferred number of charges on the island, thereby suppressing charge fluctuations. This is useful, because a Majorana qubit loses its quantum information when an additional quasiparticle tunnels into one of the Majoranas, a process known as quasiparticle poisoning. Second, there should be a way to measure the state of the qubit. In a box qubit, this is implemented by coupling a pair of Majoranas to a double quantum dot [17, 18]. In this geometry, interference between tunneling paths leads to a qubit-state-dependent tunnel coupling between the dots. These different tunnel couplings can be measured via gate-based readout using radio frequency waves. Third, for braiding operations a (quasi) 2D system is needed. Such a system can be realized using a nanowire network. For all these aspects, there are open research questions that need to be answered before a Majorana (box) qubit can be realized.

1.3. This thesis

The experiments presented in this thesis relate to the qubit elements discussed above, as a contribution to the realization of Majorana qubits. In the first part of this thesis, we present three experiments using InAs nanowires, focusing on superconducting islands in proximitized, semiconductor nanowires, and gate-based readout of semiconductor quantum dots. In the second part of this thesis, we switch gears to 2D systems, which should allow for fabrication of nanowire networks. We focus

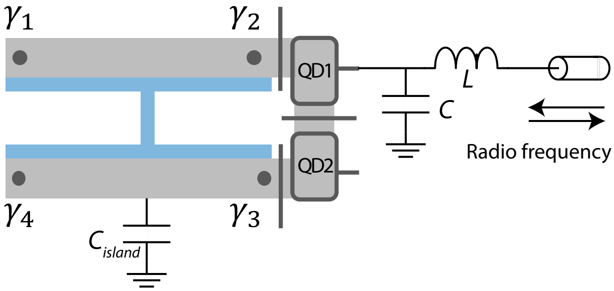

Figure 1.2 – **Elements of a Majorana box qubit.** In this schematic, the semiconductor nanowire network is shown in gray, the conventional superconductor in blue, and the Majoranas $\gamma_1, \dots, \gamma_4$ are indicated with dark gray circles. The Majoranas are contained within a superconducting island which is connected via a small capacitance C_{island} to ground. The readout circuit shown consists of a double quantum dot coupled to a pair of Majoranas, and a LC resonator connected to the gate of one of the dots. This figure is adapted from [17].

on the characterization of these systems for their use as platforms for topological superconductivity.

1.3.1. Thesis outline

In **chapter** 2, we describe the theoretical background of Majoranas in semiconductor nanowires, as well as the building blocks for Majorana box qubits: quantum dots and superconducting islands. We also discuss how these qubits can be readout using quantum dots and gate-based sensing.

In **chapter** 3, we provide the technical details for the nanowire experiments. We describe the reflectometry setup used for the gate-based readout, and the fabrication procedure for the nanowire devices.

In **chapter** 4, we study the switching current modulation of nanowire single-Cooper pair transistors as a function of gate voltage, temperature, and colinear magnetic field. These island devices show a consistent $2e$-periodic switching current, indicating a hard superconducting gap without any low-energy subgap states. At finite field, we do observe subgap states which we study by tracking the length of the even and odd Coulomb valleys.

In **chapter** 5, we use the reflectometry setup to study charge hybridization in a double quantum dot. We show that the frequency shift due to the additional capacitive load follows the theoretical prediction, and demonstrate that we can distinguish between Coulomb blockade and resonance with a signal-to-noise exceeding 2 within 1 µs.

In **chapter** 6, we use gate-based readout to study charge-tunneling between superconducting islands and quantum dots. We find single and two particle processes, depending on the energy scales in the superconducting island.

Next, we characterize two material systems for their use in studying topological quantum states. In **chapter** 7, we study quantum point contacts made from InSb quantum wells. We observe a large g-factor anisotropy, and extract the effective mass from magnetic depopulation of the subbands. In **chapter** 8, we study the zero-field spin-splitting in InAs/GaSb using Shubnikov-de Haas measurements.

Finally, in **chapter** 9, we present a discussion on the available material systems, and describe a series of experiments on the road to a Majorana box qubit.

2

Theory

Tussen de regels buiten de kantlijn,
Hoe anders zou het zijn, hoe anders zou het zijn

Typhoon

In this chapter, we present the theoretical background for our nanowire experiments performed in the context of gate-based readout of Majorana box qubits via quantum dots. We first discuss quasiparticle excitations in superconductors, and Majorana zero modes in semiconductor nanowires (section 2.1). Then, we continue with an in depth discussion of quantum dots, double quantum dots, and superconducting islands (sections 2.2 and 2.3). Lastly, we describe the gate-based readout of Majorana box qubits (sections 2.4 and 2.5).

2.1. Superconductivity and Majorana zero modes

In this section, we describe the basic properties of Majorana zero modes (MZMs); zero energy quasiparticles that emerge in topological superconductors [21–25]. We begin with a general discussion of quasiparticle excitations in s-wave superconductors following the Bogoliubov-de Gennes (BdG) formalism [26, 27]. Then, we use this formalism to show how MZMs can be created in semiconductor nanowires. Lastly, we present an overview of the topological properties of these zero energy quasiparticles.

2.1.1. Bogoliubov-de Gennes formalism of superconductivity

Superconductors are interesting materials as they carry current without dissipation. Moreover, they act as perfect diamagnets, and expel magnetic fields from their interior. Initially, these phenomena were described using effective models such as the London equations and Ginzburg-Landau theory [27]. However, these theories lack a microscopic foundation. Later, Bardeen, Cooper, and Schrieffer formulated a microscopic theory of superconductivity, now known as BCS theory [26–28]. Here, we briefly review this theory in terms of the BdG formalism.

In BCS theory, electrons with opposite momentum and spin interact via (virtual) phonons. To calculate the effect of this interaction on the Fermi sphere, we write down the so-called pairing Hamiltonian using second quantization, where $a^\dagger_{k\sigma}$ ($a_{k\sigma}$) creates (annihilates) an electron with momentum $\hbar k$ and spin-projection σ

$$H = \sum_{k\sigma} \epsilon_k a^\dagger_{k\sigma} a_{k\sigma} + \sum_{k,q} V_{kq} a^\dagger_{q\uparrow} a^\dagger_{-q\downarrow} a_{-k\downarrow} a_{k\uparrow}. \tag{2.1}$$

The first term in this Hamiltonian describes the kinetic energy of the spin-degenerate superconductor. Here, $\epsilon_k = \hbar^2 k^2/2m^* - \mu$ with m^* the effective mass of the electrons in the superconductor and μ the chemical potential of the superconductor. The second term models the phonon-mediated interaction between the electrons, where V_{kq} quantifies the strength of the interaction. This term can be simplified using the mean-field approximation which assumes that the fluctuations of $a^\dagger_{q\uparrow} a^\dagger_{-q\downarrow}$ from its expectation value $\langle a^\dagger_{q\uparrow} a^\dagger_{-q\downarrow}\rangle$ are small. Using this approximation, and neglecting all constant energy terms, Eq. (2.1) reduces to the so-called model Hamiltonian

$$H = \sum_{k\sigma} \epsilon_k a^\dagger_{k\sigma} a_{k\sigma} + \sum_{k} \left(\Delta_k a^\dagger_{k\uparrow} a^\dagger_{-k\downarrow} + \Delta^*_k a_{-k\downarrow} a_{k\uparrow}\right), \tag{2.2}$$

where $\Delta_k = \sum_q V_{kq} \langle a^\dagger_q a^\dagger_{-q}\rangle$ is the pairing function. For a s-wave superconductor, the interaction strength does not depend on momentum and, hence, the pairing function is a constant $\Delta_k = \Delta$. The model Hamiltonian does not conserve the number of particles, however, this is a mere artifact of the mean-field approximation.

To calculate the excitation spectrum, it is convenient to write the model Hamiltonian in the $\left(a_{k\uparrow}, a^\dagger_{-k\downarrow}\right)$ basis which we denote as H_k[1]. The quasiparticle excitation

---

[1] Explicitly, $H_k = \epsilon_k \tau_z + \Delta \tau_x$, where $\tau_{x,z}$ are the Pauli matrices acting in particle-hole space. Again, we

with momentum $\hbar k$ is found by diagonalizing the BdG equation [27]

$$H_k \Phi_k = E_k \Phi_k. \tag{2.3}$$

This results in Bogoliubov quasiparticles which are superpositions of electrons and holes

$$b_{k\uparrow} = u_k a_{k\uparrow} - v_k a^\dagger_{-k\downarrow} \tag{2.4}$$

$$b^\dagger_{k\downarrow} = v_k a_{k\uparrow} + u_k a^\dagger_{-k\downarrow}, \tag{2.5}$$

with energy $E_k = \pm\sqrt{\epsilon_k^2 + \Delta^2}$ and coherence factors[2] $|u_k|^2 = 1 - |v_k|^2 = \frac{1}{2}\left(1 + \epsilon_k/E_k\right)$ [26]. In writing down the BdG equation, we effectively doubled the number of excitations by explicitly taking the holes into account. To resolve this, we only consider the positive energy solution. Particle-hole symmetry can be used to relate negative energy excitations to their positive energy counterparts $b_{k\uparrow} \to b^\dagger_{k\uparrow}$.

2.1.2. Majorana zero modes in nanowires

In this section, we set out to calculate the quasiparticle spectrum of a proximitized, semiconductor nanowire using the BdG formalism. The idea of using nanowires to engineer topological superconductivity started with the Kitaev chain. Kitaev showed that in an one-dimensional (1D), spinless p-wave superconductor, the Majorana operators can be paired such that two unpaired Majorana modes remain at the end of the chain [29]. Unfortunately, it has been proven difficult to find materials that exhibit p-wave superconductivity. A potential solution was offered by Fu and Kane by showing that it is possible to engineer topological superconductivity using a proximitized topological insulator [30]. Similarly, Lutchyn et al. [20] and Oreg and et al. [19] showed that it is possible to engineer such a superconductor by applying an external magnetic field to a proximitized, semiconductor nanowire with large spin-orbit interaction (SOI). Below we follow their approach.

We start with a description of the 1D semiconductor nanowire with strong Rashba SOI in a magnetic field B, for which the Hamiltonian is

$$H_k = \epsilon_k + \epsilon_{so}\sigma_y + \epsilon_B\sigma_x. \tag{2.6}$$

Here, $\epsilon_{so} = \alpha k$ with α the Rashba parameter; $\epsilon_B = \frac{1}{2} g\mu_B B$ the Zeeman energy of a spin-1/2 particle with g the Lande g-factor and μ_B the Bohr magneton; and $\sigma_{x,y,z}$ the Pauli spin matrices acting on the spin degree of freedom. Note that the magnetic field (along x) is applied perpendicular to the effective spin-orbit field (along y), and that both are perpendicular to the transport direction of the electrons $k = k_z$ (the wire points along z). The eigenvalues of this Hamiltonian are given by $E_k = \epsilon_k \pm \left(\epsilon_B^2 + \epsilon_{so}^2\right)^{1/2}$.

---

discard all constant energy terms which, all combined, give the ground state energy of the superconductor $\sum_k \epsilon_k - E_k + \Delta\langle a^\dagger_k a^\dagger_{-k}\rangle$.

[2] In Eqs. (2.4) and (2.5) we chose u, v to be real which equates to setting the phase of the superconductor to zero. In general, u and v are complex and have a phase difference equal the phase of the superconductor.

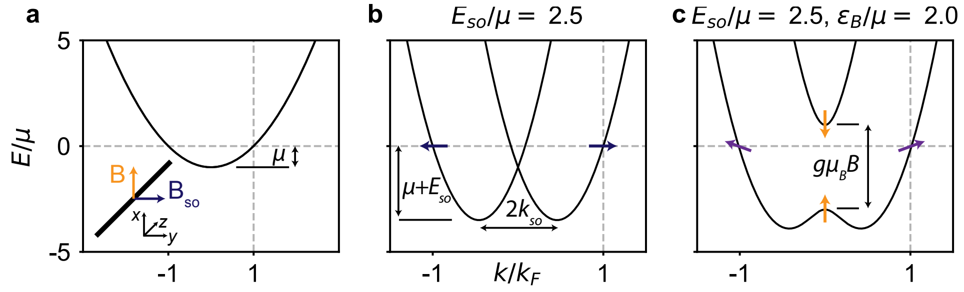

Figure 2.1 – Bandstructure of a single-band nanowire. **a** For a nanowire without spin-orbit interaction, the spin-degenerate energy bands have approximately a parabolic shape near the bottom. **b** The spin-orbit interaction causes a shift of the energy bands of $\pm k_{so}$ in momentum, depending on the spin projection along the spin-orbit field (blue arrows). The bands are still doubly degenerate. **c** A helical gap of size $g\mu_B B$ opens upon applying an external magnetic field. When the chemical potential lies within this gap, only one band crosses the Fermi surface, rendering the electrons effectively spinless (purple arrows). The inset in **a** indicates the direction of the wire and the respective fields. Note that the same effective mass is used for all panels. The bands seem to have a different curvature because the Fermi wave vector k_F is rescaled by the spin-orbit and magnetic field.

Figure 2.1 illustrates the effect of the different terms on the bandstructure of the wire. Without SOI, the bottom of the conduction band can be approximated with a parabolic dispersion (Fig. 2.1a). This band has a two-fold spin degeneracy, which have a different projection along σ_z. With finite SOI, the spins are projected along σ_y as they align to the spin-orbit field. This shifts the energy bands with $\pm k_{so} = \pm m^* \alpha/\hbar^2$ in momentum, but does not lift the degeneracy (Fig. 2.1b). The applied magnetic field can, however, lift this degeneracy; it opens a Zeeman gap (often called the helical gap) with size $g\mu_B B$ around at $k = 0$ (Fig. 2.1c). If the Fermi level lies within this gap, only one band crosses the Fermi surface, effectively lifting the spin degeneracy. In addition, the quantization axis of the spin acquires a momentum dependence. At $k = 0$, the SOI vanishes and the spins align to the applied field, but they rotate towards the spin orbit field as k increases. In the helical gap, the spin-projection is coupled to the group velocity which can be measured as a drop in the conductance of a quantum point contact [31]. To open the helical gap, it is important that the magnetic field is applied perpendicular to the spin-orbit field. In experiments, this can be accomplished by pointing the magnetic field along the wire, as the Rashba spin-orbit field is perpendicular to the momentum of the electrons.

The helical spin texture gives rise to p-wave correlations in a proximitized nanowire which we describe using the BdG formalism [24]. Since both SOI and the external field couple electrons with different spin, the matrix describing the bare wire (Eq. (2.6)) is already 2x2 which makes the corresponding BdG Hamiltonian 4x4 upon including the holes[3]. In the $\left(a_{k\uparrow}, a_{k\downarrow}, a^{\dagger}_{-k\downarrow}, a^{\dagger}_{-k\uparrow}\right)$ basis, the Hamiltonian

---

[3] The BdG Hamiltonian for a conventional superconductor could also be written as 4x4 matrix consisting

of the proximitized wire reads

$$H_k = \tau_z \otimes H_0 - \Delta\left(\tau_y \otimes \sigma_y\right), \tag{2.7}$$

where Δ is the size of the induced gap, and $\tau_{x,y,z}$ are the Pauli matrices acting on particle-hole space. The eigenenergies are given by [32]

$$E_k = \left(\epsilon_k^2 + \epsilon_{so}^2 + \epsilon_B^2 + \Delta^2 \pm 2\sqrt{\epsilon_k^2\left(\epsilon_{so}^2 + \epsilon_B^2\right) + \epsilon_B^2\Delta^2}\right)^{\frac{1}{2}}. \tag{2.8}$$

In Figure, 2.2 the evolution of the wire spectrum as a function of the external magnetic field is shown. At zero field, the proximity induced superconducting correlations result in a gap Δ around the Fermi level. There are two gaps: Δ_0 around $k = 0$ and Δ_F at $k = k_F$, corresponding to the two Fermi level crossings when $\Delta = 0$ (Fig. 2.1b). Due to the Zeeman splitting, Δ_0 decreases linearly with field $\Delta_0 = \sqrt{\mu^2 + \Delta^2} - \epsilon_B$. In contrast, the gap at the Fermi wave vector only has a weak field dependence because of the finite SOI [33]. When $\epsilon_B = \sqrt{\mu^2 + \Delta^2}$, the gap around $k = 0$ closes and the wire undergoes a topological phase transition driven by the external field (Fig. 2.2c). For larger fields, Δ_0 reopens, albeit with a different sign, and the wire is in the topological superconducting phase with MZMs localized at its ends [19, 20].

InAs and InSb nanowires have large SOI and a large g-factor which makes them good candidates for studying topological superconductivity [25]. Indeed, two hallmark signatures of MZMs, perfect Andreev reflection and fractional Josephson radiation, have been reported in these systems [34–37]. In this thesis, we use InAs nanowires for our experiments on superconducting islands and gate-based readout.

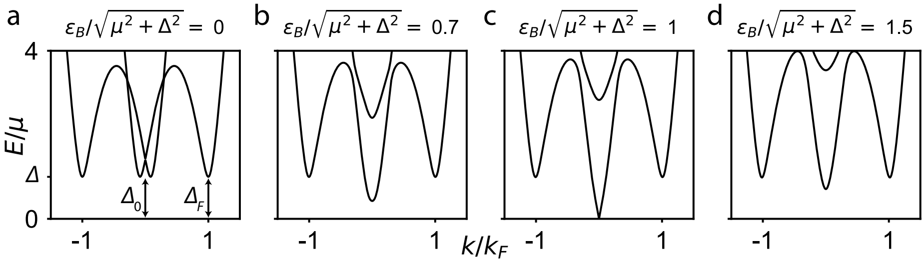

Figure 2.2 – Magnetic field evolution of the bandstructure of a proximitized nanowire. a At zero field, an induced gap of size Δ is present around the Fermi level. By increasing the field, the gap around $k = 0$, Δ_0, decreases linearly while the gap around $k = k_F$, Δ_F, remains roughly constant due to the finite spin-orbit interaction. **b** For $\epsilon_B < (\mu^2 + \Delta^2)^{1/2}$, both gaps remain finite. **c** When $\epsilon_B = (\mu^2 + \Delta^2)^{1/2}$, Δ_0 closes, while Δ_F remains finite, and the wire undergoes a topological phase transition. **d** When $\epsilon_B > (\mu^2 + \Delta^2)^{1/2}$, Δ_0 reopens (with a different sign), and the wire is in the topological phase.

---

of two decoupled 2x2 matrices. In fact, the positive energy solution, $b_{k\uparrow}^{\dagger}$, we obtained from a particle-hole symmetry argument, directly follows from diagonalizing the other 2x2 matrix.

2.1.3. Properties of Majorana zero modes

In the previous section, we learned that Majoranas can emerge in proximitized semiconductor nanowires. Here, we will zoom out and look and the general properties of MZMs.

Majorana zero modes are their own antiparticle. In addition, they obey the fermion anticommutation relations, leading to the following set of defining equations [21]

$$\gamma^\dagger = \gamma \tag{2.9}$$

$$\{\gamma_i, \gamma_j\} = 2\delta_{ij}. \tag{2.10}$$

Consequently, it does not make sense to define a number operator for a single Majorana. Moving forward, two Majoranas (e.g., γ_1 and γ_2) define one nonlocal fermionic mode $f^\dagger = \frac{1}{2}(\gamma_1 + i\gamma_2)$. Therefore, we can associate a number operator with this fermion $n_{12} = f^\dagger f$. With this definition the occupancy of the nonlocal fermion depends on the parity of the MZMs $n_{12} = \frac{1}{2}(1+P)$ with $P = -i\gamma_1\gamma_2 = \pm 1$. Thus, we can label its eigenstates either with the occupancy of the nonlocal fermion $|0,1\rangle$ or with the parity of the Majorana pair $|\pm\rangle$.

Both eigenstates have zero energy resulting in a twofold degenerate groundstate. This groundstate degeneracy increases exponentially upon adding more Majorana pairs; a system with $2N$ MZMs has a 2^N-fold degenerate groundstate. The states $|n_{12}, \dots, n_{2N,2N-1}\rangle$ of this degenerate manifold are the eigenstates of the joint number operator $n = \prod n_{i,i+1}$. Braiding two MZMs (say γ_1 and γ_2), by changing their positions, takes the system from one groundstate to another, specified by the so-called braiding matrix [22]

$$U_{12} = e^{\pm\frac{\pi}{4}\gamma_1\gamma_2} = \frac{1}{\sqrt{2}}(1 \pm \gamma_1\gamma_2). \tag{2.11}$$

This is a direct consequence of the non-Abelian exchange statistic of the MZMs. Experimental conformation of these statistics is an outstanding problem in condensed matter physics [21].

A parity measurement on a Majorana pair generally has two outcomes corresponding to the two number states. This feature, also known as the fusion channels of MZMs, relates directly to their nontrivial properties [16]. For a single pair of MZMs, however, the nonlocal fermion has a definite occupancy (or parity), and only one of the fusion channels is attainable. To observe both fusion channels two or more pairs are needed. For concreteness, we consider a system with four Majorana in the $|0_{12}0_{34}\rangle$ state. Now, we bring γ_1 and γ_4 together to measure their parity. If we measure an even/occupied state $|0_{14}\rangle$, the inner pair is also in the even/occupied state (and vice versa). These outcomes have exactly equal probability $|0_{12}0_{34}\rangle = (|0_{14}0_{23}\rangle + |1_{14}1_{23}\rangle)/\sqrt{2}$, due to the topological nature of the MZMs. This feature will be used in section 2.4 to describe projective measurements. The Majorana parity can be measured in several ways, for example by utilizing the fractional Josephson effect in a Majorana Josephson junction [38], parity-to-charge conversion [16, 39], or by coupling to a double quantum dot [17, 18].

The degeneracy between the parity states can be lifted when the wave functions of two MZMs overlap. This energy splitting should be avoided because it restores the susceptibility to local fluctuations, i.e. it removes the topological protection. It can be made exponentially small by increasing the separation between the Majoranas (or equivalently by increasing the length of the wire), because of the exponential decrease of the Majorana wave function. Additionally, the size of the energy splitting exhibits oscillatory behavior as a function of the magnetic field due to field dependence of the Fermi wave vector [40]. Recently, these effects have been seen in experiment [41].

In topological qubits, the quantum information is encoded in the degenerate grounstate, and braiding operators can be used to encode robust single qubit gates[4]. In section 2.4, we will further eloborate on Majorana qubits, but first we discuss charging effects in semiconductor nanowires, as they play an important role in the physical implementation of these qubits.

---

[4] Actually, braiding operations can only implement $\pi/2$ rotations, and thus have to be supplemented with nonprotected operations to achieve an universal set of gates with a Majorana qubit.

2.2. Quantum dots

Over the years, quantum dots have been extensively studied [42–44]. They have a discrete energy spectrum because of their small size with respect to the Fermi wave length of their electrons. Additionally, the Coulomb repulsion between electrons on a dot results in a large energy cost for adding an extra electron charge, making this charge a good quantum number. Quantum dots have found an important application in quantum-information processing as the host for spin- and charge qubits [45–47]. Moreover, the coupling between quantum dots and superconductors has led to exciting new phenomena such as π-junctions and Cooper-pair splitters [48]. Nanowires offer a natural platform to study quantum dots due to their built-in radial confinement. However, dots are not limited to semiconductor nanowires and have been realized in a whole zoo of material systems; including GaAs [43, 44], graphene [49], and carbon nanotubes [50].

Here, we are interested in quantum dots for the readout of Majorana box qubits [17, 18]. In this section, we review the relevant energy scales for single- and double quantum dots, and discuss of their transport properties.

2.2.1. Single dots

To describe single quantum dots, we use the constant interaction model [42–44]. This model makes two assumptions: first, all electrostatic interactions between electrons can be captured using one effective capacitance C for the dot; and second, the discrete energy structure of the dot E_n does not depend on the number of electrons on the dot N [43]. Given these assumptions, the total energy U of the dot is

$$U\left(N\right) = \frac{1}{2C}\left(-e\left(N - N_0\right) + \sum_i C_i V_i\right)^2 + \sum_{n=1}^{N} E_n, \tag{2.12}$$

where e is the elementary electron charge, N_0 is the offset charge when no external voltages are applied, and V_i is the voltage applied to electrode i which has a capacitance C_i to the dot (with i = s(ource), d(rain), or g(ate)). See Figure 2.3a for the effective circuit. The energy cost to put the Nth electron on the dot, i.e. the electrochemical potential[5], is $\mu\left(N\right) = U\left(N\right) - U\left(N-1\right)$. Using Eq. (2.12), we find

$$\mu\left(N\right) = \left(N - N_0 - \frac{1}{2}\right) 2E_C - e\alpha_g V_g + E_N, \tag{2.13}$$

where $E_C = e^2/2C$ is the charging energy of the dot with $C = C_g + C_s + C_d$, and $\alpha_g = C_g/C$ is lever arm of the gate. This potential scales linearly in the applied gate voltage which makes it more convenient than the total energy which scales quadraticly. The energy spacing between the transitions is called the addition energy: $E_{\text{add}}\left(N\right) = \mu\left(N+1\right) - \mu\left(N\right) = 2E_C + \Delta E_N$.

To describe electron transport through the dot, we first consider a dot with $N-1$ electrons in the linear transport regime with $V_b \approx 0$. When $\mu\left(N\right) > 0 > \mu\left(N-1\right)$,

---

[5] Assuming that we consider transitions between ground states.

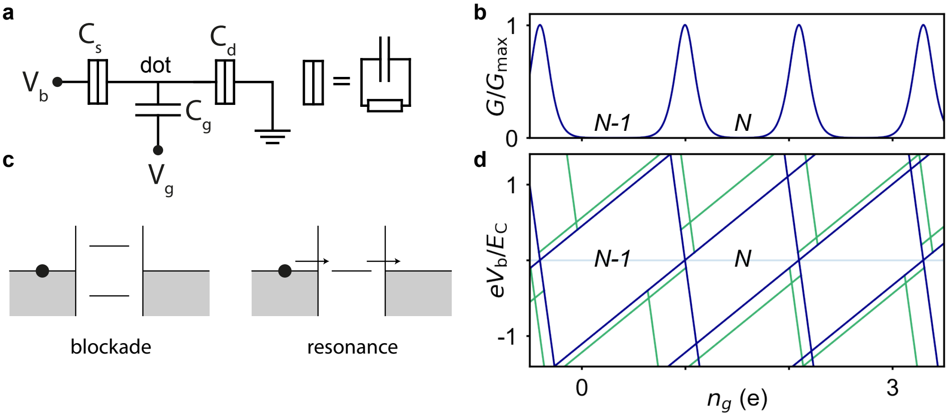

Figure 2.3 – **Single quantum dot. a** Circuit model of an asymmetrically biased single quantum dot. The junctions are modeled as a resistor $R \gg h/e^2$ in parallel with a capacitor. The electrochemical potential of the dot levels can be controlled with the gate voltage V_g and the bias voltage V_b. **b** At zero bias, the conductance of the dot shows a series of Coulomb peaks as a function of gate voltage. When the electrochemical potential μ is misaligned with the Fermi level in the reservoirs (left panel of **c**) the conductance is blocked. On the other hand, when $\mu = 0$, the number of particle on the dot is allowed to vary, leading to a finite conductance through the dot (right panel of **c**). **d** The linear increase of the bias window with bias voltage leads to the characteristic Coulomb diamonds in (V_g, V_b)-space. The blue lines result from transitions between two ground states with a different number of electrons. The green lines represent transitions from the ground state to the first excited state (and vice versa).

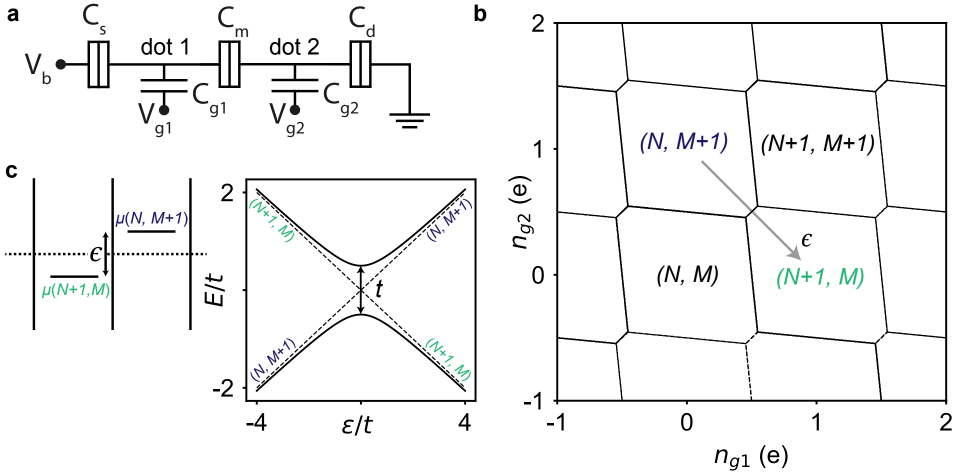

Figure 2.4 – **Double quantum dot. a** Circuit diagram of a double quantum dot in series. **b** The number of charges on dot i can be controlled via the gate voltage V_{gi} resulting in a charge stability diagram. **c** The spectrum close to the interdot transition between $(N, M+1)$ and $(N+1, M)$ as a function of the detuning ϵ. The coherent tunnel coupling between the dots hybridizes the charge states leading to an anti-crossing in the spectrum (solid lines). The dashed lines represent the situation without tunnel coupling.

the number of electrons is fixed and therefore no current can flow, see the left panel of Figure 2.3c. This situation is called Coulomb blockade. By adjusting the gate voltage to V_g^N so that $\mu(N) = 0$, the blockade is lifted, and the number of electrons on the dot is allowed to fluctuate between $N-1$ and N, see Figure 2.3c. In this case, electrons can be transported through the dot sequentially, leading to a so-called Coulomb peak in the measured current. A series of these Coulomb peaks is measured as the gate voltage is swept over multiple dot levels (see Fig. 2.3b). The spacing between the Nth and the $(N+1)$th peak, also called the Coulomb valley, is proportional to the addition energy $E_{\text{add}}(N) = e\alpha_g\left(V_g^{N+1} - V_g^N\right)$.

The addition energy can also be found using finite-bias measurements. Now, the blockade is lifted whenever a dot level enters the bias window $-eV_b = \mu_s - \mu_d$. We consider an asymmetric biasing scheme for which $\mu_d = 0$, see in Figure 2.3a. The level $\mu(N)$ enters the bias window when $\mu(N) = 0$, and exits again when $\mu(N) = -eV_b$. This leads to so-called Coulomb diamonds in the $\left(V_g, V_b\right)$-plane, see Figure 2.3d. The height of Nth diamond is set by the addition energy $E_{\text{add}}(N)$, making it possible to extract the lever arm α_g from a diamond measurement.

So far, we have only considered groundstate transitions. However, at high bias, transitions to the excited state(s) are possible as well. When $-eV_b > \Delta E_{N+1}$, the transition to the first excited state can enter the bias window. This results in additional lines in the $\left(V_g, V_b\right)$-plane that run parallel to the lines corresponding to ground state transitions. In general, a line ending in the Nth diamond corresponds to the excited state of the N electron system.

2.2.2. Double dots

A double quantum dot (DQD) can be made by connecting two quantum dots in series, as shown in Figure 2.4a. Similar to a single dot, the charge occupation of the dots (N, M) can be controlled via the two gates, leading to a so-called charge stability diagram with a hexagonal structure, see Fig. 2.4b [51]. The DQD exchanges particles with the reservoir whenever the electrochemical potential is zero, resulting in the horizontal (i.e. the transitions between (N, M) and $(N, M+1)$) and the vertical (i.e. the transitions between (N, M) and $(N+1, M)$) boundaries of the hexagon. It is also possible to exchange electrons between the two dots (i.e. the transition between $(N, M+1)$ and $(N+1, M)$). These interdot transitions occur when $\mu_1(N+1, M) = \mu_2(N, M+1)$ if $(N+1, M)$ and $(N, M+1)$ form the (degenerate) groundstate of the DQD.

Hybridization of the charge states due to coherent electron tunneling between the dots lifts this (energy) degeneracy. To illustrates this coupling, we consider an effective Hamilonian for the double dot valid around the interdot transition between $(N+1, M)$ and $(N, M+1)$

$$H_{\text{DQD}} = -\frac{\epsilon}{2}\sigma_z - \frac{t}{2}\sigma_x, \tag{2.14}$$

where t is the tunnel coupling between the two dots, and ϵ is the energy difference between the (unperturbed) charge states (often called the detuning), see Fig. 2.4c.

The energy levels of this system are

$$E_{\pm} = \mp\frac{1}{2}\sqrt{\epsilon^2 + t^2}, \tag{2.15}$$

corresponding to the bonding $|+\rangle$ and anti-bonding $|-\rangle$ states

$$|+\rangle = \frac{1}{\sqrt{2}}\left(\sqrt{1+\epsilon/\Omega}\,|N, M+1\rangle + \sqrt{1-\epsilon/\Omega}\,|N+1, M\rangle\right), \tag{2.16}$$

$$|-\rangle = \frac{1}{\sqrt{2}}\left(\sqrt{1-\epsilon/\Omega}\,|N, M+1\rangle - \sqrt{1+\epsilon/\Omega}\,|N+1, M\rangle\right) \tag{2.17}$$

where $\Omega = \sqrt{\epsilon^2 + t^2}$. Figure 2.4c shows the energy spectrum along ϵ for zero and finite tunneling coupling. Indeed, the tunnel coupling lifts the degeneracy by hybridizing the charge states.

2.3. Superconducting islands

In the previous section, we investigated charging effects in semiconductor quantum dots. In this section, we look at the consequences of making the dots superconducting. We will refer to these superconducting "dots" as islands because, in this case, the level spacing is negligible. These islands are building blocks of Majorana box qubits because they help to control the parity of the qubit. Therefore, recent research has been directed at realizing these structures in semiconductor nanowires [41, 52–54].

In this section, we will first describe the interplay between Coulomb blockade and superconductivity resulting in the parity effect with a $2e$-periodic Coulomb peak spacing. Then, we look at supercurrents in a so-called single-Cooper-pair transistor (SCPT) where the island is connected to superconducting leads. Finally, we discuss the effect of quasiparticle poisoning and temperature on the parity effect. These discussions form the basis for the experiments presented in chapters 4 and 6.

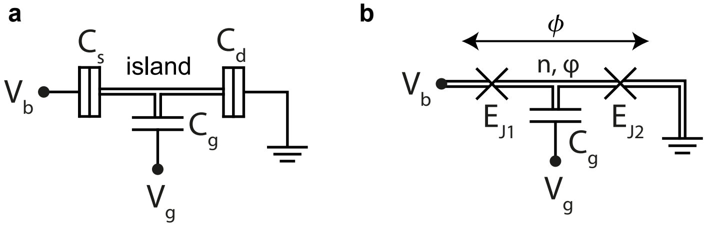

Figure 2.5 – Circuit diagram for a superconducting island (a) and a single-Cooper-pair transistor (b). The double lines indicate the superconducting sections of the device. In **b**, ϕ is the superconducting phase across the island and φ is the phase of the superconductor on the island. φ and n are conjugate variables and cannot be determined simultaneously.

2.3.1. The parity effect

In mesoscopic superconducting islands, charging effects are combined with superconductivity resulting in a parity effect with a preference for even charge states [55–60]. The island Hamiltonian consists of a Coulomb term and a superconducting term: $H = H_C + H_{\mathrm{BCS}}$, see Figure 2.5a. The Coulomb term is given by

$$H_C = E_C \sum_n \left(n - n_g\right)^2 \tag{2.18}$$

similar as in section 2.2.1. Here, we only consider the gate voltage, and set the offset charge to zero $N_0 = 0$. Moreover, we neglect the discrete energy structure of the island[6]. As we have seen in section 2.1.1, the BCS Hamiltonian can be written as $H_{\mathrm{BCS}} = \sum_{k\sigma} E_k b^{\dagger}_{k\sigma} b_{k\sigma}$. We simplify this Hamiltonian by assuming that the island can only contain one quasiparticle with energy Δ; a second quasiparticle would condense with the already present quasiparticle the into a Cooper pair with $E = 0$. With this assumption H_{BCS} reduces to

$$H_{\mathrm{BCS}} = \begin{cases} 0 & n \text{ is even} \\ \Delta & n \text{ is odd.} \end{cases} \tag{2.19}$$

This additional energy penalty for the odd states leads to the parity effect. Proximitized semiconductor nanowires can contain bound states with energies below the the gap [52]. Examples of such states include Andreev bound states due to the finite size of the wire [62] and MZMs [41]. In this case, the quasiparticle in the odd charge states occupies the subgap state with the lowest energy E_0 instead of a continuum state at Δ. Regardless, there is an energy penalty for the odd states.

Within this framework, the energy spectrum of the island is easily calculated. The different columns of Figure 2.6 show the spectrum for various values of Δ/E_C together with the resulting Coulomb peak spacing. In the first column, the groundstate always contains an even number of particles because $\Delta > E_C$. At odd gate charge values, the groundstate is degenerate $E_{\mathrm{gs}}(N) = E_{\mathrm{gs}}(N+2)$ and transport through the island is allowed, mediated by Andreev reflection at the junctions [63, 64]. This leads to a 2e-periodic Coulomb peak spacing (Fig. 2.6g). For the middle column, $\Delta < E_C$. Now, the ground state switches parity when adjacent, charge states are degenerate $E_{\mathrm{gs}}(N) = E_{\mathrm{gs}}(N+1)$, and single particles charge the island [57, 64]. This happens at $n_{\mathrm{g}} = \pm n_{\mathrm{g}}^{eo} + 2l$ with $n_{\mathrm{g}}^{eo} = (\Delta + E_C)/2E_C$ and integer l. Consequently, the Coulomb peak spacing exhibits an even-odd pattern. The length of the even/odd Coulomb valleys (in gate reduced charge) scales with the superconducting gap $\Delta n_g^{e/o} = \left(E_C \pm \Delta\right)/E_C$. Hence, the superconducting gap can be extracted by tracking the extend of the Coulomb valleys, using so-called Coulomb peak spectroscopy $2\Delta/E_C = \Delta n_g^e - \Delta n_g^o$. Again, this can be related to the spacing in gate voltage via the gate lever arm $4\Delta = e\alpha_g(\Delta V_g^e - \Delta V_g^o)$. In the particular case where $\Delta = 0$ (right column), the Coulomb peaks are regularly spaced with an 1e period.

---

[6] We estimate the level $\delta \approx 0.1\,\mu\mathrm{eV}^{-1}$ from $\rho = 23\,\mathrm{eV\,nm}^{-3}$ and $V \approx 5 \times 100 \times 1000\,\mathrm{nm}^3$ [61].

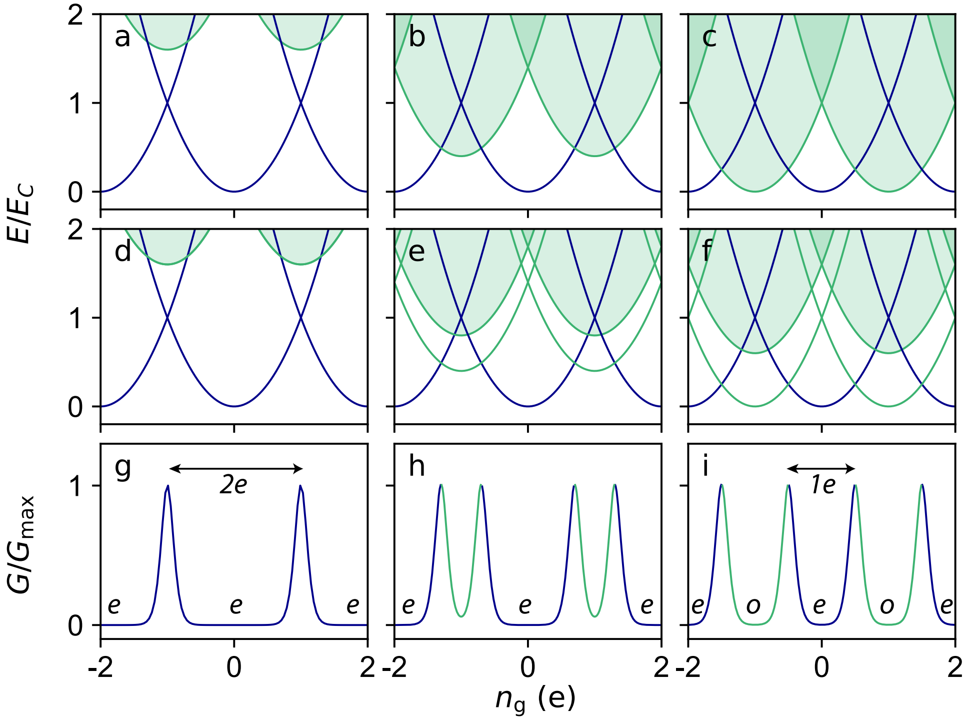

Figure 2.6 – **Energy versus gate charge and zero bias conductance of a superconducting island.** **a-f** Energy dispersion versus gate charge for the case without a subgap state **a-c** and with a (field-induced) subgap state **d-f**. The even (odd) states are indicated with blue (green). **g-i** Resulting zero bias conductance of the island (ordered by column). For the first column $\Delta > E_C$ which gives a $2e$-periodic Coulomb peak spacing, for the second column $\Delta < E_C$ which gives an even-odd pattern, and for the third column $\Delta = 0$ which results in a $1e$ periodicity.

The charging energy and the superconducting gap can also be obtained via finite bias measurements. When $\Delta < E_C$, the addition energy of the even/odd state is given by $2(E_C \pm \Delta)$. In case $\Delta > E_C$, the addition energy is $8E_C$. Moreover, the gap can also be extracted from the onset of quasiparticle transport via cotunneling processes at $V_b = 2\Delta$.

Next, we discuss the typical evolution of the energy spectrum with a magnetic field applied perpendicular (top row) or parallel (middle row) with respect to the wire [54]. In a simplified picture, a perpendicular field only causes the lowering of the bulk gap, whereas a parallel field also causes the Zeeman splitting of the spinful bound state $E_0\left(B_\parallel\right) = E_0(0) - \frac{1}{2} g\mu_B B_\parallel$. The island is driven into the normal phase when the field is increased above the critical field of the superconductor resulting in equally spaced Coulomb peaks. The Zeeman splitting, on the other hand, leads to a subgap state separated from the continuum, because the g-factor of the subgap state is typically larger than the g-factor of the superconductor as it is partially located inside the wire [65, 66]. At zero energy, the state can either stick to zero, in case of a MZM or a quasi-Majorana state [67], or cross through zero, in case of a trivial bound state or an overlapping Majorana state [40], upon increasing the field further. The former case again leads to equally spaced peaks; whereas in the latter case, the length of the even and odd Coulomb valleys invert as a consequence of the zero energy crossing.

2.3.2. Single-Cooper-pair transistors

In a single-Cooper-pair transistor (Fig. 2.5b), the superconducting island is connected to superconducting leads via Josephson junctions, which are gate-tunable in a nanowire setup [68]. In this configuration a supercurrent can flow. In this section, we calculate the gate dependence of the critical current through the island. Here, we define the critical current as the maximum supercurrent that can flow at a particular gate setting.

Compared to Eqs. (2.18) and (2.19), the Hamiltonian of a SCPT contains a Josephson term reflecting the Josephson coupling between island and the leads $H = H_C + H_{\mathrm{BCS}} + H_J$. The junctions are modeled as

$$H_J = -E_{J1}\cos(\hat{\varphi} - \phi/2) - E_{J2}\cos(\hat{\varphi} + \phi/2), \tag{2.20}$$

where $\hat{\varphi}$ is the phase on the island, ϕ is the phase difference between the leads, and $E_{J1,2}$ are the Josephson energies of the two junctions. The operator $\exp(\pm i\hat{\varphi})$ adds (removes) a Cooper pair to (from) the island. Hence, Eq. (2.20) describes Cooper pair tunneling across the junctions. By combining the terms, the Hamiltonian reduces to

$$H_J = -\sqrt{\left(E_{J1} + E_{J2}\right)^2 - 4E_{J1}E_{J2}\sin^2(\phi/2)}\sum_n |n\rangle\langle n+2| + \mathrm{H.c.} \tag{2.21}$$

From the total Hamiltonian, we obtain the groundstate energy E_{gs} which is a function of n_{g} and ϕ. The hybridization between adjacent, equal parity charge states results in an anti-crossing in the spectrum (see Fig. 2.7). Now, the gate modulation of the critical current can be found through

$$I_c\left(n_g\right) = \max_{\phi} \frac{e}{\hbar}\frac{\partial}{\partial\phi}E_{gs}\left(n_g, \phi\right). \tag{2.22}$$

The bottom row of Figure 2.7 shows the critical current modulation by the gate charge for different energies of a subgap state E_0[7]. If $E_0 > E_C$, the critical current is maximal at odd values of the offset charge. This can be understood as a consequence of the uncertainty principle for the conjugate variables n and φ; the large supercurrent around n_g = odd results in well-defined phase states, while the charge states hybridize [69].

Similar to the Coulomb peaks, the $2e$-periodic critical current modulation evolves via an even-odd pattern to an $1e$-periodic modulation as the energy of the subgap state is decreased to zero. However, unlike for conductance measurements, the maximal current strongly decreases when $E_0 < E_C$. In this case, the anti-crossing giving rise to the critical current is not contained within the groundstate.

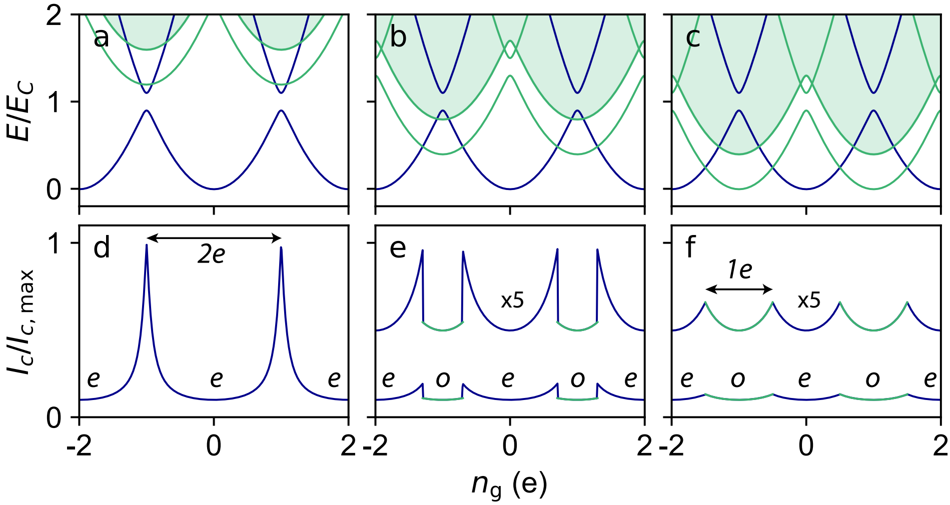

Figure 2.7 – Energy spectrum and critical current versus gate charge in a single-Cooper-pair transistor. a-c Energy spectrum versus gate charge for a SCPT containing a subgap state. The even (odd) states are indicated with blue (green). **d-f** Resulting critical current versus gate charge. For the first column, $E_0 > E_C$ resulting in a $2e$-periodic critical current modulation. For the second column, $E_0 < E_C$, and the critical current exhibits an even-odd pattern. When the odd state is the groundstate, the system is far detuned from the anti-crossing and the critical current drops. For the third column, $E_0 = 0$ and the critical current is $1e$-periodic. For panel **e** and **f**, the critical current modulation is shown twice; the upper trace is multiplied by a factor 5 to increase its visibility.

---

[7] Here, we depict a spectrum with a subgap state in anticipation of chapter 4. However, within our framework, the modulation would be the same without this subgap state.

2.3.3. Quasiparticle poisoning

In the previous sections, we looked at the parity effect in superconducting islands and SCPTs. However, we only considered the groundstate properties of these systems. These are valid at zero temperature and without the stochastic parity flips that can occur when quasiparticles in the leads hop on and off the island. Here, we discuss the latter effect which is also known as quasiparticle poisoning. The temperature dependence is treated is the next section.

Quasiparticle poisoning harms the operation of superconducting devices; it causes decoherence in superconducting and Majorana qubits [70, 71]. Naively, one would expect an exponentially small quasiparticle density as it is suppressed by the superconducting gap: $n_{qp} = \rho\sqrt{2\pi\Delta k_B T}\,\exp\left(-\Delta/k_B T\right)$ [72]. However, many experiments have reported a significant quasiparticle concentration [73–75]. Though the source of these nonequilibrium (or nonthermal) quasiparticles remains unknown [76], advancements have been made in understanding their dynamics [73], and in reducing and controlling their density profile by using normal metal quasiparticle traps and gap engineering [60, 77, 78].

To describe the consequences of quasiparticle poisoning for the parity effect, we use the weighted sum of the even and odd signal as a simple toy model. For a conductance measurement, this results in $G = p_e G_e + (1 - p_e) G_0$. The weight $p_e = 1/\left(1 + \Gamma_{\text{in}}/\Gamma_{\text{out}}\right)$ is the steady state solution of the master equation $\dot{p}_{e,o} = \mp\Gamma_{\text{in}} p_e \pm \Gamma_{\text{out}} p_o$, subjected to $p_e + p_o = 1$. In Figure 2.8, the resulting conductance signal is plotted for various ratios of $\Gamma_{\text{in}}/\Gamma_{\text{out}}$. We see that the $2e$ periodicity is retained as long as the unpoisoning rate Γ_{out} is much larger than the poisoning rate Γ_{in}. As the ratio increases towards unity, an additional conductance peak appears at odd values of the gate charge, making the signal $1e$-periodic.

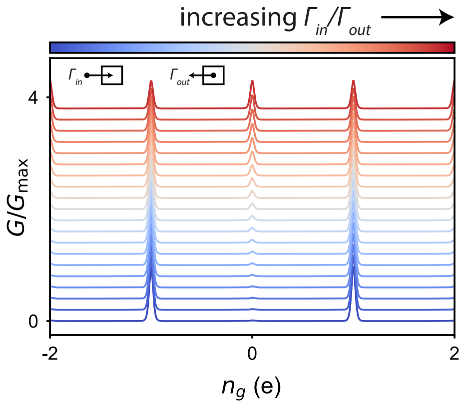

Figure 2.8 – Quasiparticle poisoning. The parity effect is destroyed as the poisoning rate (characterized by $\Gamma_{\text{in}}/\Gamma_{\text{out}}$) is increased. Individual traces are offset for clarity.

2.3.4. Temperature dependence of the parity effect

At nonzero temperatures, the gap giving rise to the parity effect in Eq. (2.19) is replaced by the free energy difference to include the entropy associated with the large number of states at the gap edge [79]

$$F_o - F_e = -k_B T \ln\left(\frac{Z_e}{Z_o}\right). \tag{2.23}$$

Here, $2Z_{e,o} = \prod_i \left(1 + \exp\left(-\epsilon_i/k_B T\right)\right) \pm \prod_i \left(1 - \exp\left(-\epsilon_i/k_B T\right)\right)$ is the partition function of the even (odd) parity sector. Evaluating these products in the case of a superconducting island with a spin degenerate subgap state yields [52]

$$F_o - F_e \approx -k_B T \ln\left(N_{eff} e^{-\Delta/k_B T} + 2e^{-E_0/k_B T}\right), \tag{2.24}$$

with $N_{eff} = \rho V \sqrt{2\pi\Delta k_B T}$ the effective number of states at the gap edge. Figure 2.9 show the evolution of $F_o - F_e$ as a function of temperature. For temperatures below $T^{**} \approx (\Delta - E_0) / \left(k_B \ln\left(N_{eff}/2\right)\right)$, the free energy difference is only weakly dependent on temperature due to the presence of the subgap state. Above T^{**}, the free energy decreases linearly until it finally reaches zero around $T^{*} \approx \Delta / \left(k_B \ln\left(N_{eff}\right)\right)$. Consequently, a $2e$-periodic signal will evolve via an even-odd pattern into a $1e$-periodic signal upon raising the temperature. Typically, $T^{*} \approx 300\,\mathrm{mK}$ for an aluminum island which is smaller than the critical temperature of aluminum.

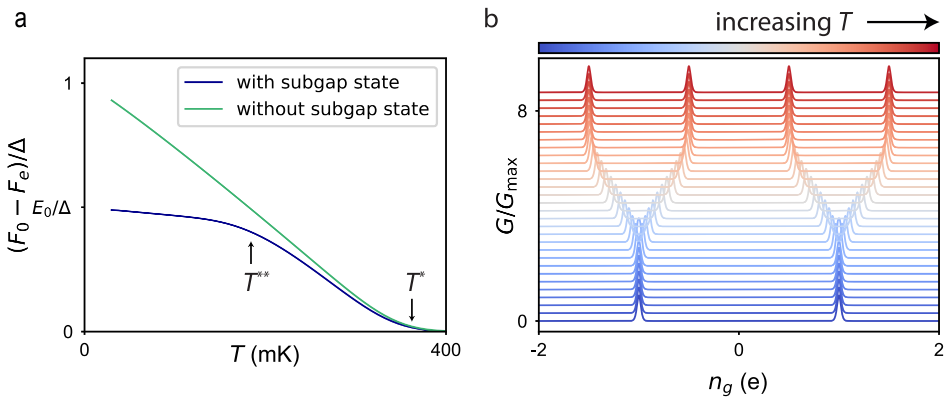

Figure 2.9 – Temperature evolution of the parity effect. a The free energy difference between the odd and even state as a function of the temperature for an aluminum island with (blue) and without (green) a subgap state. The presence of a subgap state causes a saturation of the free energy difference below T^{**}. Above T^{*}, the free energy difference is zero. **b** The decrease of $F_o - F_e$ with temperature causes a transition from a $2e$ periodicity to an even-odd pattern when $F_o - F_e < E_C$, and subsequently to a $1e$ periodicity when $F_o - F_e = 0$. Individual traces are offset for clarity.

2.4. Majorana box qubits

As we have seen in section 2.1.3, the topological properties of Majorana zero modes give rise to nonlocal fermionic states. The quantum information stored in these states is protected against local perturbations[8], and is therefore expected to have long coherence times. Over the past years, many proposals for Majorana-based qubits have been developed [15–18, 38, 39, 80, 81]. Here, we briefly review the similarities and differences between these proposals. We elaborate on the readout of the Majorana box qubit as it forms an important motivation for this thesis.

Generally, the state of a Majorana-based qubit is encoded in the parity (or number) basis of the underlying nonlocal fermions. This requires a minimum of four MZMs, $\gamma_1, \dots, \gamma_4$ (or two nonlocal fermions f_{12} and f_{34}) so that the qubit can change its state by flipping the parity of both fermions while the total parity is fixed. Here, we define the qubit in $(|0_{12}0_{34}\rangle, |1_{12}1_{34}\rangle)$. In this basis, the four MZMs encode the effective spin state

$$\sigma_x = -i\gamma_2\gamma_3, \tag{2.25}$$

$$\sigma_y = -i\gamma_3\gamma_1, \tag{2.26}$$

$$\sigma_z = -i\gamma_1\gamma_2. \tag{2.27}$$

Majorana qubits can be manipulated by braiding the MZMs. The main difference between the proposals is the way these braiding operations are implemented. Roughly, we distinguish three ideas: Initially, it was proposed to physically move the MZMs to implement braiding operations [38]. Later, it was recognized that an adiabatic time-evolution of the interaction between MZMs can achieve the same operation [80, 81]. This interaction can be controlled via the tunneling coupling between MZMs [80], or by modulating the Coulomb-mediated interaction [15, 16, 39, 81]. Lastly, in Majorana box qubits, braiding is performed via a series of projective measurements [17, 18].

The latter approach is more generally known as measurement-only topological quantum computation. The see how it works, we consider the projector $\prod_0^{23} = \frac{1}{2}(1 - i\gamma_2\gamma_3)$ which enforces that the MZM pair γ_2, γ_3 fuses to 0 when measured in the $(|0_{14}0_{23}\rangle, |1_{14}1_{23}\rangle)$ basis. This means that $\prod_0^{23}|0_{12}0_{34}\rangle = |0_{14}0_{23}\rangle$, which effectively transfers $|0_{34}\rangle$ to $|0_{14}\rangle$, a feature known as anyonic state teleportation. Now, by repeatedly performing these projective measurements, single-qubit gates can be encoded. For example, the sequence $\prod_0^{34}\prod_0^{13}\prod_0^{23}\prod_0^{34}$ corresponds to braiding MZMs γ_1 and γ_2, while γ_3 and γ_4 fuse to 0. This can be verified with (brute force) calculations using the anticommutation relations of the underlying fermions or a diagrammic approach [18].

Majorana parity readout is essential for these projective measurements. In the next section, we will see how these parity measurement can be performed by coupling the box qubit to a quantum dot.

---

[8] Except for quasiparticle poisoning.

2.4.1. Majorana box qubit readout

Figure 2.10 shows a schematic image of the so-called Majorana box qubit (MBQ) [17, 18]. It consists of two parallel topological superconductors connected by a trivial superconductor. Because of the parallel configuration of the topological sections, it is possible to align the magnetic field to both wires at the same time. The length of the topological wires should be much longer than the Majorana coherence length $L_{wire} \gg \xi$ to avoid overlap between the Majorana wavefunctions and the associated lifting of groundstate degeneracy. The trivial superconductor ensures that the qubit has a single charging energy E_C. Moreover, it blocks uncontrolled $1e$ charge-transfer between the two sections which otherwise could cause parity fluctuations of $i\gamma_1\gamma_3$ and $i\gamma_2\gamma_4$.

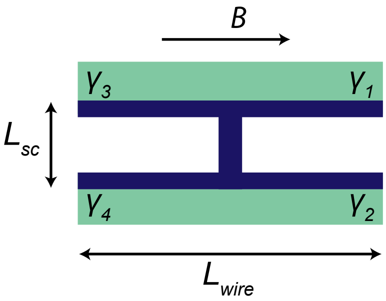

Figure 2.10 – Schematic representation of the Majorana box qubit. The four Majoranas $\gamma_1, \dots, \gamma_4$ at the end of the topological superconductors (in green) constitute a nonlocal spin which is used to encode the qubit. The topological superconductors are connected via a s-wave superconductor (in dark blue) allowing for $2e$ charge-transfer between the topological superconductors.

The parity operators of Eqs. (2.25) to (2.27) can be measured by connecting the corresponding Majorana pair to either a single or a double quantum dot. In either of these configurations, the tunneling coupling depends on the occupation of the Majorana pair due to interference of the tunneling paths. To illustrate this further, we consider the readout of the σ_z operator, corresponding to the setup shown in Figure 2.11. We focus on the single dot case for which the Hamiltonian is given by

$$H = \epsilon^{\mathrm{QD}} d^\dagger d + E_C^S \left(n - n_g\right)^2 + H_T. \tag{2.28}$$

Here, the first term describes a single spin-polarized level d in the dot which is detuned by ϵ^{QD} from the Fermi level; the second term describes the charging of the box; and the third term represents the coupling between the dot level and the MZMs [18]

$$H_T = e^{-i\varphi/2}\left(t_1 d^\dagger \gamma_1 + t_2 d^\dagger \gamma_2\right) + \mathrm{H.c.} \tag{2.29}$$

$$= -\frac{1}{2}\left[\left(t_1 + it_2\right) d^\dagger f^\dagger e^{-i\varphi} + \left(t_1 - it_2\right) d^\dagger f + \left(t_1^* - it_2^*\right) d f e^{i\varphi} + \left(t_1^* + it_2^*\right) d f^\dagger\right], \tag{2.30}$$

where $t_{1,2}$ are the tunnel couplings to Majoranas $\gamma_{1,2}$, and $\exp(-i\varphi/2)$ removes a single electron from the MBQ. To arrive at the second equality, the Majorana operators are expressed in terms of the creation/annihilation operators of the underlying nonlocal fermion: $\gamma_1 = \frac{1}{2}e^{-i\varphi/2}\left(f^\dagger + e^{i\varphi}f\right)$ and $\gamma_2 = \frac{i}{2}e^{-i\varphi/2}\left(f^\dagger - e^{i\varphi}f\right)$. There are two distinct processes that exchange particles between the qubit and the dot, one involves breaking a Cooper pair to fill the nonlocal state and the dot (and the reverse); the other one exchanges an electron between the dot and the nonlocal state.

When written in the $(|p_{12}, n_{\mathrm{dot}}\rangle)$ basis, where p_{12} is the eigenvalue of σ_z and n_{dot} the occupation of the dot, Eq. (2.28) reads

$$H = -\frac{1}{2}\begin{bmatrix} \epsilon & t_1 + ip_{12}t_2 \\ t_1^* - ip_{12}t_2^* & -\epsilon \end{bmatrix}. \tag{2.31}$$

In other words, the tunneling amplitude between the MBQ and the quantum dot depends on the parity of $i\gamma_1\gamma_2$ and can thus be used to measure σ_z.

Similarly, it can be shown that the tunnel coupling between the two dots in the double dot configuration (Fig. 2.11b) acquires a parity-dependent term [17]

$$t = t_{\mathrm{ref}} + p_{12}t_{\mathrm{MBQ}}, \tag{2.32}$$

with t_{ref} the direct tunneling amplitude between the dots, and $t_{\mathrm{MBQ}} \approx t_1t_2/\Delta_{\mathrm{MBQ}}$ the contribution due to cotunneling through the MBQ with Δ_{MBQ} the detuning of the chemical potential of the box qubit with respect to the DQD (see Fig. 2.11b).

Compared to the single dot case, the double dot approach has several advantages. For one, it allows for independent tuning of the global coupling amplitude by adjusting t_{ref}. Also, the MBQ can be operated deeper in Coulomb blockade, making it less susceptible to quasiparticle poisoning [18]. Moreover, the qubit state is not sensitive to dephasing of the readout dot. For both approaches, it is important that the level spacing of the readout dot(s) is larger than the thermal energy $\delta\epsilon \gg k_BT$, because the scheme requires coherent charge tunneling from a single dot level.

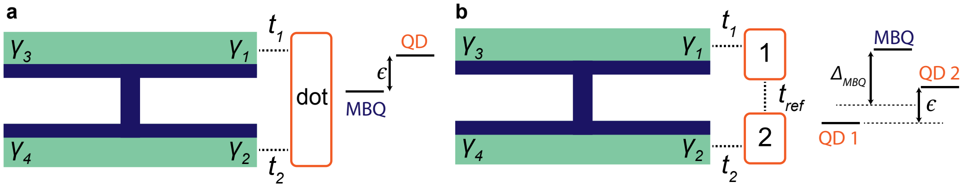

Figure 2.11 – Quantum dot-based readout of the Majorana box qubit. The interference of the tunnel couplings between a pair of Majoranas and a single dot **a**, or double dot **b** leads to a parity-dependent tunneling amplitude. The relevant levels in the QD(s) and MBQ are shown schematically.

The other Pauli operators, $\sigma_x = -i\gamma_2\gamma_3$ and $\sigma_y = -i\gamma_3\gamma_1$, can be measured by connecting the respective Majorana pairs to quantum dots. Additionally, in a loop containing two dots connected to four MZMs it is possible to measure the joint-parity of these Majoranas [17, 18]. These joint-parity measurements can be used to implement two qubit gates. The number of measurable parity operators depends on the number of ways the MZMs can connect to quantum dots. To increase this connectivity, coherent links made from Majorana islands can be used to readout distant Majoranas [82]. In Refs. 17 and 18, they combine these links with smart qubit geometries to achieve scalable qubit networks. We note that the parity readout can also be implemented with Cooper pairs instead of electrons cotunneling through the respective Majorana pair [83].

2.5. Gate-based reflectometry

As we have seen in the previous section, we can readout the Majorana box qubit by translating the difference in tunnel coupling associated with the two parity states to a difference in readout signal. This can be done by imbedding the gate of the quantum dot in a L_rC_r tank circuit and monitoring the phase shift of the reflected radio frequency (RF) probe field (see next chapter for a more elaborate discussion). This technique, called RF reflectometry, has been successfully used to readout superconducting and spin qubits. In this section, we will derive a semi-classical expression for the gate impedance of a double quantum dot following Refs. 84 and 85. As we will see, the reactive part of this impedance contains a parametric capacitance C_p term, which in turn consist of a quantum capacitance C_q and a tunneling capacitance C_t. The quantum capacitance is inversely proportional to the tunneling coupling and can thus be used for the readout of the box qubit.

2.5.1. Gate impedance of a double quantum dot

To obtain the gate impedance $1/Z_g = I_g/V_g$, we calculate the gate current $I_g = \mathrm{d}Q_g/\mathrm{d}t$ from the gate charge Q_g. The relation between the gate charge and the gate voltage V_g is determined using a network of capacitors to represent the circuit of the DQD, see Fig. 2.4a,

$$Q_g = \alpha_g C_s V_g + e\alpha_g P, \tag{2.33}$$

where P is the charge occupancy of the readout dot. For simplicity, we assumed $C \gg C_m$ so that the dots are effectively decoupled. By differentiating Eq. (2.33), we get

$$I_g = C_{\text{geom}} \frac{\mathrm{d}V_g}{\mathrm{d}t} + e\alpha_g \frac{\mathrm{d}P}{\mathrm{d}t}. \tag{2.34}$$

The geometric contribution of the gate impedance is set by the gate capacitor connected in series with the source capacitor: $C_{\text{geom}}^{-1} = C_g^{-1} + C_s^{-1}$. To evaluate the second term in Eq. (2.34), we write $P = \frac{1}{2} + \frac{\epsilon}{2\Omega}(P_+ - P_-)$ using Eqs. (2.17) and (2.16). Here, $P_\pm$ are the occupancies of the groundstate and the excited state respectively. Furthermore, we note that the probe signal modulates the gate potential $V_g(t) = V_g + \delta V_g \sin(\omega t)$, and hence, the detuning of the dot levels $\epsilon(t) = \epsilon_0 + \delta\epsilon \sin(\omega t)$

with $\delta\epsilon = -e\alpha\delta V_g$. Now, the dot occupancy acquires a time dependence via two processes: one, because the probe signal modulates the (detuning-dependent) charge polarization of the DQD, and second, because the charge is redistributed within the double dot via tunneling processes on the time scale of the modulation. These processes lead to the quantum and tunneling capacitance respectively

$$\frac{\mathrm{d}P}{\mathrm{d}t} = \underbrace{(P_+ - P_-)\frac{\mathrm{d}}{\mathrm{d}t}\frac{\epsilon}{2\Omega}}_{\text{quantum}} + \underbrace{\frac{\epsilon}{2\Omega}\frac{\mathrm{d}}{\mathrm{d}t}(P_+ - P_-)}_{\text{tunneling}}. \tag{2.35}$$

This result is semi-classical because we disregard any coherent oscillations between the states (for example, Landau-Zener transitions). For a double dot, this is a valid assumption given that the typical DQD coherence time is well below 100 ns [47, 86]; much smaller than the typical integration time.

The quantum capacitance is now readily calculated

$$C_q = \frac{\left(e\alpha_g\right)^2}{2}\frac{t_c^2}{\Omega^3}(P_+ - P_-). \tag{2.36}$$

To evaluate the tunneling contribution, the master equation $\dot{P}_+ - \dot{P}_- = 2\left(\Gamma_+ P_- - \Gamma_- P_+\right)$ needs to be solved. Following Ref. [84], we assume that the excitation and relaxation processes are driven by thermal phonons: $\Gamma_- = \Gamma^c n_p$ and $\Gamma_+ = \Gamma^c\left(1 + n_p\right)$, where Γ^c is the charge relaxation rate, and $n_p = \left(\exp\left(\Omega/k_B T\right) - 1\right)^{-1}$ is the phonon occupation number. This results in the following expression for the tunneling capacitance:

$$C_t = \frac{\left(e\alpha_g\right)^2}{2}\frac{1}{2k_B T}\left(\frac{\epsilon}{\Omega}\right)^2\frac{\gamma^2}{\omega^2 + \gamma^2}\coth^{-2}\left(\Omega/2k_B T\right), \tag{2.37}$$

where $\gamma = \Gamma^c\coth\left(\Omega/2k_B T\right)$ is the characteristic relaxation rate at temperature T. When $\gamma \approx \omega$, the tunneling processes also lead to a dissipative contribution to the impedance R_{sys}, known as the Sysiphus resistance [84].

2.5.2. Circuit quantum electrodynamics

Circuit quantum electrodynamics (cQED) describes the interaction between matter and light. In this section, we discuss the coupling between the double quantum dot and the resonator in the language of cQED [87, 88], as an alternative to the circuit element approach discussed in the previous section. We start with the Hamiltonian of the DQD-resonator system:

$$H = H_{\mathrm{DQD}} + H_r + H_{\mathrm{coupling}}, \tag{2.38}$$

with H_{DQD} as in Eq. (2.14), and $H_r = \left(a^\dagger a + \frac{1}{2}\right)\hbar\omega_0$ describing the resonator. In the latter, $n = a^\dagger a$ is the photon number operator of the resonator mode ω_0. The resonator couples to the dipole moment σ_z of the DQD. In the bonding/antibonding basis, this coupling is expressed as

$$H_{\mathrm{coupling}} = \hbar g\left(-\cos\theta\sigma_z + \sin\theta\sigma_x\right)\left(ae^{-i\omega t} + a^\dagger e^{i\omega t}\right). \tag{2.39}$$

where $\omega = 2\pi f$ is the frequency of the probe field, $g = \frac{e\alpha}{2\hbar}\sqrt{\hbar\omega_0/C_r}$ the strength of the dipole coupling[9], and $\theta = \tan^{-1}(t/\epsilon)$ the degree of hybridization between the charge states.

The Hamiltonian in Eq. (2.38) can be simplified by applying the rotating wave approximation (in the frame of the double dot). This amounts to only keeping the terms that conserve the number of excitations (e.g., $a\sigma_+$ and $a^\dagger\sigma_-$ with $\sigma_\pm$ the raising and lowering operators of the DQD), reducing Eq. (2.38) to a Jaynes-Cummings Hamiltonian. Now, we can obtain an expression for the reflected probe field using a master equation approach [88, 89]

$$\frac{a_{\mathrm{out}}}{a_{\mathrm{in}}} = \frac{\kappa_{\mathrm{ext}}}{i\left(\omega_0 - \omega\right) + \kappa/2 + i g_{\mathrm{eff}}\chi} - 1 \tag{2.40}$$

with the double dot susceptibility

$$\chi = \frac{g_{\mathrm{eff}}}{\Omega/\hbar - \omega + i\gamma/2}. \tag{2.41}$$

In these equations, $\kappa = \kappa_{\mathrm{ext}} + \kappa_i = \omega_0/Q$ is the total resonator damping rate, composed of internal losses κ_i and external coupling κ_{ext}; γ is the dephasing rate, and $g_{\mathrm{eff}} = g\sin(\theta)$ is the effective coupling strength. These equations are used in chapter 5 to extract the tunnel coupling from the dispersive shift of the resonator.

Lastly, we show the equivalence between cQED in the dispersive regime and the circuit element approach discussed in the previous section. In the dispersive regime, the detuning between the qubit excitation energy and the probe energy is large: $\Delta = \Omega/\hbar - \omega_0 \approx \Omega/\hbar$. In this case, the shift on the resonator frequency is given by $\delta\omega = -g_{eff}^2/\Delta$. Using Eq. (2.36) to relate $\hbar g_{\mathrm{eff}}^2/\Omega$ to C_q, this reduces to

$$\frac{\delta\omega}{\omega_0} = -\frac{C_q}{2C_r}; \tag{2.42}$$

Equal to the expression found by expanding $\delta\omega = 1/\sqrt{L_r\left(C_r + C_q\right)} - 1/\sqrt{L_r C_r}$ for small C_q/C_r.

---

[9] For a double quantum dot this coupling is twice as small as for a Cooper-pair box, because the charge of single electrons is twice as small as the charge of a Cooper-pair, leading to a smaller dipole moment.

3

Methods

Slow is smooth, and smooth is fast

Phil Dunphy

This chapter consists of two parts. In the first part, we describe the measurement technique gate-based RF reflectometry, and give a detailed technical description of the setups for the nanowire experiments. In the second part, we discuss the procedure for fabricating the nanowire devices.

3.1. Gate-based reflectometry

In chapters 5 and 6, we utilize gate-based radio frequency (RF) reflectometry to measure the electron tunneling between quantum dots and islands. In this section, we describe this measurement technique followed by a technical discussion of our measurement setup.

Microwave reflections occur at the interface between two media with a different characteristic impedance. In this thesis, we will use the reflection from the gate electrode of a quantum dot to measure the charge tunneling in our devices. The amplitude A and phase ϕ of the reflected wave are given by the reflection coefficient [90]

$$\Gamma = \frac{Z - Z_0}{Z + Z_0}, \tag{3.1}$$

where $Z_0 = 50\,\Omega$ is the characteristic impedance of the coax cables in the setup, and Z is the combined impedance of the device and the LC tank circuit attached to the gate. In reflectometry, typically the amplitude and phase of the reflected field are measured at a constant probe frequency while control parameters, such as gate voltages and/or the magnetic field, that impact the impedance of the device, are swept.

In quantum dots and islands, the change in impedance is reactive in nature as tunneling processes give rise to an additional parametric capacitive load seen by the gate (see section 2.5). The added capacitance shifts the resonance frequency f_0 of the LC circuit by connected to the gate

$$\Delta\omega = \frac{1}{\sqrt{LC}} - \frac{1}{\sqrt{L\left(C + C_\mathrm{p}\right)}}. \tag{3.2}$$

The frequency shift translates in an amplitude[1] and a phase shift when measured at a constant probe frequency, see Figure 3.1. The phase-roll across the resonance is 2π. Hence large phase shifts can be obtained when the frequency shift exceeds the resonator linewidth $\Delta f > f_0/Q$. Here, Q is the quality factor; it is composed of an internal and an external contribution $Q^{-1} = Q_\mathrm{int}^{-1} + Q_\mathrm{ext}^{-1}$. For our resonators, $Q_\mathrm{ext} \ll Q_\mathrm{int}$, meaning that the coupling to the detection circuit dominates the internal losses. The maximum measurement bandwidth is set by the quality factor $BW = f_0/Q$. Typically, $f_0 \approx 400\,\mathrm{MHz}$ and $Q = 100$ to 200, leading to a maximum bandwidth of 2 to 4 MHz.

The tank circuits used for our experiments are defined by NbTi spiral inductors in combination with the parasitic capacitance of the circuit. The inductors (see Fig. 3.5a for a picture) are made in the group of David Reilly [91]. They are fabricated on a sapphire chip to ensure a stable dielectric environment. Moreover, they are suitable for multiplexing since a single feedline connects to eight inductors ranging from 40 to 420 nH. On-chip bias tees are use to supply a DC offset to the individual

---

[1] An ideal LC resonator has a flat amplitude response as a function of frequency because there is no power dissipation. In practice, however, we always measure a dip in the reflected amplitude at the resonance frequency due to finite losses.

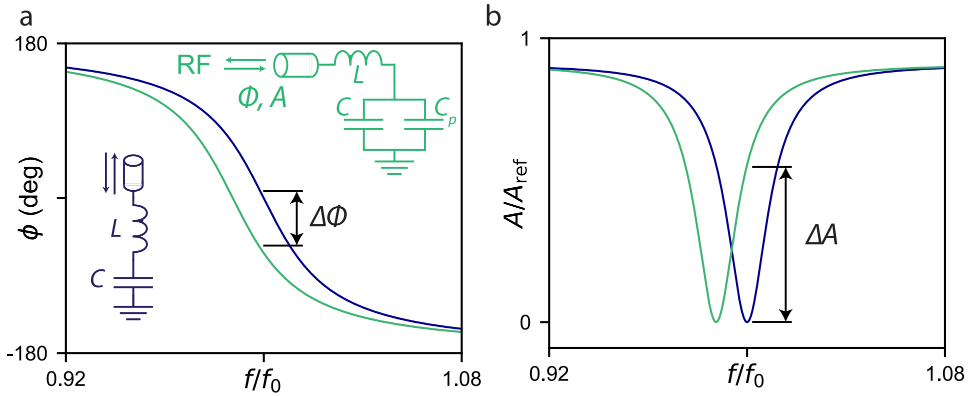

Figure 3.1 – Gate-based RF reflectometry. The resonance frequency of a LC resonator shifts upon increasing the capacitive load, for example, due to electrons tunneling within a double quantum dot. This results in a phase shift **a** and amplitude change **b** of the reflected microwave signal when probed at a constant frequency.

inductors. Finally, the 150 nm thick NbTi film has a large critical magnetic field and is therefore compatible with Majorana zero mode measurements.

3.1.1. Reflectometry setup

In this section, we describe the reflectometry setup used for the dot-island measurements of chapter 6. The setup used for the double dot measurements (chapter 5) is similar albeit with slightly different choices for various components[2]. Roughly, the setup can be separated into three parts: the RF electronics, the DC electronics, and the the printed circuit board (PCB). Figure 3.2 present a schematic circuit of the setup.

The RF carrier signal is generated using R&S SGS100A sources and is routed to the sample via low-loss coax cables. In the fridge, we use silver-plated stainless steal cables above 4 K and superconducting NbTi cables below 4 K (both from coax co). The microwaves are attenuated with a variable attenuator at room-temperature (RUDAT-13G-90) to set the overall power level, and cryogenic attenuators (from XMA) to reduce the thermal noise from room-temperature and to thermally anchor the inner conductor. Moreover, DC blocks are added to various parts of the readout chain to prevent ground loops. The coupled port of a directional coupler (ZFDC-20-S) is used to route the RF tone to the sample and to direct the reflected signal towards the amplification chain. The first stage of this chain is located at 4K and consist of a low-noise amplifier (CITLF3) with a gain of about 30 dB. For reflec-

---

[2] More precisely, we use a custom-made room-temperature amplifier and mixers; high frequency (f_{cutoff}>1 GHz) copper-powder filters and custom-made RC filters instead of the Qdevil filters; an additional DC block (PE8210) before the cryogenic amplifier; a ZEDC-15-2B directional coupling; keithley 2000 DMMs; and SRS830 lockin-amplifiers.

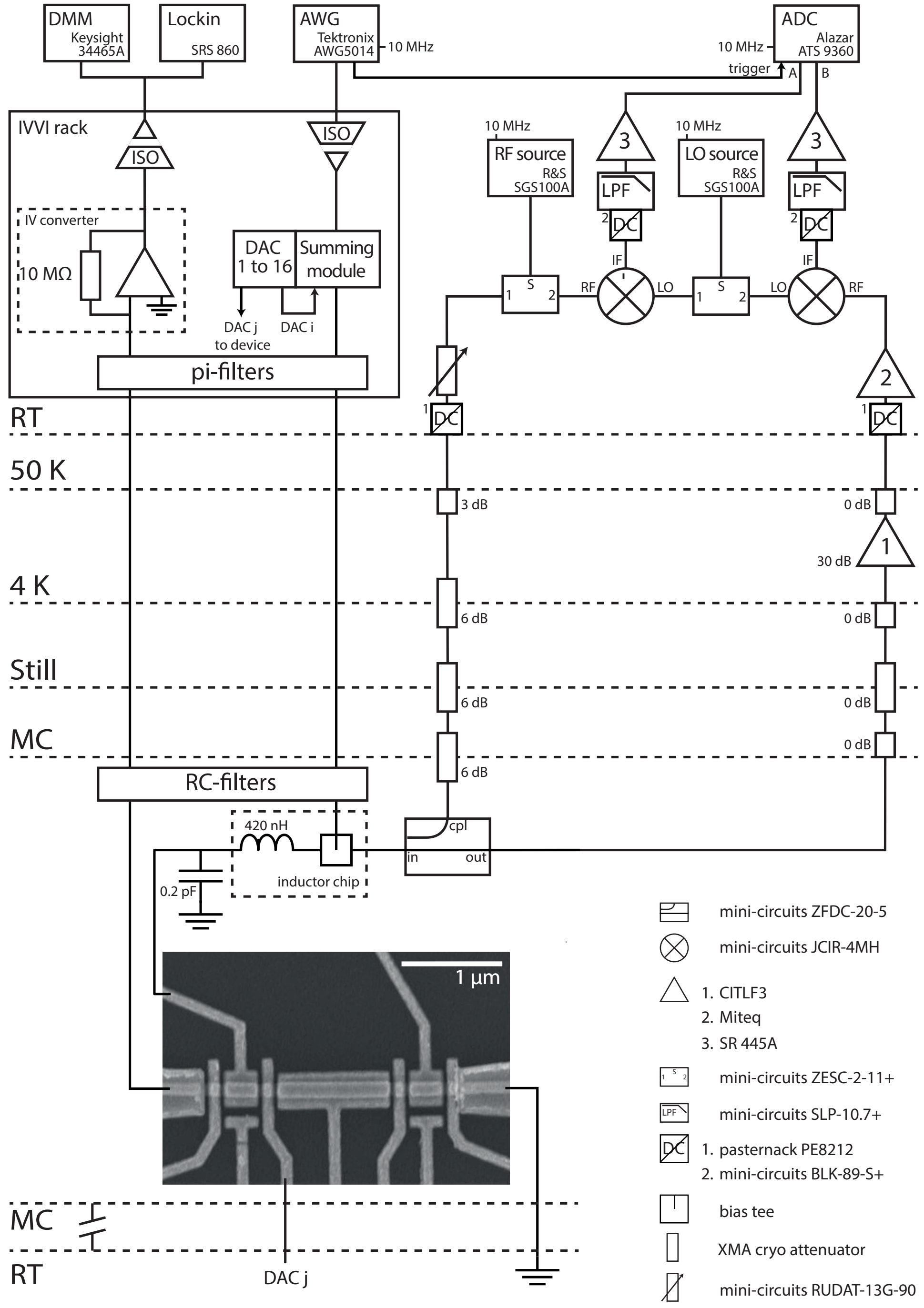

Figure 3.2 – **Reflectometry setup used for the dot-island experiment in chapter 6.** The directional coupler separates the incoming and outcoming RF fields. The reflected signal is amplified and mixed down before its amplitude and phase are extracted using a Fourier transform. DC voltages to bias the gates are added via a bias tee on the inductor chip. The in-house built IVVI rack controls the routing of DC signals and isolates the device from the control electronics. For illustration purposes, only one of the inductors is connected to the device.

tometry measurement, it is crucial that the S_{11} of this amplifier is low ($\lesssim -10$ dB). Furthermore, any attenuation before the first amplification stage strongly increases the noise temperature of the setup and should therefore be avoided. The second amplifier (from Miteq) is located directly after the signal exits the fridge and has a gain of about 36 dB. Subsequently, the carrier is mixed (using JCIR-4MH) with a local oscillator (LO) resulting in an intermediate frequency (IF = RF − LO) and the sum frequency (RF + LO). Typically, IF = 1-10 MHz. The signal is low-pass filtered (f_{cutoff} = 10 MHz) and amplified before it is discretized using an Alazar acquisition card (ATS9360). The amplitude and phase are determined via the fast Fourier transform. To correct for phase drifts, the phase of the reference arm is subtracted.

The DC signals are handed to the sample via an in-house built module called the IVVI rack which is designed by the group of Raymond Schouten [92]. This battery-powered module isolates the device from the control electronics using isolation amplifiers for device signals and opticals control signals. Moreover, it contains 16 low-noise digital-to-analog converters (DACs) which are used to bias the gates and the source of the device. They have a resolution of 61 µV and a range of -2 to +2 V. Voltage sources can be used to increase the resolution of the DACs, and current sources to generated bias currents. Furthermore, IV converters and voltage amplifiers are used to amplify the signal before it is measured using a digital multimeter (Keysight 34465A) and/or a low-frequency lockin amplifier (SRS860); and an arbitrary waveform generator (Tektronix AWG5014) is used to bias the gate with a staircase signal in order to speed up the measurements. Finally, all in- and output signals are filtered using pi-filters with a cutoff frequency of 10 MHz at room-temperature, and several stages of RC filtering at base temperature (using Qdevil filters).

Like the inductor chip, the PCB is supplied by the Reilly group. It consist of a fixed motherboard and a replaceable daughterboard and is equipped with 96 DC lines and 8 RF lines (of which we only use the one connected to the reflectometry circuit). Each of the DC lines contains an additional RC filter, resulting in a combined cutoff frequency of about 50 kHz and a total series resistance of 8.7 kΩ (including the Qdevil filters). The RF lines can also be DC biased via a bias tee on the motherboard which increases the series resistance by 5 kΩ. Furthermore, DC/RF lines are added to the respective inductors via another bias tee on the inductor chip which adds another ≈ 2 kΩ in series.

3.2. Switching current measurements

Here, we briefly describe the setup used for the switching current experiment on the nanowire single-Cooper-pair transistors (SCPTs) presented in chapter 4.

The switching current histograms are measured using a Rigol DG4062 arbitrary waveform generator to supply the waveform of the ramp to the current source which results in a time-dependent current bias of the device characterized by a constant current ramp rate $\mathrm{d}I/\mathrm{d}t$. The voltage across the SCPT is measured in a four-terminal configuration using a voltage amplifier that is isolated from the commercial electronics. A typical current bias waveform together with the resulting voltage are schematically depicted in Figure 3.3a. When the measured voltage crosses the preset voltage threshold V_{th}, the corresponding bias current is recorded using a custom-made sample-and-hold circuit and a Keithley 2000 digital multimeter. This reference voltage is tuned inside the voltage step that separates the supercurrent- from the quasiparticle current branch so that the recorded current measures the switching current. This measurement is repeated N times to acquire the switching current histogram.

Figure 3.3b shows an example of a measured switching current modulation with this protocol.

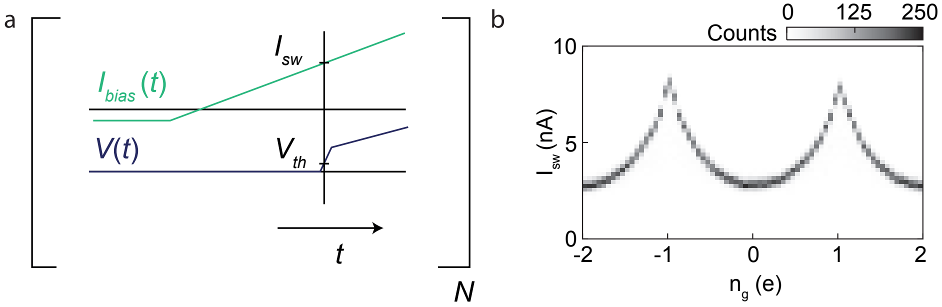

Figure 3.3 – **Switching current histograms.** **a** Protocol for the switching current histograms. The bias current is varied with a constant ramp rate while the voltage across the sample is measured. When this voltage passes a preset threshold voltage, the corresponding bias current is recorded using a sample-and-hold circuit. If the threshold voltage is tuned so that it lies within the voltage step, the recorded current measures the switching current. **b** Modulation of the switching current of a SCPT. For each gate value, the switching current measurement is repeated $N = 500$ times.

3.3. Fabrication of nanowire devices

In this section, we introduce the nanofabrication methods used for the dot-island devices[3] of chapter 6. Besides introducing the fabrication process, the aim of this section is to hightlight important steps taken in its development and point out where improvements could possibly be made with the hope to make it a useful starting point for future nanowire reflectometry devices.

3.3.1. Nanowire growth

The InAs-Al core-shell wires used in this thesis are grown with molecular beam epitaxy (MBE) in the group of Peter Krogstrup in Copenhagen [93]. The InAs wires are grown in the $\langle 0001 \rangle$B-direction. They have a hexagonal cross section with $\{1\bar{1}00\}$ facets. They have a typical width between 80 and 120 nm, a typical length between 5 and 10 µm, and a typical electron mobility between 5000 and 10000 $\mathrm{cm}^2/(\mathrm{Vs})$. The aluminium shell is grown on the wire without breaking the vacuum which results in an epitaxial interface between the InAs and the Al as can be seen in Figure

---

[3] These devices combine superconducting islands (chapter 4) with quantum dots (chapter 5). As such, the methods and recipes discussed here are also applicable for those devices.

3.4a. Since the aluminium is deposited with a directional beam only a fraction of the facets are covered (typical two to three facets), leaving room for adjusting the chemical potential in the wire via electrostatic gating [94]. The clean interface between the InAs and the Al induces a hard superconducting gap (Fig. 3.4b) which was a major advancement in the field of proximizited nanowires [95–97]. Finally, the Al layer is very thin (<10 nm), resulting in a large critical magnetic field necessary for the emergence of MZMs.

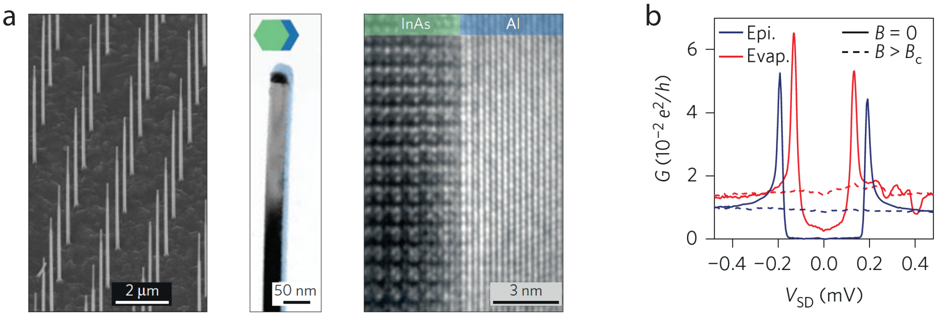

Figure 3.4 – **Hard gap in InAs nanowires with an epitaxially grown shell.** **a** Left: scanning electron micrograph showing the InAs-Al nanowires grown in a regular grid. Middle and right: transmission electron micrographs indicating the epitaxy between InAs and Al. Image obtained from [93]. **b** Comparison of the induced superconducting gap of an evaporated- (red) and an epitaxially grown aluminium shell (blue). Indeed, the latter shows a stronger reduction of the subgap conductance, indicating a hard induced superconducting gap without low-energy subgap states. Image obtained from [95].

3.3.2. Chip layout and nanowire transfer

Intrinsic silicon chips ($\rho > 10\,000\,\Omega\,$cm) covered with 20 nm of LPCVD-deposited SiN_x are used for the reflectometry samples to reduce the parasitic capacitance that sets the resonance frequency. The fabrication starts with patterning 4-inch wafers with e-beam and alignment markers. The wafer is diced into 6.5×6.5 mm^2 chips so that they exactly fit in the cutout on the PCB and no post-fabrication dicing of the chips is required[4]. The marker layout allows for three devices on a chip which results in a reasonable yield while minimizing the amount of design work. Moreover, it leaves room for the resonator chip as can be seen in Figure 3.5a.

Before the nanowires are deposited, the device chip is cleaned with acetone (10 minutes in an ultrasonic bath) and IPA. It could be worthwhile to investigate whether additional cleaning would improve the device quality [98]. Individual nanowires are transferred onto the chip using a micro-manipulator [99]. Care is taken to avoid bending and/or sticking together of the nanowires. Figure 3.5b shows a dark field optical image of the alignment markers together with a single

---

[4] We noticed that post fabrication dicing of nanowire devices with our gate geometry (e.g., a wrap gate separated by a thin layer of AlO_x or SiN_x.) enhances the probability of shorting gates to the nanowires; presumably caused by electrostatic discharge (ESD).

nanowire. This image is used to align the design to the wire. The wires are stored in an argon environment to prevent degradation of their quality[5].

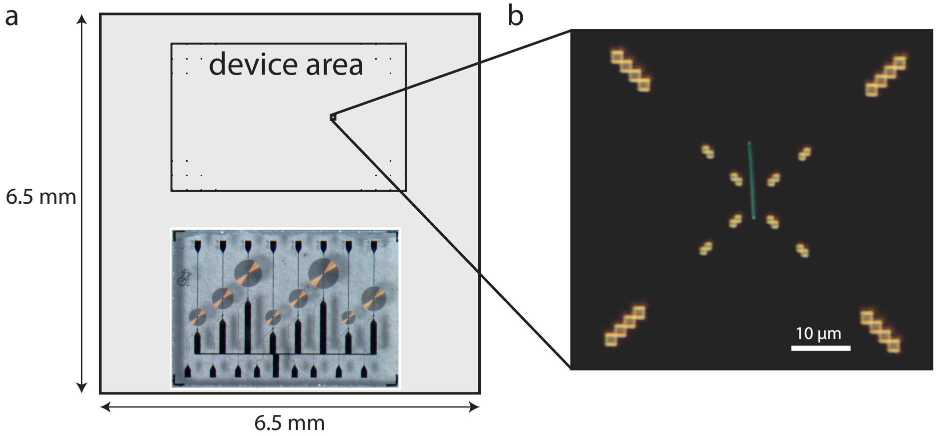

Figure 3.5 – **Chip layout and wire deposition.** **a** The chip layout used for the reflectometry samples. The chip is made from intrinsic silicon and is covered with 20 nm LPCVD SiN_x. The inductor chip is glued on the device chip using PMMA. **b** Dark-field optical image of a single nanowire deposited on a predefined location using a micro-manipulator.

3.3.3. Etching of the aluminium shell

Transene D is used to etch the aluminium shell from the InAs-Al nanowires in order to define the superconducting islands. This etchant was developed to selectively etch Al from GaAs [100]. We optimized the eching recipe to be able to reliably define short junctions which is difficult because of the different etch rates for Al and AlO_x. We achieve an average junction length of 85 nm with a standard deviation of 5 nm (starting from 50 nm lithographically defined windows). Figure 3.6a shows a SEM of a typical test sample and Figure 3.6b the result of an etch test with the optimized recipe. In this recipe, it is key to be able to control the temperature of the etchant. Therefore, we put the glass-coated sensor directly into 100 mL of transene D. In addition, we use a sensitive hot plate (IKA C-MAG HP 10) and controller (IKA ETS-D6). The acid is heated to 48.2 °C while it is gently stirred. We put the sample in the etchant for 12 s and rinse thoroughly in water afterwards.

Despite its selectivity for GaAs, transene D does slowly etch InAs. Therefore, it could be worthwhile to investigate different chemicals; possible candidates are BOE (or HF), sulphur, or MF321 (or TMAH).

---

[5] A quick calculation shows that roughly 10^{10} wires fit on a 1×1 cm^2 growth chip. Still, we regularly use new chips either because wires degrade or because improved wires growths are available.

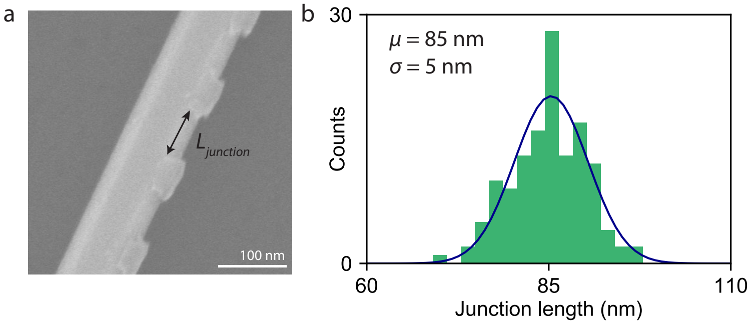

Figure 3.6 – **Calibration of the transene D etch. a** Scanning electron micrograph of a test sample used to calibrate the etching recipe. The remaining aluminium patches are visible on the top-right facet of the wire. **b** Histogram of the junction length obtained by analyzing 134 junctions made using the optimized recipe. The histogram shows that we can reliably make 85 nm long junctions.

3.3.4. Ohmic contacts

The native oxide of the InAs has to be removed to make ohmic contacts to the nanowire. We remove this oxide with 30 seconds of *in situ* argon milling before depositing a 10/140 nm Ti/Au layer. We calibrated the argon mill by etching unoxidized Al, where we measure an etch rate of -0.6 Å/s. Typically, the room temperature resistance is 1 and 5 MΩ after this step of the fabrication.

3.3.5. Gating the nanowire

The dots and islands are defined by locally depleting the nanowire via electrostatic gating. The lever arm of a gate is primarily determined by its geometry and dielectric environment. We want a large lever arm for the readout gate to increase the dispersive signal which scales as $C_q \propto \alpha^2$ (see Eq. (2.36)). In addition, the gate-hysteresis should be small to be able to efficiently tune up the dots. We chose for a wrap-around gate design to maximize the gate lever arm.

First, we tested the continuity of these gates by measuring the resistance of a short crossing the wire. For the dielectric layer, we considered sputtered $\mathrm{SiN_x}$ and ALD $\mathrm{AlO_x}$. Typical pinchoff curves for such gates are shown in Fig 3.7a and b. Figure 3.7a shows that gates with a 20 nm $\mathrm{SiN_x}$ layer[6] can have low hysteresis. However, we noticed that this recipe was not reproducible between fabrication runs. Figure 3.7b contains a typical pinchoff curve for a gate separated by a 10 nm thick $\mathrm{AlO_x}$ layer. These gates generally have a lower value for the threshold voltage than the $\mathrm{SiN_x}$ gates indicating a stronger coupling to the nanowire channel. Moreover, the $\mathrm{AlO_x}$ gates have negligible hysteresis and their fabrication was found to be reproducible. Therefore, we use $\mathrm{AlO_x}$ for the reflectometry devices.

We note that after the deposition of the dielectric the wire resistance typically drops to 5 to 10 kΩ.

---

[6] We found that 30 nm thick $\mathrm{SiN_x}$ films give similar results.

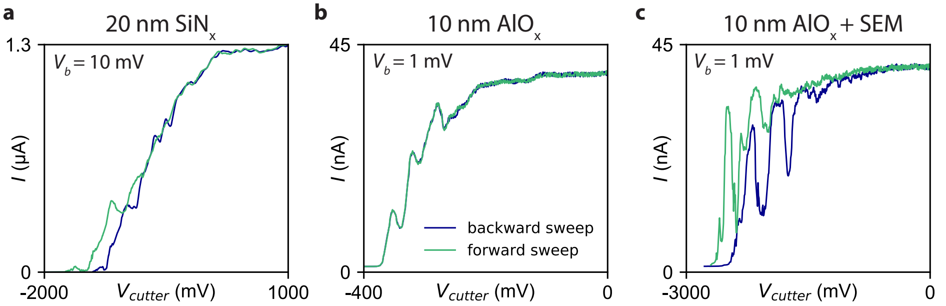

Figure 3.7 – Typical pinchoff curves for gates with different dielectric layers. **a** SiN_x can result in gates with small hysteresis. **b** Gates on AlO_x generally have negligible hysteresis and a small voltage span between saturation and pinchoff. **c** After SEM inspection the gating properties can degrade; the hysteresis increases and the threshold voltage shifts towards more negative voltages. Note that the difference in saturation current between the panels is also influenced by the series resistance of the setup and the applied bias voltage.

3.3.6. Post processing

After the gate fabrication, the devices are ready to be measured. Often it is useful to inspect the devices using SEM to check whether there were no shifts during the lithography of the gates. However, we observed an increase in the hysteresis of the pinchoff curves after SEM as is illustrated in Fig. 3.7c. Moreover, we noticed that dicing the sample increased the probability of shorting a gate to the nanowire. Therefore, we avoid SEM and dicing after the dielectric deposition.

For the cooldown, the chip is mounted on the daughterboard of the PCB. Then, the resonator chip is placed on top of the device chip. PMMA is used as glue for both steps. Next, a device is wire bonded to the DC lines on the PCB and the inductors on the resonator chip. The bond wires to the inductor should be as short as possible to minimize the parasitic capacitance of the tank circuit. Finally, the PCB is screwed into the cold finger of a dilution refrigerator.

4

Magnetic-field-dependent quasiparticle dynamics of nanowire single-Cooper-pair transistors

Parity control of superconducting islands hosting Majorana zero modes (MZMs) is required to operate topological qubits made from proximitized semiconductor nanowires. We test this control by studying parity effects in hybrid InAs-Al single-Cooper-pair transistors (SCPTs) to evaluate the feasibility of this material system. In particular, we investigate the gate-charge modulation of the supercurrent and observe a consistent $2e$-periodic pattern indicating a general lack of low-energy subgap states in these nanowires at zero magnetic field. In a parallel magnetic field, an even-odd pattern develops with a gate-charge spacing that oscillates as a function of field demonstrating that the modulation pattern is sensitive to the presence of a single bound state. In addition, we find that the parity lifetime of the SCPT decreases exponentially with magnetic field as the bound state approaches zero energy. Our work shows that aluminum is the preferred superconductor for future topological qubit experiments and highlights the important role that quasiparticle traps and superconducting gap engineering would play in these qubits. Moreover, we demonstrate a new means by which bound states can be detected in devices with superconducting leads.

This chapter is based on J. van Veen, A. Proutski, T. Karzig, D. I. Pikulin, J. Nygård, P. Krogstrup, A. Geresdi, L. P. Kouwenhoven, and J. D. Watson, Magnetic-field-dependent quasiparticle dynamics of nanowire single-Cooper-pair transistors, *Physical Review B* **98**, 174502 (2018).

4.1. Introduction

The interplay of charging energy E_C and the superconducting gap Δ leads to the surprising result that the electrical transport in a mesoscopic superconducting island containing a macroscopic number of electrons is sensitive to the addition or removal of a single electron [55–57, 101]. This parity effect has been extensively studied in Al-AlO$_x$ SCPTs by measurements of a $2e$-periodic gate-charge modulation of Coulomb peak spacings, ground state charge, and switching currents [58–60, 79, 102–106]. In recent experiments, the presence of MZMs in hybrid semiconductor-superconductor nanowires was inferred from a field-induced $1e$ Coulomb blockade periodicity, illustrating the utility of this periodicity in understanding the low-energy spectrum of superconducting islands [41, 52–54, 64, 82, 107, 108]. In contrast with these previous studies which utilized devices with normal metal leads, we investigate parity effects in gate-tuneable nanowire SCPTs which have superconducting leads by studying the junction gate, temperature, and parallel magnetic field dependence of the switching current modulation. These experiments not only give new insights into quasiparticle dynamics but also represent a first step towards implementing recent Majorana-based qubit proposals which require Josephson coupling to the leads to enable parity-to-charge conversion for MZM manipulation and readout [15, 16, 39, 81, 109].

The Hamiltonian of a SCPT consists of three terms: $H = H_C + H_J + H_{\mathrm{BCS}}$. The Coulomb term, $H_C = E_C(n - n_g)^2$, stabilizes the excess charge n on the island which can be changed by varying the gate-charge n_g. The effective charging energy $E_C = e^2/2C$ is given in terms of the electron charge e and a generalized capacitance C that takes into account the geometric capacitance and possible renormalization effects due to tunneling of quasiparticles [110–114]. The Josephson term for symmetric junctions $H_J = -E_J \cos(\phi/2) \sum_n |n\rangle\langle n+2| + h.c.$, with E_J the Josephson energy and ϕ the superconducting phase difference across the island, couples adjacent, equal-parity states and results in energy level anti-crossings when states with the same parity are degenerate. The third term describes the spectrum of the gapped BCS quasiparticles resulting in an energy offset Δ for the odd ground state due to an unpaired electron in the superconductor. Figure 4.1a shows the resulting band structure of a SCPT. The corresponding gate-charge modulation of the critical current is shown in Fig. 4.1b. We denote the amplitude of the (even) ground state charge dispersion $E_{\mathrm{gs}}(n_g)$ with $\delta E_{\mathrm{eo}} = E_{\mathrm{gs}}(n_g = 1) - E_{\mathrm{gs}}(n_g = 0)$. When $\Delta > \delta E_{\mathrm{eo}}$ the ground state is always even. Consequently, the switching current modulation will be $2e$-periodic at $T = 0$ in this simple model.

Quasiparticle poisoning, however, affects this $2e$-periodic modulation. Previous studies have illustrated several important timescales, namely the (un)poisoning rate $\Gamma_{\mathrm{in,(out)}}$ at which quasiparticles in the lead tunnel to the island (or vice versa), the non-equilibrium unpoisoning rate $\Gamma_{\mathrm{out}}^{\mathrm{neq}}$ at which non-equilibrium quasiparticles on the island tunnel out to the leads, and the relaxation rate $1/\tau$ at which non-equilibrium quasiparticles on the island relax to the gap edge or subgap states [72, 73, 77, 115]. While the relaxation is important for the quasiparticle dynamics, the thermodynamics of the system can be described by equilibrium poisoning and unpoisoning rates Γ_{in} and Γ_{out} alone; therefore, we leave the implications of relaxation in our devices to the discussion section below. The ratio $\Gamma_{\mathrm{in}}/\Gamma_{\mathrm{out}}$ gives the relative occupation between the even and odd parity states in equilibrium $p_{\mathrm{odd}}/p_{\mathrm{even}}$. If $\Gamma_{\mathrm{in}}/\Gamma_{\mathrm{out}} \approx 1$ as is expected to occur at high temperature, the switching current modulation deviates from $2e$ periodicity and exhibits a $1e$ periodicity instead.

Figure 4.1c presents a scanning electron micrograph (SEM) of one of our SCPTs, and a 3-dimensional schematic of the device is shown in Fig. 4.1d. The SCPTs are fabricated from InAs nanowires covered with a thin aluminium shell on two of their facets. It has been shown that this material combination results in a hard, induced superconducting gap in the nanowire [93, 95]. The aluminium shell is etched in two regions along the nanowire in order to define the island together with the two Al-

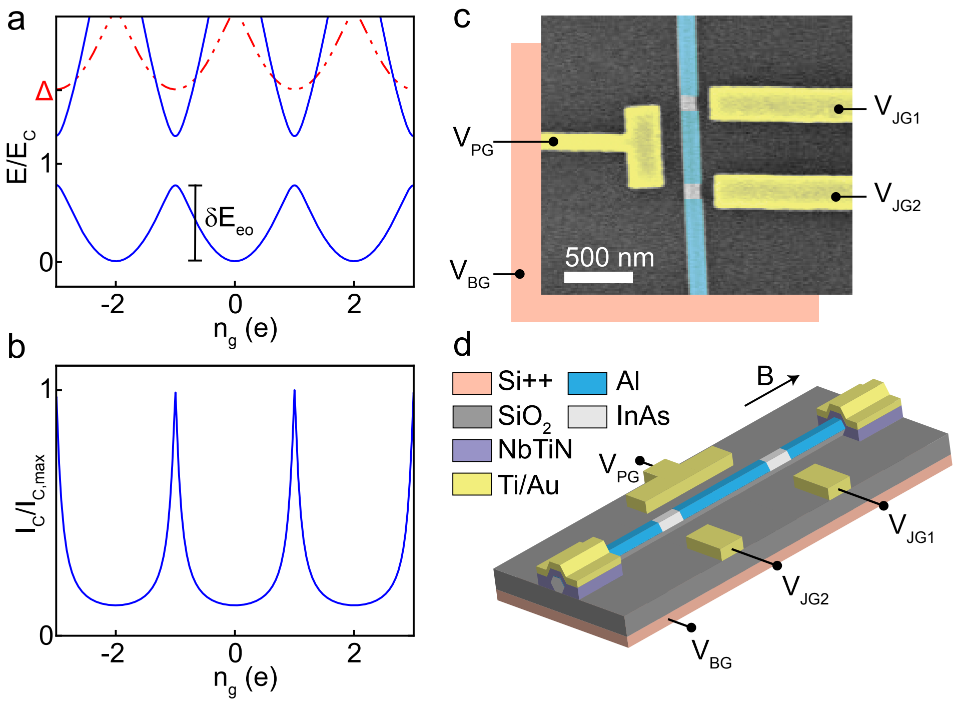

Figure 4.1 – **Theoretical background and device layout.** **a** The band structure of a SCPT as a function of gate-charge n_g for $\phi = 0$, $\Delta/E_C = 1.5$, and $E_J/E_C = 0.25$. The charge dispersion of the odd parity branch (in red) is displaced from the even parity branch (in blue) by the superconducting gap Δ and $\delta n_g = 1$. The amplitude of the ground state charge dispersion is denoted by δE_{eo} **b** The corresponding critical current modulation as a function of n_g. **c** A false-coloured scanning electron micrograph of a nanowire SCPT. The etched regions in the Al shell define the junctions and the island. By applying voltages to the electrostatic gates, we can tune the chemical potential (with V_{BG}), the junction transparency (with $V_{JG1,2}$) and the charge occupation of the island (with V_{PG}). **d** 3-dimensional device schematic. The nanowire is deterministically placed on top of a SiO$_2$/Si++ substrate. It is then contacted by a stack of NbTiN and Ti/Au 1 µm away from the etched regions. Finally, the local gates are deposited. The arrow indicates the direction of the magnetic field for the data presented in Fig. 4.4.

InAs-Al Josephson junctions. The wire is contacted 1 µm away from each junction by NbTiN/Ti/Au contacts which are expected to act as quasiparticle traps due to the presence of normal metal and the large subgap density of states in NbTiN [116]. Previous studies have shown the effectiveness of such traps to reduce the quasiparticle density [60, 70, 77]. Voltages V_{JG1} and V_{JG2} applied to the side gates tune the transparency of the weak links while the plunger gate voltage V_{PG} tunes the chemical potential of the island, and the global backgate voltage V_{BG} tunes the chemical potential of the whole system. The SCPTs are mounted to the cold finger of a dilution refrigerator with a base temperature of 27 mK. We report on six devices in total; in the main text, we present data on a device with a 500 nm long island (see Table 4.S1 of the Supplemental Material for an overview of all the devices). Unless otherwise indicated, the presented data were obtained at 27 mK and at zero field.

4.2. Results

4.2.1. Coulomb blockade and switching current histograms

We first tune the device into Coulomb blockade by increasing the heights of the barriers separating the island from the leads. The clear, regular Coulomb diamonds shown in Fig. 4.2a demonstrate the creation of a single, well-defined island. Moreover, a 1e-periodic conductance modulation appears when $e\,|V_b| > 4\Delta$ and transport through the island is dominated by quasiparticles which enables us to identify the gate voltage periodicity corresponding to 1e [117]. The current at lower bias voltages is too small to resolve in the Coulomb blockade regime since it involves Cooper pair transport and is therefore higher order in the tunneling. Finally, we extract the superconducting gap $\Delta = 180\,\mu\text{eV}$ and the geometric charging energy $E_C^0 = 1.5\,\text{meV}$ from the observed diamonds.

In order to generate a measurable supercurrent, we lower the barriers in order to increase E_J which simultaneously suppresses δE_{eo}. The switching current is recorded by triggering on the voltage step in the I-V curve as illustrated in Fig. 4.2c; this is repeated N times for each n_g to gather statistics, typically $N = 100$ to 500. Figure 4.2b shows the resulting switching current histogram which is 2e-periodic, indicating that in this regime the charge dispersion has decreased at least an order of magnitude to the point that $\delta E_{\text{eo}} < \Delta$, consistent with the observed charging energy renormalization in a nanowire island with normal leads [107].

To establish that our observed 2e periodicity is robust, we investigate the gate-charge modulation for a wide range of gate settings, as is shown in Fig. 4.2d. We characterize each gate setting by the normal state resistance of the device. Figure 4.2d shows that the modulation is observed for R_N ranging from 5.8 to 19.6 kΩ. At $R_N = 5.8\,\text{k}\Omega$, the switching current was only modulated by 5%, indicating that the device is in the Josephson dominated regime where $E_J > \delta E_{\text{eo}}$.

The other devices behave similarly as can be seen in Fig. 4.S1 of the Supplemental Material. Five out of the six measured SCPTs show a 2e-period modulation robust over different gate settings. The remaining SCPT (device 5) exhibits an even-odd pattern, indicating that $\delta E_{\text{eo}} > \Delta$. Nevertheless, the robustness of the 2e-signal across gate settings and devices suggests a general lack of low-energy subgap states inside the islands at zero field, consistent with the hard gap observed in bias spectroscopy experiments which locally probe the density of states [35, 95].

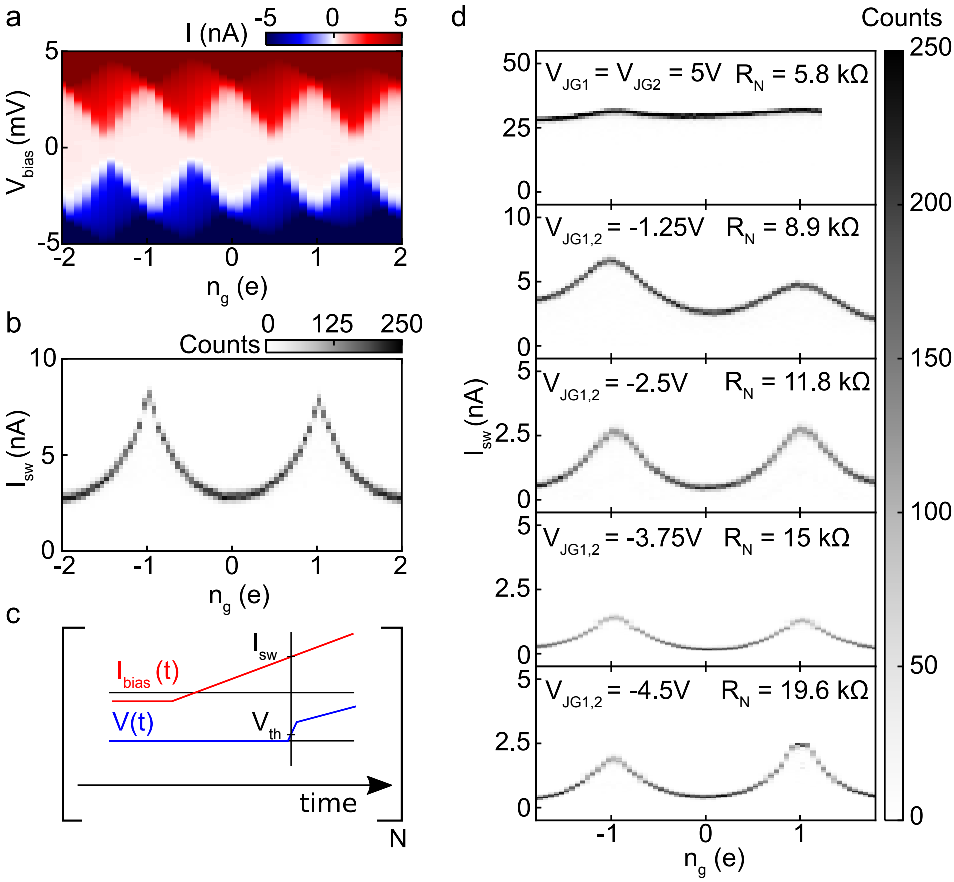

Figure 4.2 – **Gate dependence of the 2e-periodic switching current modulation.** **a** Coulomb diamonds measured in the strongly Coulomb-blockaded regime with Δ = 180 μeV and E_C^0 = 1.5 meV. **b** Histogram of the 2e-periodic switching current I_{sw} in the weakly Coulomb-blockaded regime, indicating that $\Delta > \delta E_{\rm eo}$. At this gate setting, V_{JG1} = -4.1 V and V_{JG2} = -5.7 V, R_N = 14.8 kΩ. **c** Schematic representation of the current ramp (in red) used to obtain the I_{sw} histograms and the resulting voltage across the SCPT (in blue). The switching current I_{sw} is recorded when the voltage drop on the SCPT reaches a threshold value V_{th}. **d** Switching current histograms for varying normal state resistance. The normal state resistance is calculated as the average over the n_g range at high bias. Note the change of vertical scale for the two topmost panels. The peak height asymmetry seen for R_N = 8.9 kΩ and R_N = 19.6 kΩ is due to cross coupling between the junctions and V_{PG}.

4.2.2. Temperature dependence and modeling

To gain insight into the relevant poisoning mechanisms of the SCPT, we measure the temperature dependence of the $2e$-periodic switching current modulation at $R_N = 14.8\,\mathrm{k\Omega}$. As can be seen in Fig. 4.3a, we observe that the $2e$ periodicity persists up to $T \approx 189$ mK at which point the oscillations develop local maxima at even n_g values and finally become fully $1e$-periodic for $T^* \approx 300$ mK. This is consistent with an expected level spacing of the Al shell δ of a few mK when using the estimate for vanishing charge dispersion $k_B T^* = \Delta/\ln(\Delta/\delta)$ [118]. For comparison to the histograms, Fig. 4.3b shows $\mathrm{d}V/\mathrm{d}I$ data taken over the same temperature range. At elevated temperatures, the $\mathrm{d}V/\mathrm{d}I$ characteristics show a similar behavior as the histograms including the onset of local maxima at even n_g. This can be explained by self-averaging that takes place in the overdamped regime due to a succession of multiple switching and retrapping events. Indeed, we note that for $T > 189$ mK, the $\mathrm{d}V/\mathrm{d}I$ traces show negligible hysteresis, indicating that the SCPT is in the overdamped regime. At low temperatures, the junction enters the underdamped regime where a single phase slip can drive the junction normal, which leads to increased fluctuations in the $\mathrm{d}V/\mathrm{d}I$ data at base temperature.

Our modeling of the $\mathrm{d}V/\mathrm{d}I$ data, outlined in Supplemental Material dection 4.5.1, focuses on the overdamped regime. We identify two limiting cases, depending on the ratio of the parity switching times controlled by $1/\Gamma_{\mathrm{in}}$, $1/\Gamma_{\mathrm{out}}$ and the response time of the SCPT given by the Josephson time constant $\tau_J = \hbar/2eI_cR_J$ [119], with R_J the effective shunt resistance of the device and I_c the critical current. For slow parity switches, one expects a double peak structure in the $\mathrm{d}V/\mathrm{d}I$. In contrast, we observe a parity-averaged single peak in the $\mathrm{d}V/\mathrm{d}I$ which shows that at high temperatures the SCPT is in the fast parity switching regime $\Gamma_{\mathrm{in}}, \Gamma_{\mathrm{out}} \gg 1/\tau_J$. At $T \approx 189$ mK where the SCPT transitions into the overdamped regime, $R_J \approx 180\,\Omega$ and $I_c \approx 3$ nA leading to $\tau_J \approx 1$ ns in our experiment.

Given the fast (un)poisoning at high temperature, we model the observed switching currents as the weighted sum of the switching current of the even and the odd parity states, with the relative probabilities governed by the free energy difference of the two states. Our model includes the charging energy of the island, Josephson coupling of the island to the leads, and the entropic factor associated with bringing a quasiparticle into the island; see Supplemental Material section 4.5.2 for a more detailed discussion. We note that though the fast (un)poisoning is a necessary assumption to fit the data at high temperature $T > 189$ mK, at low temperatures the probability to find the system in the odd state becomes negligible, i.e. $p_{\mathrm{odd}}/p_{\mathrm{even}} \propto \exp(-(\Delta - \delta E_{\mathrm{eo}})/k_B T) \to 0$ for $\Delta > \delta E_{\mathrm{eo}}$. Thus, for low temperatures the system is essentially only in the even state which yields the $2e$-periodic histograms of Fig. 4.3a (v).

The fitting gives approximate values of the Δ, E_J, and E_C. These values have error bars of the order of half of their values due to the weak parameter dependence of the fitting function. The fitted value of the superconducting gap $\Delta \approx 220\,\mu\mathrm{eV}$ is, within its error bar, consistent with the value obtained from the Coulomb diamonds in Fig. 4.2a. Similarly, the fitted $E_J \approx 43\,\mu\mathrm{eV}$ is consistent with the observed switching current. The fitted effective $E_C \approx 160\,\mu\mathrm{eV}$, however, is smaller than E_C^0

extracted from the Coulomb diamond data in Fig. 4.2a. This indicates that, in the regime of open barriers, E_C is significantly renormalized by virtual quasiparticle tunneling processes relative to the geometric charging energy [110–114]. The set of consistent fit parameters, together with an excellent fit of the model to the observed switching current dependence on n_g, supports the validity of the model and the assumption of fast (un)poisoning at high temperatures. Similar fitting results for device 2 strengthen this conclusion, see Supplemental Material Fig. 4.S4.

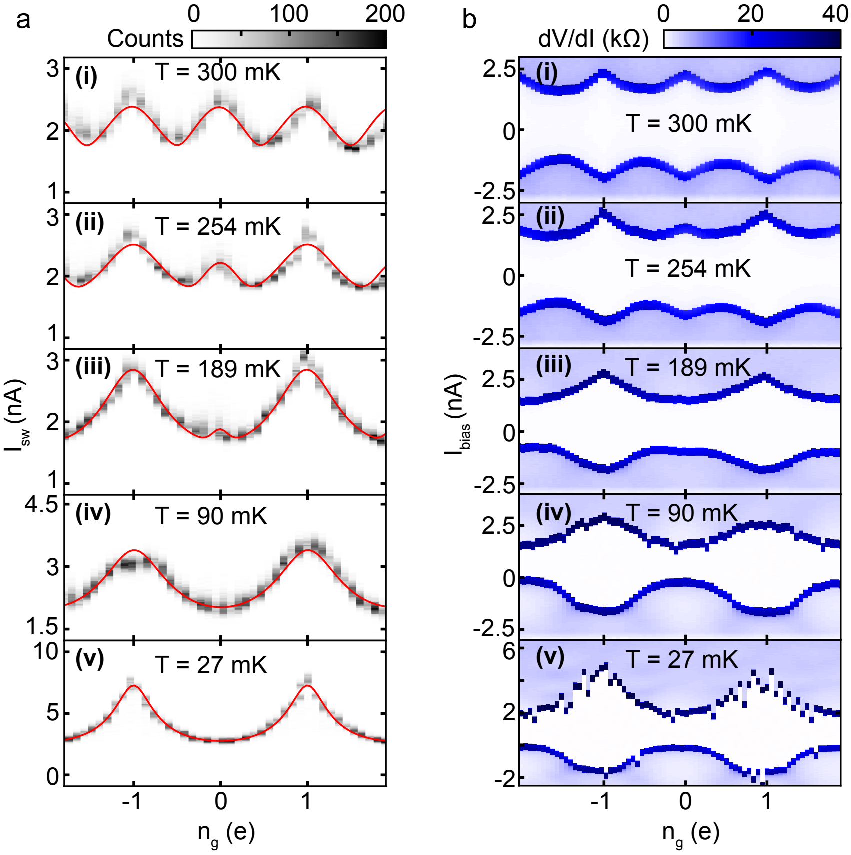

Figure 4.3 – **Temperature dependence.** **a** Switching current modulation as a function of temperature. The experimental histograms shown in grayscale are overlaid by the theoretical fit to the average switching current $\langle I_{\mathrm{sw}} \rangle$ (red curves). Individual fits are for different values of Δ, E_J, and E_C. The average values for resulting the parameters are $\Delta \approx 220\,\mu\mathrm{eV}$, $E_J \approx 43\,\mu\mathrm{eV}$, and $E_C \approx 160\,\mu\mathrm{eV}$. **b** $\mathrm{d}V/\mathrm{d}I$ data for the same temperature range as in **a** obtained from numerical derivation of the I-V curves. The current bias is swept from negative to positive values, hence, switching (retrapping) occurs at positive (negative) bias. At elevated temperatures, the overdamped $\mathrm{d}V/\mathrm{d}I$ data shows a similar behavior as the histograms in **a** with local maxima appearing at even n_g at $T \approx 189$ mK and a fully $1e$ periodic modulation at $T^* \approx 300$ mK. At low temperatures the junction is in the underdamped regime as indicated by the asymmetric $\mathrm{d}V/\mathrm{d}I$, and the increased fluctuations due the absence of self-averaging.

4.2.3. Parallel magnetic field dependence

Next, we study the effect of a parallel magnetic field on the switching current modulation. In particular, we tune the gates such that $R_N = 12.9\,\mathrm{k\Omega}$, and I_{sw} shows a $2e$-periodic modulation at zero field, as is shown in Fig. 4.4b. The $2e$ periodicity implies that $\Delta > \delta E_{\mathrm{eo}}$ and thus that the ground state is always even. As a magnetic field is applied along the nanowire axis, the spinful, odd-charge states are split by the Zeeman energy, thereby reducing the minimal single-particle excitation energy E_0 of the island. Here, we consider a bound state with energy E_0. This state is residing in the island since its energy is modulated by n_g [52]. The parity-dependence of the bound state energy suggests that its origin is superconductivity-related. Moreover, the effective g-factor of a bound state residing partially in the InAs nanowire may be larger than that of the states in the Al shell [65, 66]. This is why in Fig. 4.4a the bound state energy is detached from the quasiparticle continuum for finite magnetic fields. Interestingly, when the applied field is large enough so that $E_0 < \delta E_{\mathrm{eo}}$, the parity of the ground state around $n_g = \pm 1$ changes to odd. During the retrapping process of the switching current measurement, the system tends to be reset to the ground state, indicated by the general lack of bimodal switching current distributions in our data. Hence, the corresponding parity-flip shows up as a dip in the switching current modulation around odd n_g, causing an even-odd pattern. Figures 4.4c and 4.4d show examples of this even-odd structure in the switching current modulation measured at 250 mT and 300 mT, respectively.

We investigate the field dependence of this even-odd pattern in more detail by defining the length in gate-charge over which the even (odd) state is stable as S_{even} (S_{odd}). In Fig. 4.4e these spacings are tracked as a function of the magnetic field using both switching current histograms and I-V measurements, see Fig. S6 and S7 of the Supplemental Material for the representative data. The even (odd) data points are obtained by averaging over 2 (3) successive spacings. Earlier studies performed in metallic superconducting islands found a monotonous drop in S_{even} [58–60, 120]. In contrast, we find an oscillating behavior in the even and odd spacings with the first crossing at 420 mT. After the first crossing, the spacings oscillate around $1e$ with increasing oscillation amplitude. The crossings indicate a closing and reopening of the energy gap for single-particle excitations in the island. Therefore, we conclude that the oscillating pattern is caused by the field-induced zero energy crossings of a single bound state that is detached from the continuum as is illustrated in Fig. 4.4a.

Similar to Fig. 4.3, the histograms and I-V characteristics mostly coincide. For small fields below 200 mT, however, the histograms indicate an even ground state, while the slower I-V traces display an even-odd pattern, see Fig. 4.4e. This discrepancy occurs because the slower I-V measurements are sensitive to trapping events of quasiparticles in the island [115]. The latter occur since even in the absence of subgap states the island acts as a metastable trap with energy δE_{eo} below the gap of the superconducting lead around odd n_g. In rare cases, the metastable state becomes occupied long enough by quasiparticles to cause switching to the resistive state.

In addition, we measure the parity lifetime of the SCPT in a parallel field by performing slow histogram measurements while fixing the gate-charge at $n_g = 1$ so that the extracted lifetime corresponds to poisoning of the even state [104, 116]. For representative histograms see the lower inset of Fig. 4.4f and Fig. 4.S7 of the Supplemental Material. At $n_g = 1$, we expect the worst-case scenario for poisoning since the energy difference between the even and odd state is maximal (i.e. favoring the odd state). We observe that this lifetime decreases exponentially with field between 225 and 300 mT, see Fig. 4.4f. We are limited to this intermediate field range because the lifetime is too large to obtain useful statistics at lower fields and too small to be captured by the bandwidth of the measurement electronics at larger fields. Still, by extrapolating the lifetime to 415 mT where $S_{\text{even}} = S_{\text{odd}} = 1e$, one can estimate the parity lifetime when the bound state is at zero energy to be ≈ 1 ns.

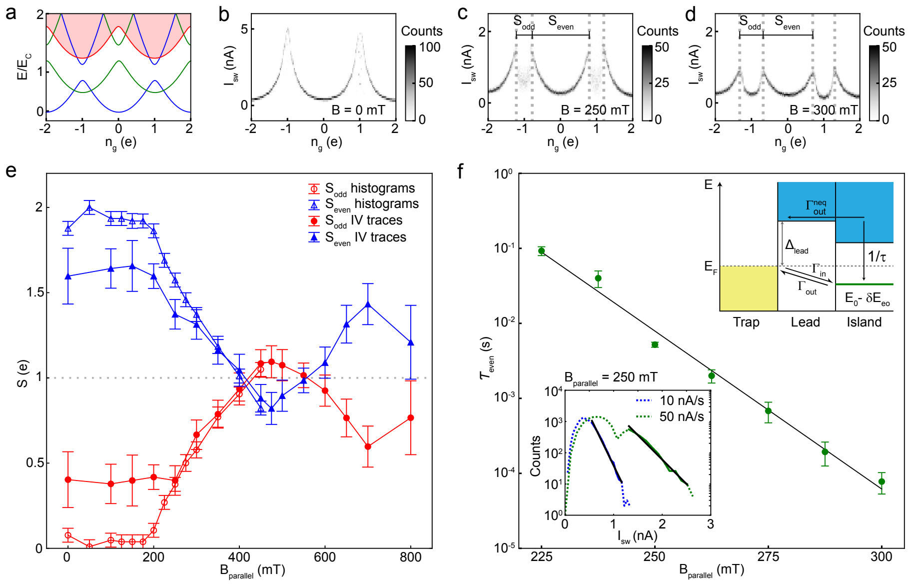

Figure 4.4 – **Parallel magnetic field dependence.** **a** The energy spectrum of a SCPT at finite magnetic field. The blue lines indicate the ground and first excited state of the even parity branch. The odd parity ground state is shown in red with the shaded red region emphasizing the quasiparticle continuum on the island. The green curves indicate the presence of a bound state on the island with energy $E_0(B)$ leading to an even-odd structure of the ground state when $E_0 < \delta E_{\text{eo}}$ **b-d** Switching current histograms at 0 mT, 250 mT, and 300 mT showing the field evolution of the even-odd structure. **e** The even and odd spacings as a function of the parallel magnetic field obtained from both histograms and I-V traces. The observed crossing at 420 mT and subsequent oscillation is attributed to the presence of an bound state that oscillates about zero energy as a function of magnetic field while the superconducting bulk on the island remains gapped. For the most part switching current histograms and I-V characteristics give the same spacings. At low fields, the slow I-V measurements pick up rare poisoning events and thus do not recover full $2e$ periodicity **f** The even parity lifetime at $n_g = 1$ as a function of the magnetic field. The solid line is a guide to the eye indicating an exponential dependence. The lower inset presents a typical dataset used for the extraction of τ_{even}. The upper inset shows a schematic representation of the energy needed to add a single quasiparticle to different parts of the device.

4.3. Discussion

We begin by noting that the growth of the even-odd spacing oscillation as a function of field seen in Fig. 4.4e is reminiscent of one of the proposed signatures of overlapping Majorana zero modes [40]. However, this increasing oscillation amplitude was only observed in a narrow gate range in our device, as is illustrated in Fig. 4.S8 of the Supplemental Material. This makes it difficult to map the amplitude of the first oscillation to a Majorana overlap, as was done in Ref. [41]. From our results, we can only conclude that if this oscillation is indeed due to the presence of overlapping MZMs, the topological portion of the device parameter space is rather small. Nevertheless, mapping the even-odd peak spacing in this manner could be used in future experiments to signal the transition to the topological regime in devices with superconducting leads such as the ones proposed in Refs. [16, 39, 109]. This could be an attractive alternative to gap-edge spectroscopy [121–124] as a signature of the topological regime in these all-superconducting systems.

We also note that the splitting of the $2e$-signal into an (oscillating) even-odd signal is not always observed. Measurements performed on device 4, which has a 3 μm-long island, show a sharp transition of the $2e$-signal to the $1e$-signal at a parallel field of 100 mT, similar to the behavior observed while increasing the temperature in device 1, see Fig. 4.S9 in the Supplemental Material. This field evolution of the I_{sw} modulation indicates that the SCPT is in the fast (un)poisoning limit with $\Gamma_{\text{in}}/\Gamma_{\text{out}} \approx 1$, possibly caused by a field-induced softening of the superconducting gap in the island and/or leads.

To understand the exponential decrease of the even state lifetime with field seen in Fig. 4.4f, we model the system as an island connected to a gapped superconducting lead in contact with a normal metal quasiparticle trap as is shown in the upper inset of Fig. 4.4f. In the field range where we measure the lifetime, the observed even-odd pattern indicates that the energy difference between the odd and even state at $n_g = 1$ is always negative, as also depicted in Fig. 4.4a and the inset of Fig. 4.4f. Therefore, at $n_g = 1$ poisoning is only prevented by the quasiparticle filtering effect of the superconducting gap in the leads. Quasiparticles can cross this gap in two ways: by thermal excitation to the gap edge or by tunneling through the gap. Both processes are exponentially suppressed by a factor that scales with the size of the gap in the leads Δ_{lead}. Quantitative estimates of the relative strength of the tunneling and thermal activation contributions require a microscopic knowledge of the device. Still, both processes lead to an exponential dependence of the lifetime with field since $\Delta_{\text{lead}}(B) = \Delta_{\text{lead}}(0) - \frac{1}{2} g\mu_B B$. In either case, the filtering effect should be enhanced by increasing the length of the superconducting leads as well as by increasing Δ_{lead}. Since recent studies indicate that the size of the proximitized gap in semiconducting nanowires is gate-tunable [65, 66], we suggest enhancing this filtering effect by locally gating the leads of the SCPT. Additionally, the length of the leads could be varied in order to investigate the proximity effect of the traps on the gap in the leads [77, 125].

Next, for a Majorana-based qubit one is primarily concerned with poisoning events which change the state of the qubit - namely, poisoning of the MZMs [71]. If direct tunneling from the quasiparticle trap is the dominant poisoning mechanism, the subgap state is expected to be directly poisoned since it is the lowest energy state on the island. In this case, the measured τ_{even} in Fig. 4.4f directly gives the bound state lifetime since the quasiparticle residence time in the subgap state is likely to be longer than the relevant switching timescale of the junction - τ_J for an overdamped junction, and $2\pi/\omega_p$, with ω_p is the plasma frequency, for an underdamped junction. In the opposite case of thermally activated poisoning, quasiparticles are first transfered elastically from the superconducting lead to the continuum in the island before relaxing to the subgap state within a time τ [115]. In this case, quasiparticles can escape from the island before they are detected if $\Gamma_{\text{out}}^{\text{neq}}$ is faster than the SCPT response time. Now, the time τ_{even} represents a lower bound on the parity lifetime of the subgap state, and the overall parity of island might fluctuate faster. Our previous estimate of $\tau_J \approx 1$ ns sets a lower bound on our poisoning detection bandwidth since the junction would switch even faster to the resistive state in the underdamped case which we observe at low temperature. Given that typical resonators in time-domain RF measurements have bandwidths of no more than a few 10's of MHz [72, 77, 105], switching current measurements are a promising alternative before Majorana poisoning times can be measured more directly via the coherence of MZM-based qubits.

Finally, with the design of future MZM-based qubits in mind it is worth comparing our results with those obtained with NbTiN islands [116]. Our observed gate-charge modulation of the switching current shows a robust $2e$-periodic signal for a wide range of gate settings which indicates that there are no low-energy subgap states inside the SCPTs at zero magnetic field. This is in stark contrast to the case of NbTiN islands, where subgap states result in a $1e$-periodic, bimodal switching current distribution. In that case, despite the large superconducting gap, the island parity is effectively randomized after each measurement when the island retraps after being flooded with quasiparticles.

4.4. Conclusions

We have investigated quasiparticle poisoning in hybrid InAs-Al SCPTs by measuring the gate charge modulation of the switching current as a function of temperature and magnetic field. In contrast to previous studies of NbTiN SCPTs, we observe a consistent 2e-periodic supercurrent at zero field despite having a similar gap in the island and leads. This highlights that at zero field there are no subgap states in the island, and places Al as the superconductor of choice for MZM qubit experiments despite its smaller gap and critical field relative to NbTiN. In addition, we have observed, for the first time, an oscillating pattern in the gate periodicity of the supercurrent due to the field-induced zero energy crossing of a bound state. This opens the door to using the switching current to identify MZMs in qubit devices with superconducting leads. This is a crucial proof-of-principle demonstration as the superconducting leads are not compatible with the zero-bias peak measurements typically taken as evidence of MZMs. We have performed lifetime measurements on this subgap state and observed an exponential decay of the lifetime in magnetic field due to a collapsing filtering effect of the leads. This exponential decay highlights the importance of proper engineering of the superconducting gap via local gating and intentional quasiparticle traps to minimize the presence of quasiparticles in the leads in future topological qubits.

4.5. Supplemental Material

Table 4.S1 – Device overview. Parameters characterizing the devices are the length of the island L, the thickness of the aluminum shell t_{Al}, and the backgate layout. Moreover, the geometric charging energy E_C^0 and superconducting gap Δ are listed. These parameters are extracted from Coulomb diamonds in the strongly blockaded regime (data shown in Figure 4.S1). In addition, the cooldown at which the device was measured is specified.

Device	L(μm)	Backgate layout	t_{Al} (nm)	E_C^0 (meV)	Δ(μeV)	Cooldown
1	0.5	Global	5	1.5	180	2
2	1	Global	5	0.85	160	2
3	2	Global	5	0.44	220	2
4	3	Global	5	0.35	180	2
5	3	Global	5	No data	No data	2
6	1.2	Local	8	0.5	160	1

4.5.1. Overdamped junction limit

In this section, we discuss the I-V characteristics and switching dynamics of overdamped junctions in the presence of quasiparticles. For larger temperatures where the I-V characteristics departs from $2e$ periodicity, the junction is typically in the overdamped regime which allows the following theory to capture the $2e$ to $1e$ crossover (see Fig. 4.3 in the main text).

Overdamped RCSJ model

We start with the standard RCSJ model of a junction with resistance R_J, capacitance C, and Josephson energy $E_J = \hbar I_c/2e$. The overdamped regime is reached once the damping rate $\tau_R^{-1} = (R_J C)^{-1}$ exceeds the plasma frequency $\omega_p = \sqrt{2eI_c/\hbar C}$. The equation of motion then takes the form of the Langevin equation

$$\dot{\phi} + \sin\phi = \mathcal{J} + \sqrt{2\Gamma_T}\eta(t)\,, \tag{4.S1}$$

where ϕ is the phase differences across the junction, $\mathcal{J} = I_{\text{bias}}/I_c$ is the current bias relative to the critical current, and time is measured relative to $\tau_J = (2eI_cR_J/\hbar)^{-1} = \tau_R^{-1}\omega_p^{-2}$. Fluctuations due to thermal noise $\Gamma_T = k_B T/E_J$ are assumed to be short-time correlated $\langle\eta(0)\eta(t)\rangle = \delta(t)$. Note that in these units, the renormalized voltage $v = V/I_cR_J$ is given by $v = \dot{\phi}$. The Langevin form can be mapped to a Fokker-Planck equation

$$\partial_t p = \partial_\phi\left([\partial_\phi u]p\right) + \Gamma_T\partial_\phi^2 p \tag{4.S2}$$

in terms of probability distribution $p = p(\phi, t)$ and potential $u(\phi, \mathcal{J}) = -\cos\phi - \mathcal{J}\phi$. Eq. (4.S2) is in the form of a continuity equation $\partial_t p + \partial_\phi j_p = 0$ which defines the

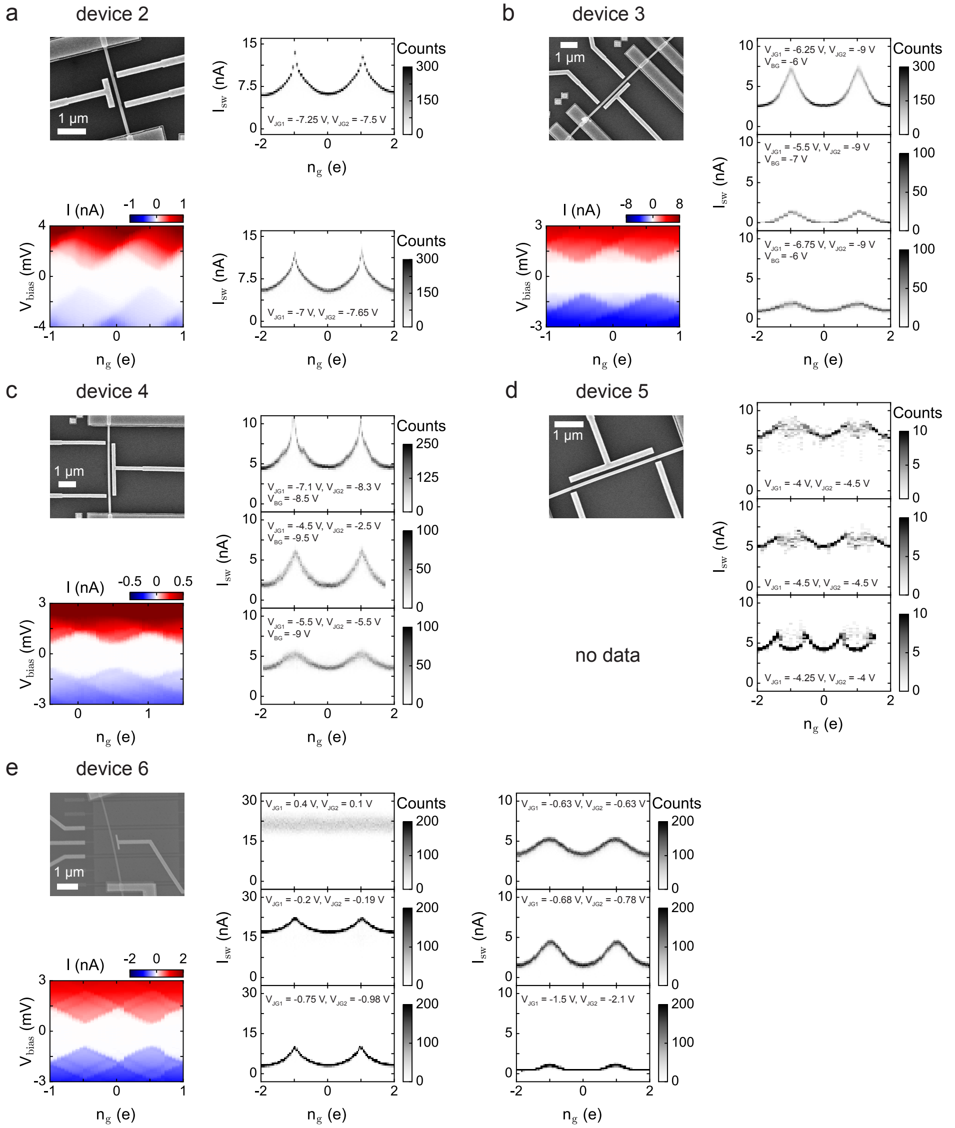

Figure 4.S1 – Scanning electron micrographs, Coulomb diamonds, and gate dependence of the $2e$-periodic signal for device 2-6 (**a** – **e**). The E_C^0 and Δ extracted from Coulomb blockade are summarized in Table 4.S1. Apart from device 5 which shows an even-odd pattern in the switching current modulation, all devices show a $2e$ modulation, illustrating that the $2e$ signal does not correspond to a fine-tuned gate setting. The gate settings corresponding to the measurements are specified in each subfigure. The gates are labeled using the same convention as in the main text. For device 2, 5, and 6 the backgate is fixed at V_{BG2} = -10 V, V_{BG5} = -8.5 V, and V_{BG6} = 0, respectively.

probability current

$$j_p = -[\partial_\phi u]p - \Gamma_T \partial_\phi p\,. \tag{4.S3}$$

The I-V characteristics can be obtained from considering the stationary case $\partial_t p = 0$ of constant current $\partial_\phi j_p = 0$. When the probability distribution is normalized with respect to the interval $[0, 2\pi]$, using periodic boundary conditions in ϕ, the current j_p is a measure for the rate at which the phase particle traverses the interval, and is therefore related to the voltage $v = 2\pi j_p$. Solving Eq. (4.S3) yields the I-V characteristics

$$v = 2\pi\Gamma_T \left(e^{\frac{2\pi\mathcal{J}}{\Gamma_T}} - 1\right)\left\{\int_0^{2\pi} d\phi \left[\int_0^{\phi} d\phi' + e^{\frac{2\pi\mathcal{J}}{\Gamma_T}} \int_\phi^{2\pi} d\phi'\right] e^{\frac{u(\phi',\mathcal{J})-u(\phi,\mathcal{J})}{\Gamma_T}}\right\}^{-1}\,. \tag{4.S4}$$

Quasiparticle dynamics in the overdamped RCSJ model

The overdamped RCSJ model can be readily extended to include quasiparticle dynamics by keeping track of the even $\alpha = 0$ and odd $\alpha = 1$ state of the island,

$$\partial_t \begin{pmatrix} p_0 \\ p_1 \end{pmatrix} + \partial_\phi \begin{pmatrix} j_0 \\ j_1 \end{pmatrix} = \begin{pmatrix} -\gamma_{\mathrm{in}} p_0 + \gamma_{\mathrm{out}} p_1 \\ +\gamma_{\mathrm{in}} p_0 - \gamma_{\mathrm{out}} p_1 \end{pmatrix}, \tag{4.S5}$$

where $j_\alpha = -[\partial_\phi u_\alpha]p - \Gamma_T \partial_\phi p_\alpha$ in terms of the parity dependent potential $u_\alpha(\phi, \mathcal{J}) = -a_\alpha \cos\phi - \mathcal{J}\phi$ with $a_0 = 1$ and $a_1 = E_{J1}/E_{J0}$. Here $\gamma_{\mathrm{in/out}} = \Gamma_{\mathrm{in/out}}\tau_J$ are dimensionless rates of switching the system from even to odd or vice versa. To derive the I-V characteristics, we again look at the steady state $\partial_t p_0 = \partial_t p_1 = 0$. We then observe that $\partial_\phi(j_0 + j_1) = 0$ and, similar to the single state case, the constant is fixed by the voltage $j_0 + j_1 = v/2\pi$. The normalization condition of the probabilities is now in terms of $\int d\phi(p_0 + p_1) = \bar{p}_0 + \bar{p}_1 = 1$. We now consider the two limiting cases of slow and fast poisoning.

Slow poisoning limit In the slow poisoning limit corresponding to $\gamma_{\mathrm{in}}, \gamma_{\mathrm{out}} \ll 1$ the right hand side of Eq. (4.S5) can be neglected which, in the steady state, sets both j_0 and j_1 independently to a constant and therefore recovers the standard RCSJ model. The result from section (4.5.1) can essentially be copied with voltages v_α defined by Eq. (4.S4) using the potential u_α of the corresponding parity state. To calculate the total voltage drop one needs to take into account that the normalization of the probabilities $\int_0^{2\pi} d\phi p_{0/1} = \bar{p}_{0/1} = \gamma_{\mathrm{out/in}}/(\gamma_{\mathrm{out}} + \gamma_{\mathrm{in}})$ enters Eq. (4.S4), so that the voltages v_α are correctly weighted. This yields

$$v = v_0 \bar{p}_0 + v_1 \bar{p}_1\,. \tag{4.S6}$$

We conclude that in the slow poisoning case the I-V characteristic is the weighted sum of the I-V characteristics of each parity where the weight is given by the average occupation. For significantly different even and odd switching currents we would therefore expect a double-kink in the I-V characteristics which is most clearly visible in the derivative $\mathrm{d}V/\mathrm{d}I$ which subsequently turns into a double-peak (see Fig. 4.S2).

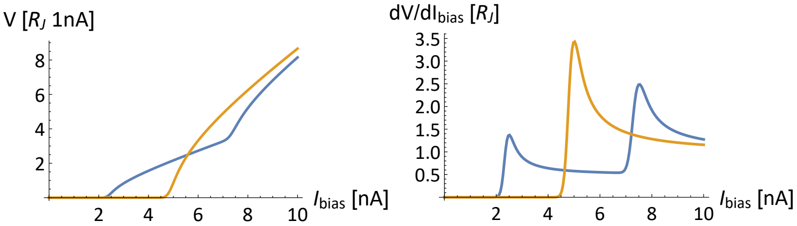

Figure 4.S2 – Analytic solution of the slow and fast poisoning limit. Voltage drop V in terms of the bias current I_{bias} (left) and dV/dI_{bias} (right). The slow poisoning case (blue) is showing a double-kink behavior while fast poisoning (yellow) leads to a single-kink at the averaged switching current. Parameters are $I_c^{(0)} = 2.5\text{nA}$, $I_c^{(1)} = 7.5\text{nA}$, and $\Gamma_T = 0.05$.

Fast poisoning limit In the fast poisoning limit corresponding to $\gamma_{\text{in}}, \gamma_{\text{out}} \gg 1$, the probabilities $p_\alpha(\phi)$ have to cancel the leading order of the right hand side of Eq. (4.S5) [up to terms $\mathcal{O}(1)$]. This allows to separate the fast quasiparticle dynamics, that lock the ratio of $p_0(\phi)/p_1(\phi)$ to $\bar{p}_0/\bar{p}_1$ for each ϕ, from the ϕ-dependence of the probability distribution, i.e. use the ansatz $p_\alpha(\phi) = \bar{p}_\alpha p_+(\phi)$ with $p_+(\phi) = p_0(\phi) + p_1(\phi)$. We can then solve for $p_+(\phi)$ by looking at the sum of both components of Eq. (4.S5)

$$\begin{aligned}\frac{v}{2\pi} = j_1 + j_2 &= -[\partial_\phi u_0]p_0 - [\partial_\phi u_1]p_1 - \Gamma_T \partial_\phi (p_0 + p_1) \\ &= -[\partial_\phi \left(\bar{p}_0 u_0 + \bar{p}_1 u_1\right)]p_+ - \Gamma_T \partial_\phi p_+ ,\end{aligned}$$

which yields the same type of equation to solve as for the standard RCSJ model with an effective potential $u_{\text{eff}} = \bar{p}_0 u_0 + \bar{p}_1 u_1$. The solution corresponds to a single kink that signals the onset of the resistive state that lies in between the double step kink solution of the slow poisoning case, see Fig. 4.S2.

General case In the general case the differential equation (4.S5) can be solved numerically. Figure 4.S3 shows a gray scale plot of the dV/dI-I characteristics for fast, intermediate, and slow poisoning with different $\Gamma_{\text{in}}/\Gamma_{\text{out}}$. Comparing the different poisoning scenarios with the experimental data of Fig. 4.3 clearly shows that at high temperatures, where the $\Gamma_{\text{in}}/\Gamma_{\text{out}}$ ratio is sizable, slow and intermediate poisoning is incompatible with the experimental data while fast poisoning yields an excellent agreement. Note that at the level of Eq. (4.S5) the critical currents $I_c^{(\alpha)}(n_g)$ are input parameters. For simplicity, we used a parabolic dependence with a minimum and maximum of 2.5 nA and 7.5 nA to resemble the behavior of Fig. 4.2b in the main text.

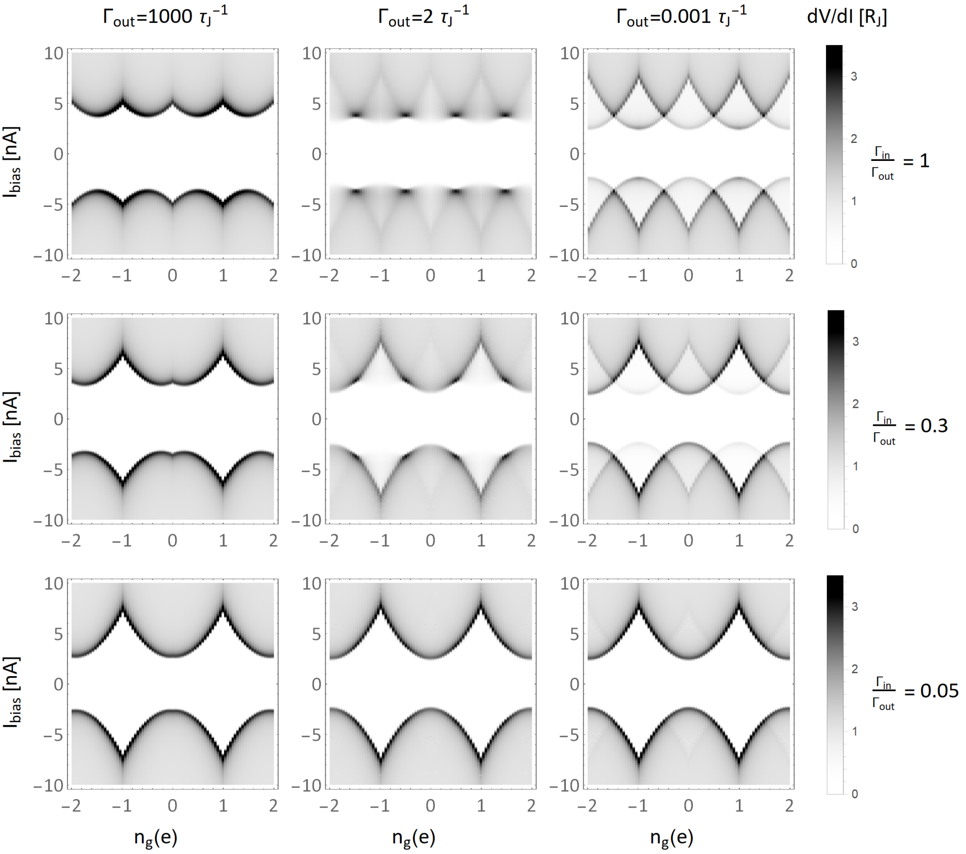

Figure 4.S3 – Numerical solution of the dV/dI characteristics in different parameter regimes. The columns from left to right correspond to fast, intermediate, and slow poisoning, respectively. The rows correspond to different ratios of $\Gamma_{\text{in}}/\Gamma_{\text{out}}$ and are therefore a measure of the temperature.

4.5.2. Temperature Dependence

In this section, we discuss the model used to fit the switching current histograms in Fig. 4.3 of the main text for varying temperature. In our model, we assume that the quasiparticle poisoning and unpoisoning rate is fast compared to the characteristic switching time of the junction $\Gamma_{\text{in}}, \Gamma_{\text{out}} \gg 1/\tau_J$. Under this assumption, which is justified above in section 4.5.1, the critical current of the SCPT is given by the weighted average of the critical currents in the even and odd states with the weighting coefficients given by the free energy difference between the parity states of the SCPT. In the opposite regime when the switching rate of the junction is much larger than the poisoning or unpoisoning rate $\Gamma_{\text{in}} \ll 1/\tau_J$ or $\Gamma_{\text{out}} \ll 1/\tau_J$, we expect a bimodal switching current distribution. This is not observed in the temperature dependence data. It is important to note that the fast poisoning-unpoisoning assumption may be broken at small temperatures, where the probability of odd state occupation is very small. Even though we do not see bimodal distribution of the switching current at low temperatures, this may be due to weak spectral density of the peak corresponding to the odd occupations.

To calculate the sought-after temperature dependence, we need to compute the critical currents in the two parity states as functions of the gate charge n_g, as well as the free energy difference between the two states. To do so, we use the Hamiltonian $H = H_J + H_C + H_{\text{BCS}}$ described in section 2.3.2. For the fitting procedure, we fix moderately asymmetric junction with $E_{J1}/E_{J2} = 2$. Furthermore, we note that the chaging energy is possibly renormalized due to (virtual) tunneling of quasiparticles. We can find the even ground state energy of the SCPT as a function of the phase difference between the superconducting leads ϕ and gate charge n_g, $E^{even}(\phi, n_g)$, by diagonalizing the Hamiltonian. The odd ground state energy is found by shifting $E^{even}(\phi, n_g)$ by $n_g = 1$ and adding the superconducting gap; $E^{odd}(\phi, n_g) = E^{even}(\phi, n_g + 1) + \Delta$. The zero-temperature supercurrent is given by the derivative of the ground state energy as a function of phase difference

$$I_c^{even}(\phi, n_g) = \frac{e}{\hbar}\frac{\partial}{\partial\phi}E^{even}(\phi, n_g). \tag{4.S7}$$

The finite-temperature supercurrent is given by the weighted sum of the even and odd ones with the assumption of the fast (un)poisoning, where the weighting factors p_{odd} and $p_{even} = 1 - p_{even}$ are calculated as follows

$$p_{odd}(T, \phi, n_g) = \frac{Z_{odd}}{Z_{even} + Z_{odd}} = \frac{1}{1 + \exp(\Delta F(T, \phi, n_g)/k_B T)}, \tag{4.S8}$$

where $Z_{odd,even}$ are the partition functions in the state with and without a quasiparticle on the island, respectively, ΔF is the free energy difference between the parity states, k_B is the Boltzmann constant, and T is the temperature.

The free energy difference between the two parity states can be computed as follows

$$\Delta F(T,\phi,n_g) = \delta E(\phi,n_g) - k_B T \ln\tanh z_i(T,\delta_i), \tag{4.S9}$$

$$z_i(T,\delta_i) = \frac{2\pi\sqrt{k_B T\Delta}}{\delta_i}\exp(-\Delta/k_B T). \tag{4.S10}$$

Here $\delta E(\phi,n_g) = E^{\text{even}}(\phi,n_g+1) - E^{\text{even}}(\phi,n_g)$ is the difference in ground state energy between the odd and even parity sectors (not including Δ), z_i is the partition function difference between the quasiparticle being inside the island at energy Δ and in the lead at zero energy, and δ_i is the level spacing inside the island. In this expression we assume that the quasiparticle is tunneling from a gapless, large quasiparticle trap. This means the lead has negligible level spacing and negligible change of entropy due to the removal of one electron from the trap. We assume $\delta_i = 5$ mK. This gives the following expression which we use to fit the data

$$I_c(T,n_g) = \max_{\phi}\left[I_c^{even}(\phi,n_g)(1-p_{odd}(T,\phi,n_g)) + I_c^{even}(\phi,n_g+1)p_{odd}(T,\phi,n_g)\right]. \tag{4.S11}$$

Equation (4.S11) fits the data nicely, as shown in Fig. 4.3a of the main text. It is important to mention that the same fit assuming non-equilibrium quasiparticles in the lead instead of equilibrium quasiparticles in the trap does not fit the data, since even at lowest temperatures it would produce an even-odd or a purely 1e periodicity. We thus conclude that the dominating poisoning effect is via direct tunneling of the quasiparticles from the normal lead.

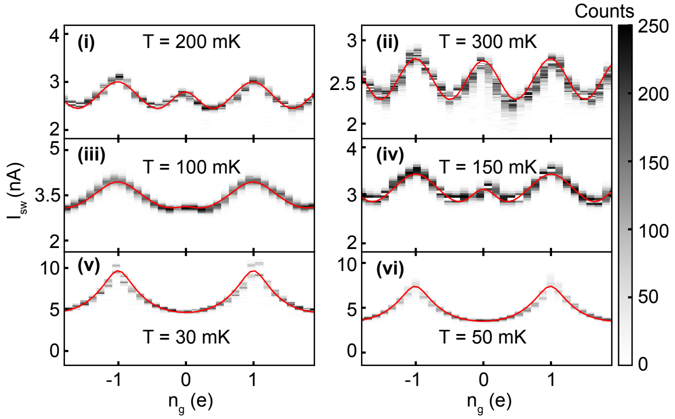

Figure 4.S4 – Switching current modulation as a function of temperature for device 2 at R_N = 10.5 kΩ. The experimental histograms shown in grayscale are overlaid by the theoretical fit to the average switching current $\langle I_{\text{sw}}\rangle$ (red curves). Individual fits are for different values of Δ, E_J, and E_C. The averaged values for these parameters are $\Delta \approx 245$ µeV, $E_C \approx 192$ µeV, and $E_J \approx 111$ µeV.

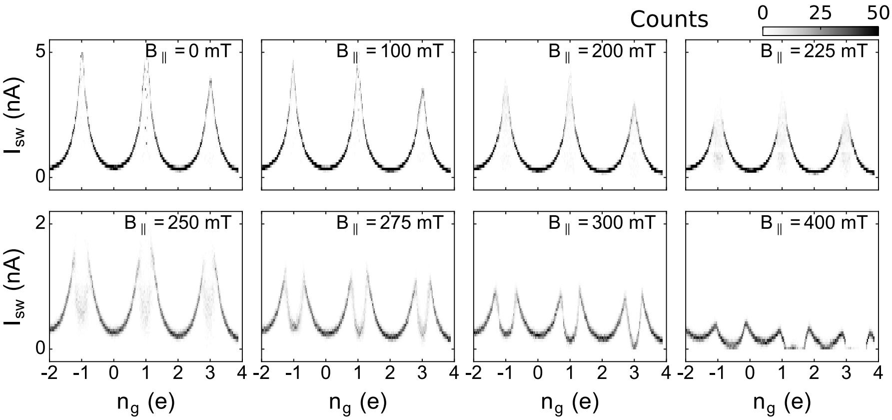

Figure 4.S5 – Representative switching current histograms as a function of parallel magnetic field for device 1 at $V_{BG} = -7.55$ V, and $V_{JG1} = V_{JG2} = -1.5$ V. The S$_{\text{even}}$ and S$_{\text{odd}}$ spacings reported in Figure 4.4e are extracted from the average S$_{\text{even}}$ and S$_{\text{odd}}$ of these histograms. Note that the histogram at $B_{\|} = 400$ mT is distorted around $n_g = 1.5$ and $n_g = 3.5$ due to false triggers.

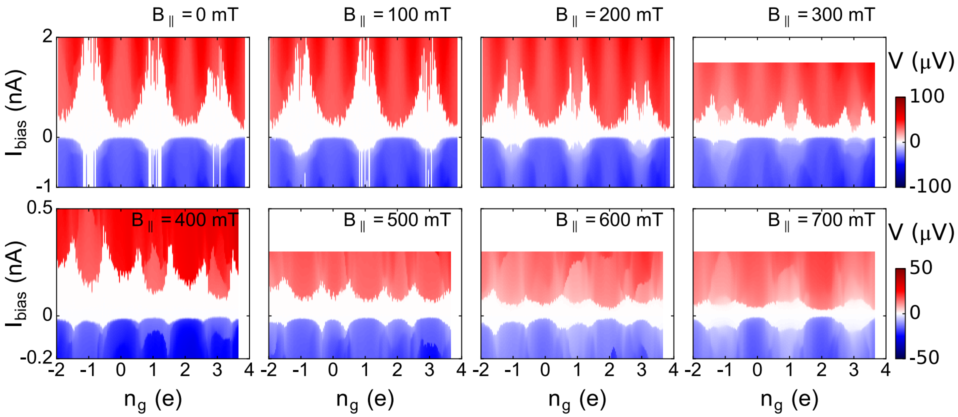

Figure 4.S6 – Representative I-V characteristics as a function of parallel magnetic field for device 1 at $V_{BG} = -7.55$ V, and $V_{JG1} = V_{JG2} = -1.5$ V. The S$_{\text{even}}$ and S$_{\text{odd}}$ spacings reported in Figure 4.4e are extracted from the average S$_{\text{even}}$ and S$_{\text{odd}}$ of these I-V characteristics.

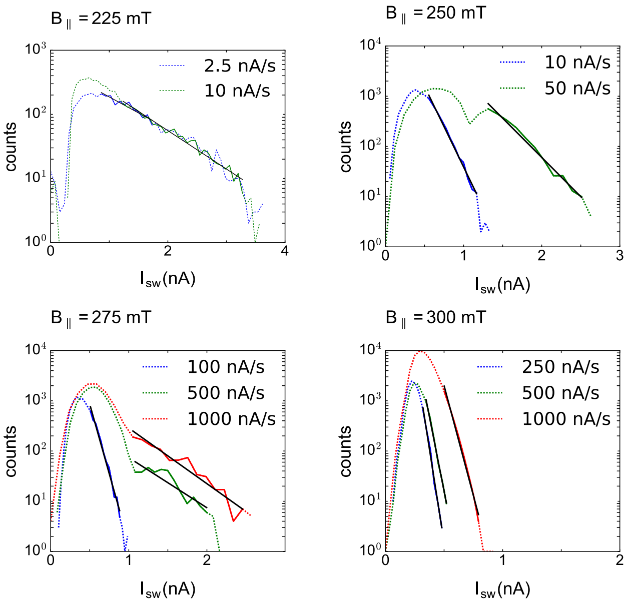

Figure 4.S7 – Slow switching current histograms at $n_g = 1$ at representative values of the magnetic field taken on device 1 at $V_{BG} = -7.55$ V, $V_{JG1} = V_{JG2} = -1.5$ V. The even state lifetime τ_{even}, presented in Figure 4.4f of the main text, was obtained from the exponential tail of the histograms, using the following model: $N = N_0 \exp\left(-\frac{I-I_0}{dI/dt\tau_{\text{even}}}\right)$, where N_0 is the number of counts at I_0 and $\mathrm{d}I/\mathrm{d}t$ is the current ramp rate. The extracted lifetimes are tabulated in Table 4.S2.

Table 4.S2 – Overview of the even state lifetimes at $n_g = 1$ as a function of the parallel magnetic field $B_\parallel$ taken on device 1. This data is presented in Fig. 4.4f of the main text. In addition, the current ramp rate $\mathrm{d}I/\mathrm{d}t$ and the sample size N used to construct the switching current histogram are shown.

$B_\parallel$ (mT)	dI/dt (nA/s)	τ_{even} (ms)	N
225	2.5	105	3500
	10	80	5000
237	2.5	50	5000
	10	30	10000
250	10	4.8	10000
	50	5.6	10000
262	50	1.6	10000
	100	2.4	25000
275	100	0.78	10000
	500	0.87	10000
	1000	0.39	10000
287	500	0.1	10000
	1000	0.26	50000
	2000	0.22	50000
300	250	0.11	10000
	500	0.073	10000
	1000	0.05	50000

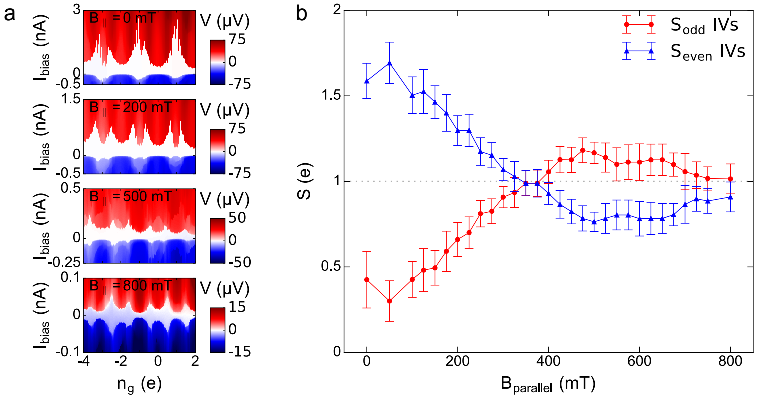

Figure 4.S8 – Parallel magnetic field dependence of the even and odd spacing in device 1 at $V_{BG} = -7.65$ V and $V_{JG1} = V_{JG2} = -1.5$ V. Although it is very close to the used gate setting for the data presented in Figure 4.4 of the main text, we believe this corresponds to a different charge configuration in the SCPT because the of hysteresis in the gate response. **a** I-V characteristics used for the construction of **b** for representative values of the parallel magnetic field. **b** S_{even} and S_{odd} as a function of the parallel magnetic field. S_{even} (S_{odd}) is obtained by averaging over 2 (3) succesive spacings respectively. At this gate setting, the spacings cross, similar to the data presented in Figure 4.4e of the main text. However, the shape of the oscillation pattern is different from Figure 4.4e.

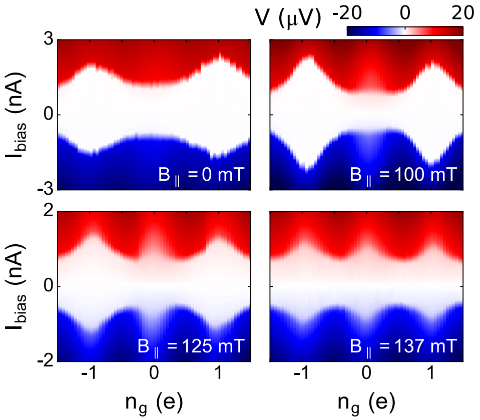

Figure 4.S9 – Parallel magnetic field dependence of the I-V characteristics of device 4. Instead of an even-odd pattern that develops as a function of field, as was observed for device 1, the I-V characteristics develop a peak in the switching current at odd gate charge similar to the behavior that was observed as a function of temperature (Fig. 4.3). This indicates that the SCPT is in the fast (un)poisoning limit possibly caused by field-induced softening of the gap.

5

Rapid detection of coherent tunneling in an InAs nanowire quantum dot through dispersive gate sensing

Dispersive sensing is a powerful technique that enables scalable and high-fidelity readout of solid-state quantum bits. In particular, gate-based dispersive sensing has been proposed as the readout mechanism for future topological qubits, which can be measured by single electrons tunneling through zero-energy modes. The development of such a readout requires resolving the coherent charge tunneling amplitude from a quantum dot in a Majorana zero mode host system faithfully on short time scales. Here, we demonstrate rapid single-shot detection of a coherent single-electron tunneling amplitude between InAs nanowire quantum dots. We have realized a sensitive dispersive detection circuit by connecting a sub-GHz, lumped-element microwave resonator to a high-lever arm gate on one of dots. The resulting large dot-resonator coupling leads to an observed dispersive shift that is of the order of the resonator linewidth at charge degeneracy. This shift enables us to differentiate between Coulomb blockade and resonance – corresponding to the scenarios expected for qubit state readout – with a signal-to-noise ratio exceeding 2 for an integration time of 1 μs. Our result paves the way for single shot measurements of fermion parity on microsecond timescales in topological qubits.

This chapter is based on D. de Jong, J. van Veen, L. Binci, A. Singh, P. Krogstrup, L. P. Kouwenhoven, W. Pfaff, and J. D. Watson, Rapid detection of coherent tunneling in an InAs nanowire quantum dot through dispersive gate sensing, *Physical Review Applied* **11**, 044061 (2019).

5.1. Introduction

Dispersive sensing is a promising measurement technique that enables high-fidelity readout of solid-state quantum bits, such as superconducting [87, 126] or spin qubits [127]. Recently, dispersive readout has also been proposed for future topological qubits based on Majorana zero modes (MZMs) [17, 18]. In particular, gate-based dispersive readout can be used to measure an electron tunneling rate in the system which in turn reflects the state of the qubit [128]. As a result of this difference in tunnel coupling, different qubit states can impart a different dispersive shift on a resonator coupled to the gate electrode. This frequency shift can be probed on very fast time scales, using state-of-the-art radio frequency (RF) techniques, and in a quantum non-demolition manner with minimal perturbation [87, 129].

High-fidelity, quantum non-demolition measurements require fast readout with high signal-to-noise ratio (SNR). This is particularly crucial for measurement-based quantum computation, such as proposed for MZM-based architectures [17, 18, 130]. So far, however, the frequency shift of dispersive gate sensors has been fairly small, on the order of a degree [127, 128, 131–133]; correspondingly, the required readout times to resolve a difference in tunnel coupling has been in the range of milliseconds [134–136]. It is thus of great interest to find avenues toward increasing the attainable SNR, and achieve readout on the sub-microsecond scale, as available for other solid-state qubit platforms [137].

In this chapter, we show rapid dispersive sensing in an InAs nanowire double quantum dot system. InAs nanowires have been studied in the context of spin qubits [88, 138], but have also recently gained significant attention as host system for MZMs that could enable the realization of topological qubits [41, 139]. We demonstrate a sensitive gate sensor based on a large-lever arm top-gate that is connected to an off-chip, lumped-element resonant circuit probed with reflectometry [91]. In particular, we show a dispersive shift close to 1 MHz which is on the order of the linewidth of the resonator; this results in a detected phase shift that approaches the maximally possible value of π. We study in detail the magnitude of the dispersive shift both as a function of tunnel coupling and readout power; we find, in agreement with theory, that the attainable shift is ultimately set by the magnitude of the tunneling rate and the resonator frequency. The large shift allows us to resolve a difference in tunneling rate with a SNR of up to 2 within 1 µs.

5.2. Experimental approach and setup

The coherent tunneling amplitude t_C, between two single-particle levels in weakly coupled quantum dots can be detected through an arising change in differential capacitance [140, 141]. The coupling affects the expectation value of charge on either island. The dependence of induced charge on gate voltage, i.e. the differential capacitance $C = \partial Q/\partial V_g$, depends on the coupling. This effect can be described within the framework of circuit quantum electrodynamics (cQED) [87] or as a “quantum capacitance” [142] and measured by monitoring the change in differential capacitance through an external tank circuit. Our aim is to determine how fast the tunneling amplitude can be detected; this maps to the projected readout performance

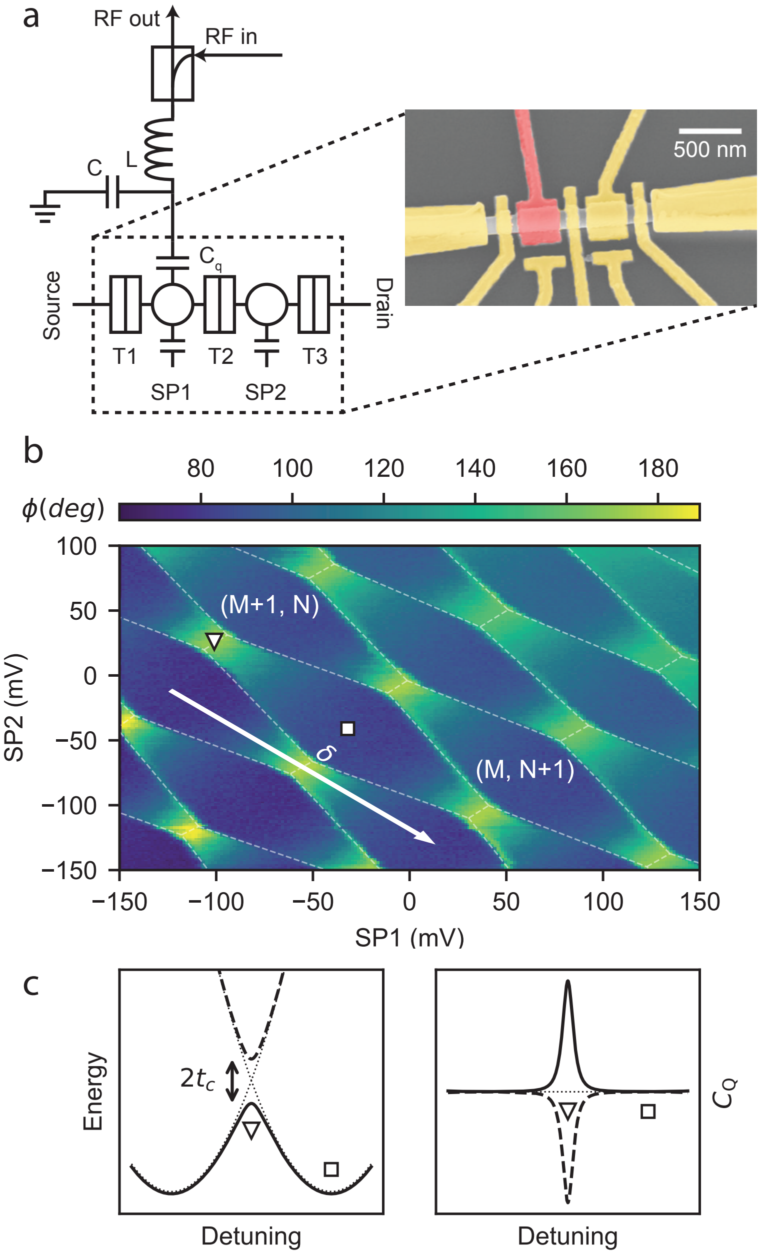

Figure 5.1 – Dispersive sensing on an InAs nanowire double quantum dot. a Schematic of the of experiment measurement setup. One of the quantum dots is capacitively coupled to a resonant circuit that is probed in reflectometry. Inset: False-colored electron micrograph of a nominally identical device. The sensing top gate is colored red. **b** Charge stability diagram measured with the gate resonator. The dashed lines are guides to the eye. The triangle marker denotes charge degeneracy while the square marker denotes Coulomb blockade. The arrow denotes the detuning from charge degeneracy, δ. **c** Sketch of the energy levels and resulting quantum capacitance versus detuning. Solid lines: ground state; dashed lines: first excited state; dotted line: case of no interdot tunneling.

for MZM qubits [17, 18] where the magnitude of the tunnel coupling is the qubit readout signal.

Our experiment approach is schematically depicted in Fig. 1a. We form two quantum dots in an InAs nanowire where the interdot coupling can be set through a gate voltage. We designate one of the dots as the "sensor" whereas the other dot is merely used as an auxiliary single level system, in lieu of MZMs. To achieve a large signal from the interdot coupling, we connect a gate with a large lever arm to a resonant circuit. The goal of the experiment is then to resolve a change in resonance frequency,

$$\delta\omega = \sqrt{LC}^{-1} - \sqrt{L(C + C_\mathrm{q})}^{-1}, \tag{5.1}$$

that arises from the tunneling-dependent quantum capacitance C_q (Fig. 1c).

To realize this experiment we have fabricated a double quantum dot in an InAs nanowire with a diameter of approximately 140 nm. The nanowire was deterministically deposited using a micromanipulator on an intrinsic silicon substrate with a 20 nm $\mathrm{SiN_x}$ dielectric layer deposited with LPCVD after removing the native $\mathrm{SiO_2}$. Contacts to the nanowire are made using argon milling followed by evaporating a 10 nm Ti sticking layer and a 150 nm Au layer. A 10 nm $\mathrm{AlO_x}$ dielectric layer deposited using atomic layer deposition (ALD) seperates the nanowire from the top gates. By using a thin dielectric layer, we ensure a large lever arm from the top gates to the underlying quantum dots. The top gates consist of a 10 nm Ti layer and a 150 nm Au layer. A false color SEM of a similar device is shown in Fig. 1a.

Using top gates T1, T2, and T3, a double dot is defined in the nanowire by pinching off the electron coupling to the leads and between the two dots. The top gate of the sensing dot is wire-bonded to a lumped-element resonator that was fabricated on a separate chip [91]. The sample is cooled down in a dilution refrigerator with a base temperature of 20 mK. The resonator response is then probed using standard RF heterodyne techniques (Fig. 1a).

5.3. Results

5.3.1. Observation of quantum capacitance and dispersive shift

We begin by characterizing the change in resonator response resulting from coherent tunneling between the two quantum dots. To this end, we first tune the device to a regime where the dot charge states strongly hybridize on resonance. We then record the phase response of a reflected probe field as a function of the two plunger gates, SP1 and SP2. (Fig. 1b). The resulting charge stability diagram shows a prominent phase shift at charge degeneracy, hinting at a large dispersive shift of the resonator frequency. We attribute the substantial magnitude of the observed phase shift in this regime to the large lever arm of the sensing gate [87, 142]. From independent Coulomb blockade measurements, we estimate the lever arm to be $\alpha = C_\mathrm{g}/C_\Sigma \approx 0.75$, where C_g is the capacitance of the gate to the sensing dot, and C_Σ is the total capacitance seen by the dot.

The relation between the dispersive shift and the magnitude of the interdot coupling lies at the heart of the C_q detection scheme; we therefore focus next on model-

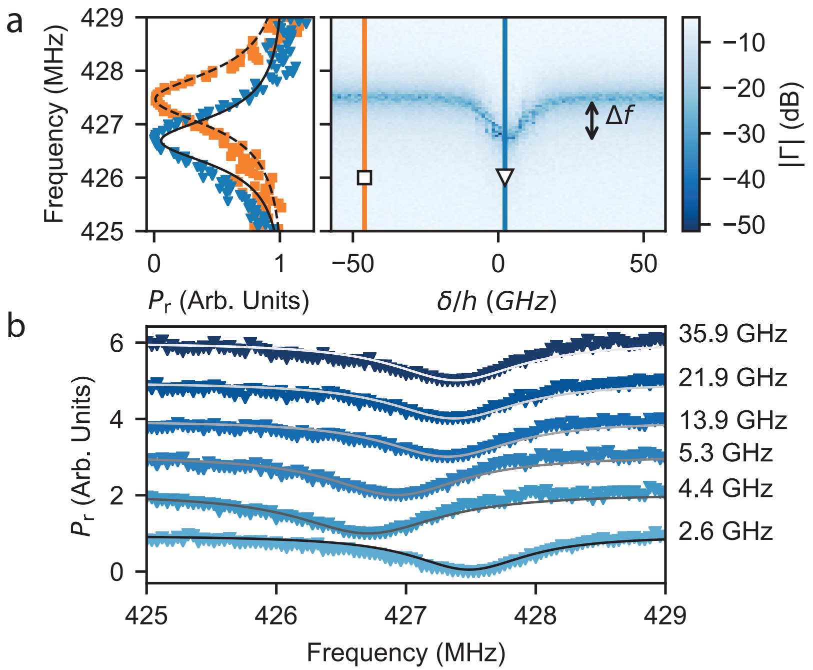

Figure 5.2 – **Charge-resonator coupling. a** Right panel: Resonator reflection spectrum measured from the difference between injected (P_{RF}) and reflected RF power (P_r) corrected for estimated attenuation and gain in the setup, as a function of detuning δ. T2-gate voltage was −768 mV for this data. Left panel: Line cuts in blockade (orange; square) and at degeneracy (blue; triangle) together with fits (black) to Eq. (5.2). **b** Resonator spectroscopy at charge degeneracy for different tunneling rates together with the fit to Eq. (5.2). Traces are offset for clarity. Tunnel rates t_C/h extracted from the fit are indicated on the right.

ing this relation from our data following earlier work performed on semiconductor dots in cQED environments [88, 132]. Near charge degeneracy the eigenstates of the double dot are superpositions of a charge delocalized between the two dots, with energy splitting $\Omega = \sqrt{4t_C^2 + \delta^2}$, where t_C is the tunnel coupling[1], and δ is the detuning of the two dots (Fig. 1c) [143]. To determine the tunnel coupling, we measure the resonator response as a function of δ and the detuning of the drive from the resonance frequency (Fig. 2a). The reflected probe signal can be developed in a cQED approach from the input-output relations [87, 88],

$$\frac{a_{\text{out}}}{a_{\text{in}}} = 1 + \frac{\mathrm{i}\kappa_{\text{ext}}}{-\mathrm{i}\kappa/2 + \Delta\omega + g\chi}. \tag{5.2}$$

Hereby, $a_{\text{in,out}}$ are the complex input and output signals; $\kappa = \kappa_{\text{int}} + \kappa_{\text{ext}}$ is the total resonator damping rate, composed of internal losses κ_{int} and external coupling

---

[1] In this chapter, the full splitting at zero detuning is $2t_C$ rather than t_C as in Eq. (2.14).

κ_{ext}; $\Delta\omega$ is the detuning of the drive from resonance; $g = g_0(2t_C/\Omega)$ is the effective coupling strength with g_0 being the Jaynes-Cummings coupling; and χ is the susceptibility of the double quantum dot that depends on the dephasing rate γ and the detuning between the charge dipole and the resonator,

$$\chi = g/(\omega_0 - \Omega + \mathrm{i}\gamma/2). \tag{5.3}$$

Figure 2a shows the evolution of the dispersive shift as we tune the double dot between Coulomb blockade regime and charge degeneracy, for one particular tunnel gate setting. Fitting this data yields the tunnel coupling, as well as the relevant parameters characterizing circuit and resonator-dot coupling. In particular, we find $Q = \omega_0/\kappa \approx 350$, and $g_0/2\pi \approx 60$ MHz, consistent with the large lever arm. This procedure allows us now to correlate the tunnel coupling and the dispersive shift with the gate voltage on electrode T2 (Fig. 2b).

5.3.2. Quantitative model of the dispersive shift

Having established the means to analyze the resonator response, we now investigate the change in resonator frequency as a function of double dot properties. Figure 3a shows the magnitude of the dispersive shift at charge degeneracy as a function of tunnel coupling. This shift can be predicted using the quantum capacitance picture; from determining the expectation value of charge on the sensing dot one expects [142, 144]

$$C_{\text{q}} = \frac{\alpha^2 e^2}{4t_C}, \tag{5.4}$$

where e is the electron charge; this relation straight-forwardly yields the frequency shift through Eq. (5.1). We find that this prediction agrees well with our data for tunnel couplings $t_C/h \gtrsim 4$ GHz. The effect of reduced frequency shift with increasing tunnel coupling is reflected also in the familiar geometry of charge stability diagrams (Fig. 3a, inset). For small tunnel couplings, we observe a reduction in the shift; this behavior is likely due to noise in the system, such as thermal fluctuations [133] or charge fluctuations on the gates (i.e. fluctuations in δ). This noise would effectively blur out the C_{q} peak as it narrows with decreasing t_C.

A natural question that arises is in which regimes this simple description holds. In particular, from the quantum capacitance picture one could naively expect that it is always possible to increase the power of the readout tone to increase the signal-to-noise ratio (SNR). However, this view ignores any internal dynamics of the quantum dot system that can impact the dispersive shift. Most importantly, increasing the AC voltage of the readout drive can induce transitions of the ground state to the excited state of the double dot, resulting in an incoherent mixture. Since the dispersive shift from the excited state is opposite to that of the ground state, excitation would thus lead to a reduction of the measured shift.

In Figure 3b, we show the evolution of the dispersive shift when increasing the readout drive amplitude; indeed, the shift disappears entirely at large drive amplitudes. We compare this data to a model in which we compute the excitation of the double dot by assuming that the readout drive acts as a detuned Rabi drive (with

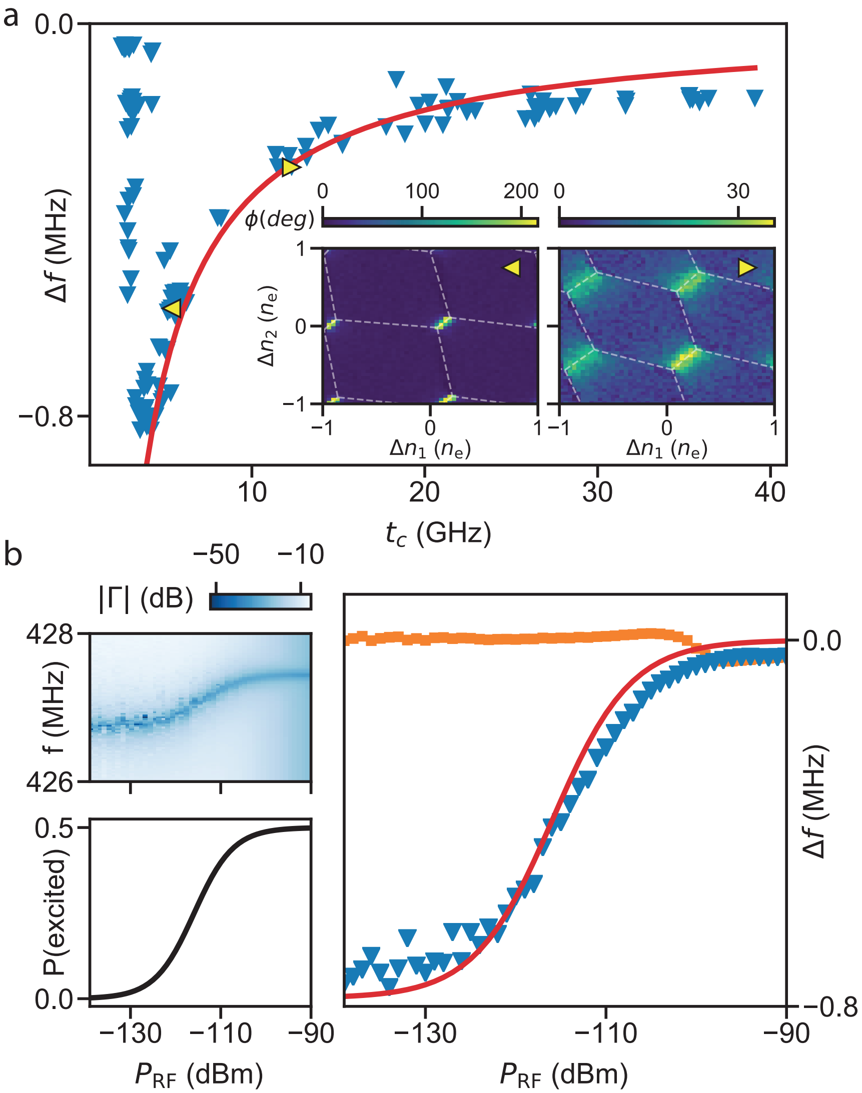

Figure 5.3 – Evolution and modeling of the dispersive shift. **a** Frequency shift as a function of tunneling rate, extracted from fitting spectroscopy data to Eq. (5.2). We estimate an accuracy of 5 % for extracting the tunnel coupling and of 40 kHz in the extraction of Δf. Solid line: independent theoretical prediction from Eq. (5.4). Inset: charge stability diagrams for tunneling rates corresponding to the yellow markers. **b** Resonator response as a function of frequency and power. Power is given at the sample level; this is attenuated by a total of ∼ 79 dB after the generator. Top left panel: resonator spectroscopy as function of RF power. Bottom left panel: calculated steady state population in the excited state. Right panel: Resonator shift in blockade (orange), and on degeneracy (blue). Red: prediction from the excited state population by assuming that the net shift is given by the population-weighted average between ground and excited state shifts.

detuning $\omega_0 - 2t_C/h$) and the double dot dephases quickly. We find that the double dot approaches a fully mixed state in the same range in which the disappearance of the shift occurs; the resulting predicted dispersive shift is in very good agreement with the data.

We can therefore conclude that the tunnel coupling has two competing influences on the observed resonator shift: For one, the shift gets larger for decreasing t_C following Eq. (5.4). On the other hand, in the present setup a decreased tunnel coupling results in reduced drive detuning; this in turn increases excited state population, reducing the shift again.

5.3.3. SNR for detecting a tunnel amplitude

In order to show the feasibility of dispersive gate sensing for qubit readout, we finally investigate the time-resolved resonator response. In particular, we aim to show that the difference in charge hybridization between Coulomb blockade and charge degeneracy can be obtained on fast time scales [17, 18]. To do so, we repeatedly measure the RF-signal in Coulomb blockade and on charge degeneracy by switching between the two points in the charge stability diagram. The signal is then binned in 1 µs intervals and for each interval, the in-phase and quadrature components of the signal are extracted and represented in a histogram (Fig. 4a). From Gaussian fits, we can then extract the SNR, which is given by the distance between the two distributions, Δ, divided by their full width, 2σ. These widths are set by the noise in the system, which is dominated by the thermal contribution of the cryogenic amplifier. From independent measurements, we estimate the equivalent noise temperature of the readout circuit to be around 4 K.

In Figure 4b, we show the attained SNR per 1 µs "shot" as a function of readout power and tunnel coupling. The SNR reaches its peak value of >2 for an RF power of $P_{\mathrm{RF}} \approx -109$ dBm and a tunnel coupling of ∼ 5 GHz. The probability of misidentifying the state of the system using thresholding is less than 2 % for these settings. Since the signal is largely set by the frequency shift, the dependence of the SNR on t_C closely follows the evolution of the dispersive shift shown in Fig. 3a. The power dependence results from the competition between double dot excitation and signal increase. The optimal power is reached at the point where the diminishing frequency shift starts dominating over the improvement gained from larger accuracy in the estimation of I and Q.

5.4. Conclusions

We have performed gate-based dispersive sensing on a double quantum dot in an InAs nanowire. The observed charge-tunneling induced dispersive shift on our resonator is comparable to the resonator linewidth, enabling fast detection of the presence of the tunnel amplitude with high SNR. Notably, this result was achieved with a low-Q, lumped-element resonator operating at a frequency of less than 1 GHz; these types of resonators hold great promise for scalable readout due to their reduced footprint compared to high-Q, CPW resonators that are more traditionally used in cQED [87]. Utilizing the large resonator shift, we have shown that states corresponding to different charge hybridizations can be distinguished in 1 µs measurements while retaining an SNR exceeding two in our experimental setup. We have further established that the factor that predominantly limits the SNR is the tunnel coupling. Its magnitude determines the dispersive shift, and its detuning from the resonator frequency places a limit on the readout power that can be used before adverse effects take over.

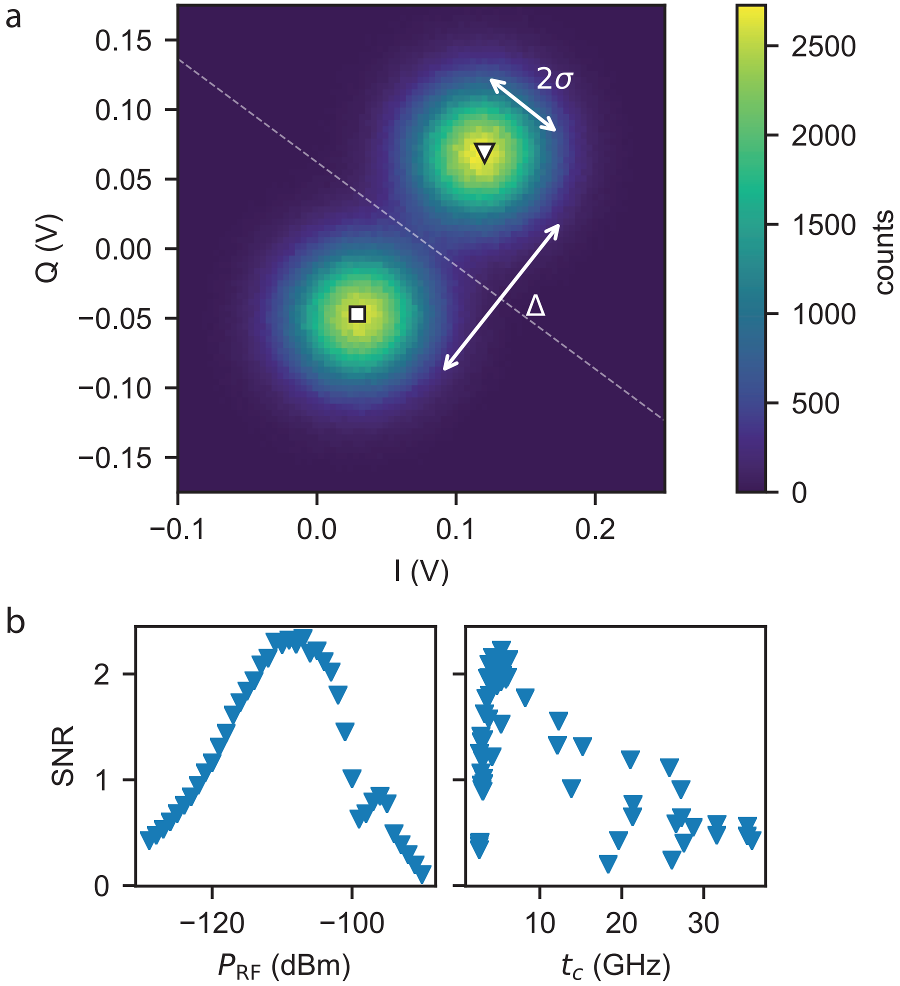

Figure 5.4 – **Readout SNR. a** Histogram of resonator reflection measurements in Coulomb blockade (square marker) and charge degeneracy (triangle marker). This data was taken with a tunnel coupling of 4.3 GHz and a readout power of $P_{\mathrm{RF}} = -105$ dBm. Each count corresponds to an integration time of 1 µs. The SNR is defined as $\Delta/2\sigma$. The dashed line is the threshold used for state identification. **b** Attained SNR as a function of readout power (left panel) and tunnel coupling (right panel). For the tunnel coupling dependence, readout power and frequency were optimized for every data point individually.

Our results show that high-fidelity measurements of semiconductor nanowire-based qubits could be performed using gate-sensing on the single-microsecond scale. This is particularly promising for MZM-based topological qubits that could be realized in nanowire networks [17, 18]. Since our work illustrates the dominating factor of only a few key device parameters — such as electron tunneling rate, gate lever arm, and resonator frequency — our results can provide important guidance for the design of qubit and measurement circuits. We further expect that existing technology could be used to lower the noise temperature of the cryogenic amplifier [145–148] or optimize the sensing circuits [149] in order to enhance the attainable SNR further, and reduce the required measurement time.

6

Revealing charge-tunneling processes between a quantum dot and a superconducting island through gate sensing

We report the detection and identification of charge-tunneling processes between a quantum dot and a superconducting island through radio-frequency gate sensing. We are able to resolve spin-dependent quasiparticle tunneling as well as two-particle tunneling involving Cooper-pairs. The sensor allows us to characterize the superconductor excitation spectrum, enabling us to access subgap states without transport. Our results provide crucial guidance for future dispersive parity measurements of Majorana modes, which can be realized by detecting the parity-dependent tunneling between dots and islands.

This chapter is based on J. van Veen, D. de Jong, L. Han, C. Prosko, P. Krogstrup, J. D. Watson L. P. Kouwenhoven, and W. Pfaff, Revealing charge-tunneling processes between a quantum dot and a superconducting island through gate sensing, submitted (2019).

6.1. Introduction

Quantum dots coupled to superconductors can give rise to novel physical phenomena such as π and ϕ_0-junctions [48, 150, 151], Cooper-pair splitting [152, 153], and Yu-Shiba-Rusinov (YSR) states [154, 155]. These phenomena arise because the single-electron states of the dot hybridize with the more complicated many-particle states of the superconductor. Recently, such hybrid systems have gained interest in the context of Majorana zero modes (MZMs) where the quantum dot (QD) can, for example, be used as a spectrometer [35]. Moreover, projective parity measurements can be achieved by coupling a QD to a pair of MZMs, which are located on a superconducting island (SC) [41, 52], enabling topologically protected quantum computation. These projective measurements rely on the parity-dependent hybridization between a single dot level and the MZMs [17, 18]. Therefore, unambiguous detection of coherent tunneling between a QD and the superconducting island is needed to implement this readout.

Dispersive gate sensing provides direct access to the charge hybridization between weakly coupled dots or islands. More precisely, coherent tunneling within these structures can impart a frequency shift on a resonant circuit that can be observed on short time scales with high accuracy. In this way, experiments have revealed coherent charge hybridization between superconductors [142, 156, 157] and in semiconductor double quantum dots [88, 128, 132]. Moreover, capacitive RF sensing has been used to study charging of QDs connected to normal- and superconducting reservoirs [158, 159]. However, while dispersive readout presents an excellent opportunity to study charge-tunneling between QDs and superconducting islands, it has not been employed yet in such hybrid systems.

In this chapter, we report detection and identification of charge-tunneling processes between a QD and a superconducting island through RF sensing via an LC resonator connected to the gate of the QD. From observations of the resonator response, supported by numerical simulations of the system, we find that the nature of the tunneling depends crucially on the ordering of the relevant energy scales of the SC. When the smallest scale is the energy of the lowest single-particle state, the QD and SC can exchange quasiparticles, giving rise to a characteristic “even-odd” effect. Conversely, when the charging energy of the SC is lowest, we detect signatures of Cooper-pairs tunneling out of the SC. Depending on the tunneling amplitude, this results in either $1e$-charging of the QD, with the other electron leaving into a reservoir, or $2e$-charging of the QD via coherent Cooper-pair tunneling. We can re-enable the tunneling to the single-particle states by operating the device in a floating regime where the total number of charges in the two systems is conserved.

A schematic of our experiment is shown in Fig. 1a. Two charge islands are formed in an InAs nanowire with an epitaxially grown Al-shell. A superconducting island is defined by removing the Al outside a 1.2 µm segment with wet-etching. Tunneling barriers are implemented with gates, insulated from the wire by 10 nm AlO_x. They are used to define the QD and SC; and to control the various tunneling rates. Large-lever arm top gates (“plungers”) on both QD and SC can be used to tune the chemical potentials. The dot plunger is connected to an off-chip, superconducting resonator [91]. We use its response near the resonance frequency to probe the charge tunneling on and off the dot. We have fabricated two of these devices, and measured them separately at temperatures of $T \approx 20\,\mathrm{mK}$ in a dilution refrigerator.

The relevant energy scales in our devices can be obtained from Coulomb blockade measurements: Figure 1b shows Coulomb diamonds of the superconducting island alone, measured through conductance. The diamonds of device A display a clear even-odd pattern, indicating that the energy of the lowest odd-parity state, E_0, is smaller than the charging energy of the superconducting island, E_C^S (Fig. 1c) [57, 64, 160]. For this device, we estimate $E_0 = 72\,\mu\mathrm{eV}$ and $E_\mathrm{C}^\mathrm{S} = 112\,\mu\mathrm{eV}$ from the extent of the diamonds. Conversely, the charging of the superconducting is-

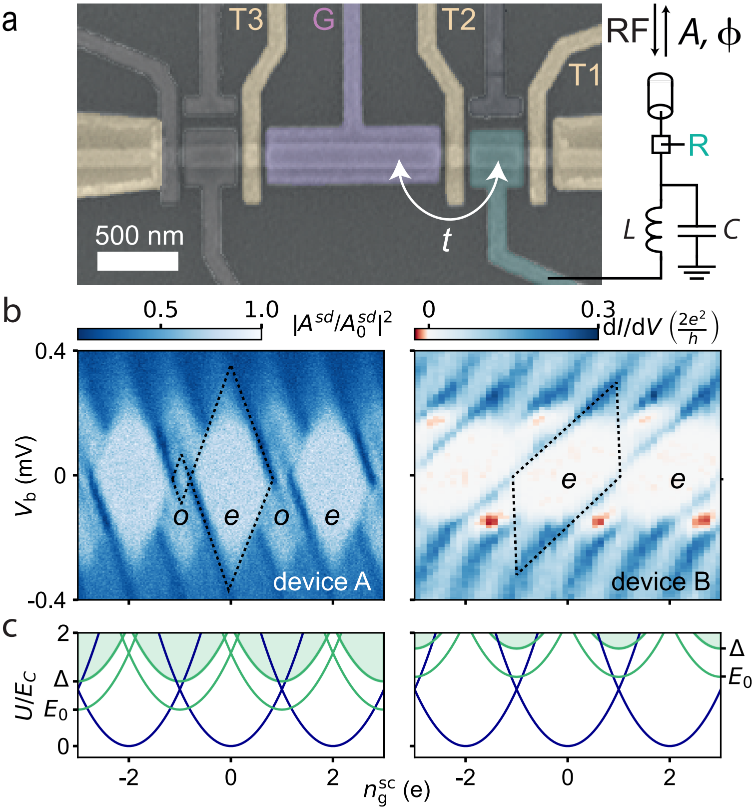

Figure 6.1 – Experimental setup and sample characterization. a False-colored electron micrograph of a nominally equivalent hybrid double dot. The plunger gate of the QD (island) is colored cyan (purple). A LC resonator is capacitively coupled via the gate of the QD. Its phase ϕ and amplitude A response are monitored at a constant probe frequency. **b** Coulomb blockade measurement of the SC. Left: for device A measured using RF reflectometry off the source (circuit not shown in **a**). The even-odd pattern indicates that $E_0 < E_C^S$. Right: for device B measured using standard lockin techniques. The doubling of the period at low bias V_b illustrates that $E_0 > E_C^S$. **c** Energy dispersion of the superconducting island for device A (left) and device B (right). The even (odd) energy levels are shown in darkblue (green). The odd parity sector consists of a discrete subgap state at E_0 and a continuum of states above Δ.

land of device B is 2e-periodic, indicating that $E_0 > E_C^S$ [63, 64]; here, we estimate $E_0 \approx 90\,\mu\text{eV}$ and $E_C^S \approx 70\,\mu\text{eV}$. While in an ideal BCS superconductor E_0 is equal to the superconducting gap Δ, current measurements on device A (Supplemental Material) and the negative differential conductance observed in device B indicate the presence of subgap states [52]. In both devices, the charging energy of the dot, $E_C^{QD} \approx 200 - 300\,\mu\text{eV}$, is the largest energy scale in the system, and the typical QD level spacing exceeds the thermal energy (Supplemental Material).

6.2. Results

6.2.1. Spin-dependent tunneling

In the following, we investigate the change in resonator response when charges are able to tunnel between the QD and SC at zero bias, beginning with device A. To this end, we form a hybrid double dot by tuning the gates T1 and T2 close to pinch-off, and T3 into pinch-off. Figures 2a,b show the resonator response as a function of the two plunger gates in the weakly coupled regime. Both the amplitude- and phase response display the charge stability diagram (CSD) of the hybrid double dot, which shows a clear 1e pattern along the QD gate, and an even-odd pattern along the SC gate; this is again a manifestation of $E_0 < E_C^S$, and the CSD shape can be readily reproduced by computing the charge ground states of the system (Supplemental Material).

We focus on the interdot transitions, highlighted in Figs. 2a-c, where we observe a strong amplitude and phase response on all charge degeneracy points. Interestingly, we see a strong difference in the resonator response across interdot transitions with a different parity of the total particle number, indicating a difference between the coupling between the involved states [84]. Two scenarios can lead to such a different coupling: One, an asymmetric electron- and hole coupling to the quasiparticle state in the SC [160]; and second, a difference in the available spin states for the different transitions [161].

We find that the latter situation can qualitatively describe the asymmetry in our data. To see this, we label the states according to their pairing; for the SC states as even/odd, and for the states in the QD as singlet/doublet: $|e/o, S/D\rangle$. We can differentiate couplings between two sets of states; $|e, D\rangle$ to $|o, S\rangle$ and $|e, S\rangle$ to $|o, D\rangle$. The coupling is different for these two sets, because they involve a different number of states. Only one spin channel contributes to the coupling between $|e, D\rangle$ and $|o, S\rangle$, while both spins of a Cooper-pair can couple to the QD doublet for the transition between $|e, S\rangle$ and $|o, D\rangle$ [161]. The “checkerboard”-like pattern in the CSD that results from this mechanism is in agreement with our data. This effect has originally been predicted for a double quantum dot and is thus not restricted to the QD-SC system [161]. The asymmetry from the electron or hole tunneling would result in a different pattern in the CSD; we thus conclude that the features observed in the data are most likely explained by the number of available spin states in the hybrid double dot.

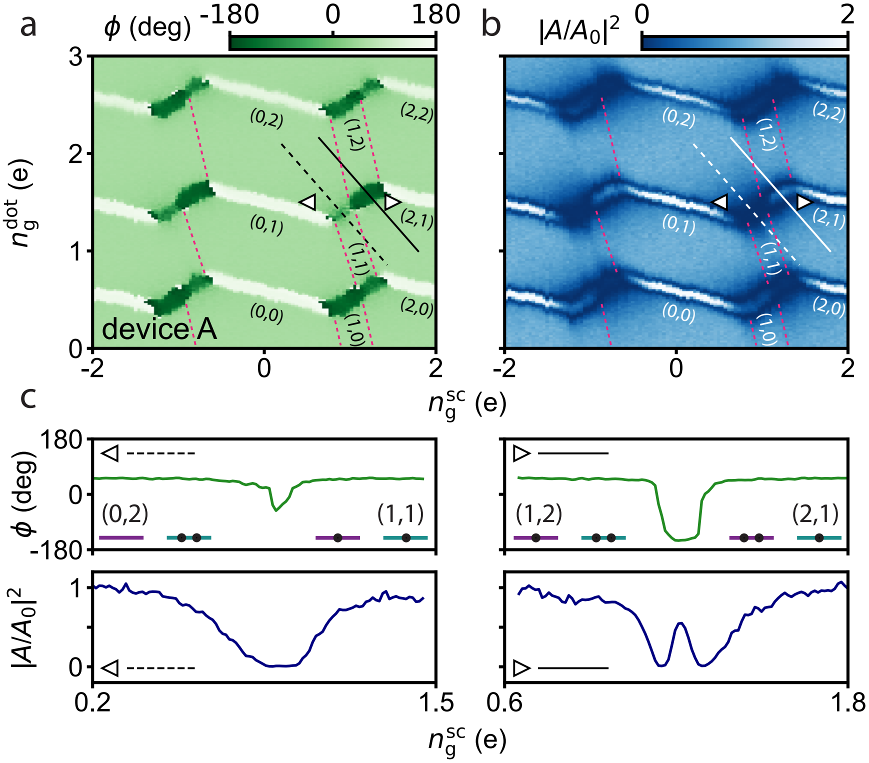

Figure 6.2 – **Spin-dependent tunneling between a QD and a SC.** **a** and **b** Charge stability diagram of device A measured in phase **a** and amplitude **b**. The charge states are labeled with (n^{SC}, n^{QD}) with respect to the state (N, M) with N and M even. Dashed pink lines: expected locations of the lead-island transitions. **c** Linecuts of the phase (green) and amplitude (blue) along the interdot transitions. The linecut crosses the states (0,2) and (1,1) in the left panel (dashed line) and (1,2) and (2,1) in the right panel (continuous line). A pronounced different resonator response is observed for the two transitions. For the $|e\text{(ven)}, S\text{(inglet)}\rangle$ to $|o\text{(dd)}, D\text{(oublet)}\rangle$ transition between (0,2) and (1,1) (left panel), both spin channels are available, while only one spin channel contributes to the $|o, S\rangle$ to $|e, D\rangle$ transition between (1,2) and (2,1) (right panel).

6.2.2. Cooper-pair tunneling

For device B, the situation changes significantly. The energy ordering $E_0 > E_\mathrm{C}^\mathrm{S}$ implies that quasiparticle states are not accessible (Fig. 1c). We form a hybrid double dot by tuning T1, T2, and T3 close to pinchoff. The CSD for a weak QD-SC coupling is shown in Fig. 3a. The diagram is $2e$-periodic in the SC gate, indicating that the island is charged via Andreev reflections from the lead. The QD is again $1e$-periodic. To model the measured CSDs, we compute the charge ground state by diagonalizing an effective Hamiltonian of the system that includes charging effects, the superconducting gap in the island, and coupling terms (Supplemental Material). This model, with the energy scales extracted from the Coulomb blockade measurements and an adjustable tunneling amplitude (rightmost panel in Fig. 3a), describes the observed CSD well.

The different gate charge periodicity for the QD and SC leads to interdot transitions that change the total charge of the dot-island system. This implies that a reservoir must be involved in the corresponding charge-transfer process. The observed resonator signal, with a linecut shown in Fig. 3b, results from tunneling on and off the QD, and thus should not contain information of SC-lead coupling [84]. A possible candidate for the precise underlying process that gives rise to our data is crossed Andreev reflection (CAR) [152, 153]. There, a hole from the QD is converted to an electron in the lead, consistent with the charge states involved in the experiment. This process is exponentially suppressed in the length of the island $\exp(-L/\pi\xi)$, where ξ is the superconducting coherence length [162]. Still, with $L = 1.2\,\mu\mathrm{m}$ and assuming a coherence length of $\xi \sim 260\,\mathrm{nm}$ [41] this remains a plausible scenario.

Interestingly, increasing the tunnel coupling allows for bringing the system into a regime where a particle-conserving interdot transition emerges. The CSD in a more strongly coupled regime, together with a simulation of the charge ground states is shown in Fig. 3c. In this regime, we assume an induced gap in the quantum dot, consistent with earlier studies in the context of YSR states [155]. Here, we observe that the regions with odd charge number in the QD shrink, while the regions with an even number of QD charges connect, resulting in an even-odd pattern in both gates. Now, the interdot transition shows a purely dispersive signal (Fig. 3d): we observe only a small phase shift, without any amplitude response; this is indicative of a coherent transition. We can thus conclude that this transition is caused by coherent Cooper-pair transfer between the dot and the island, resulting in an anti-crossing in the energy spectrum.

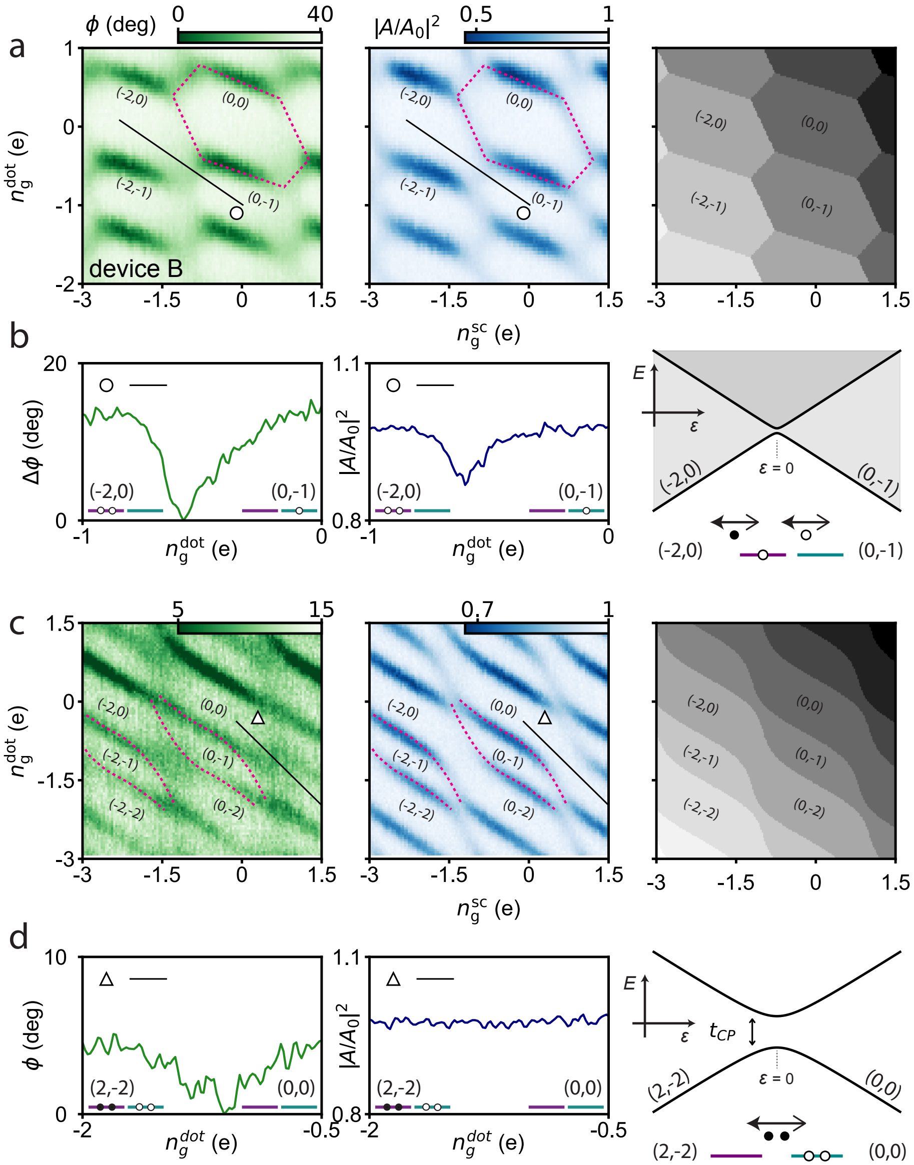

Figure 6.3 – Cooper-pair tunneling in a hybrid double dot. **a** Charge stability diagram measured in phase (left) and amplitude (middle) along with a simulation of the charge ground state (right) in the weakly coupled regime. The charge states are labeled with $(n^{\mathrm{SC}}, n^{\mathrm{QD}})$ with respect to the state (N, M) with N even. Dashed pink lines: locations of the transitions from the (0,0) state as a guide to the eye. The gray scale in the simulation indicates the sum of the charge in the combined system. **b** Linecuts of the phase (green) and amplitude (blue) along the (-2,0) to (0,-1) interdot transition. This transition involves a reservoir with a continuous spectrum, indicated by the shaded region above the lowest available energy state. The schematic shows how these states couple via crossed Andreev reflection. **c** Same as in **a** for the strongly coupled regime. Dashed pink lines: locations of the lead transitions from the (-2,-1) and (0,-1) states as a guide to the eye. **d** Linecuts of the phase (green) and amplitude (blue) along the (2,-2) to (0,0) interdot transition. These states couple via coherent Cooper-pair tunneling. All data is measured in device B.

6.2.3. Floating regime

As we have seen, the main difference between the two devices is that the odd states of the SC can not be directly accessed in the regime $E_0 > E_C^S$. This changes in absence of lead reservoirs because quasiparticles that tunnel from the QD onto the SC are confined to the system [157]. The additional energy associated with decharging the QD makes Cooper-pair tunneling energetically unfavorable when $E_0 < E_C^S + E_C^{QD}$. We realize this situation experimentally in device B by closing the outer tunnel barriers, through gates T1 and T3. The resulting CSD and corresponding calculation of the ground state transitions are shown in Figs. 4a,b. It can readily be seen that no transitions to a reservoir take place, and the even-odd pattern is indicative of the alternating occupation of even and odd states of the SC.

Importantly, even though SC and QD are now galvanically isolated from the environment, the gate sensor still allows us to study the quasiparticle states in the SC. To establish this further, we study the evolution of the even-odd spacing as a function of temperature (Fig. 4c). This spacing is a measure for the free energy difference of the SC. In particular, the temperature evolution of the free energy difference can be used to identify and characterize subgap states [59]; for proximitized nanowires, this has earlier been studied in transport [52]. The extracted free energy difference $F_o - F_e$ as a function of temperature is shown in Fig. 4d. A fit to the model from Ref. 52 yields a gap of $\Delta = 220$ µeV, a subgap state energy of $E_0 = 106$ µeV, and an Al volume of $V = 2.9 \times 10^5$ nm^3, consistent with the dimensions of the island. We note that the slightly larger energy of the subgap state is consistent with the more negative plunger gate voltage for this measurement [94]. The excellent quality of the fit corroborates our initial assessment of the presence of a subgap state (Fig. 1b). This result shows clearly that the resonator response of the QD gate sensor can be used to characterize states of the SC, even when leads for transport experiments are not available.

6.3. Conclusions

In summary, we have performed dispersive gate sensing on a quantum dot that can exchange particles with a superconducting island. Analysis of the resonator response has allowed us to directly detect and identify the charge-tunneling processes that take place between the dot and the superconductor. We have found that single- or multi-particle tunneling processes take place, depending on the dominating energy scales of the hybrid double dot. In particular, our data shows that gate sensing provides an excellent tool for studying subgap excitations, even in situations where an absence of leads prohibits transport studies. Going forward, the ability to detect the coherent tunneling into subgap states will be crucial for the realization and operation of Majorana qubits based on proximitized nanowires [17, 18]. Our results thus set the stage for the implementation of quantum measurements of topological qubits.

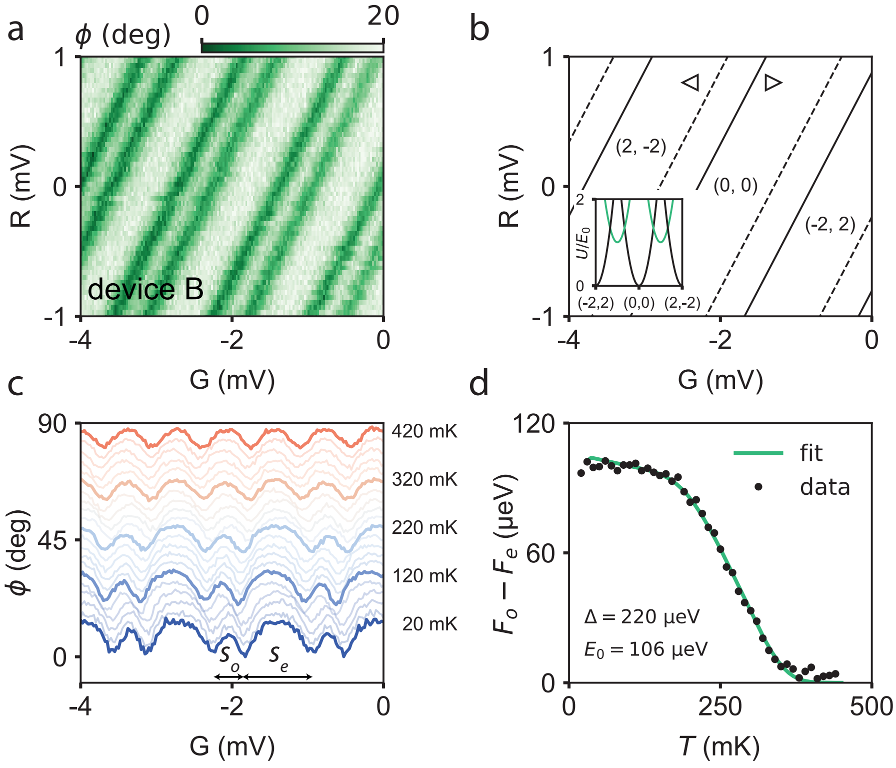

Figure 6.4 – **Re-enabling of single-particle tunneling in the floating regime a** Charge stability diagram measured in phase in device B. The anti-diagonal lines indicate that the total charge in the system is conserved. **b** The calculated positions of the transitions in good agreement with the measured stability diagram. Inset: energy spectrum with the even states in black and the odd states in green showing that the even-odd pattern is caused by the parity effect even though $E_0 > E_C^S$. **c** Temperature dependence of the even-odd pattern. **d** The evolution of the free energy difference with temperature. The free energy difference is extracted from the even-odd pattern via $F_\mathrm{o} - F_\mathrm{e} = (S_\mathrm{e} - S_\mathrm{o})\, e\alpha/4$ with $\alpha = 0.9$ the lever arm of G, and e the elementary electron charge.

6.4. Supplemental Material

6.4.1. Additional Coulomb diamond measurements

In this section, we present additional Coulomb blockade measurement of the quantum dots (QD) in Fig. 6.S1, and the superconducting island (SC) of device A in Fig. 6.S2.

From the Coulomb diamonds in Fig. 6.S1, we extract the QD charging energy and estimate the typical level spacing of the dot. We find that the charging energy is the largest energy scale for both QD-SC systems. Moreover, the level spacing, δ, exceeds the thermal energy for both QDs, and it fluctuates with the charge occupation in the QD.

Figure 6.S2 shows Coulomb diamonds for the SC of device A obtained via current

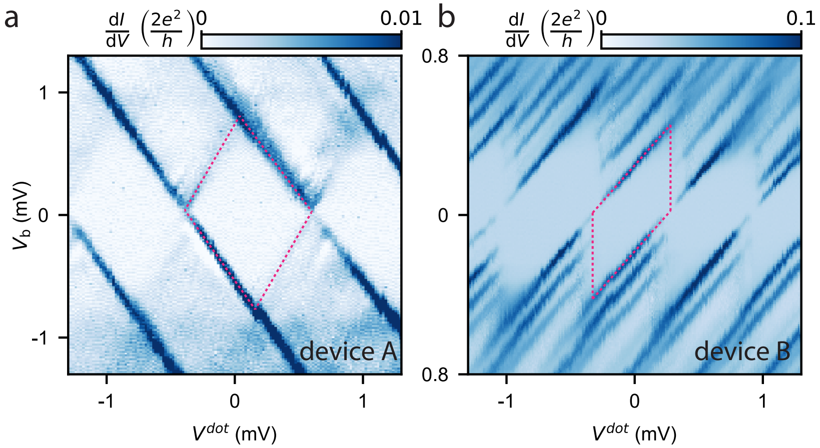

Figure 6.S1 – **Coulomb blockade measurements on the quantum dots.** **a** For device A, the conductance is calculated from the numerical derivative of the measured current. We extract $E_C^{\mathrm{QD}} \approx 300\,\mu\mathrm{eV}$, $\delta = 50{-}150\,\mu\mathrm{eV}$, and $\alpha^{\mathrm{QD}} = 0.8$. **b** For device B, we obtain $E_C^{\mathrm{QD}} \approx 200\,\mu\mathrm{eV}$, $\delta = 100{-}170\,\mu\mathrm{eV}$, and $\alpha^{\mathrm{QD}} = 0.72$.

measurements at the same gate settings as the diamond scan shown in Fig. 1b of the main text. The data in presented in the main text is measured using RF reflectometry from the source of the QD-SC system. The conductance shown here drops back to zero when V_b increase above the height of the small odd diamond. This indicates that for the odd charge states the current is carried by a discrete, subgap state. In contrast, if the current is carried by a continuum of states, the conductance would remain constant.

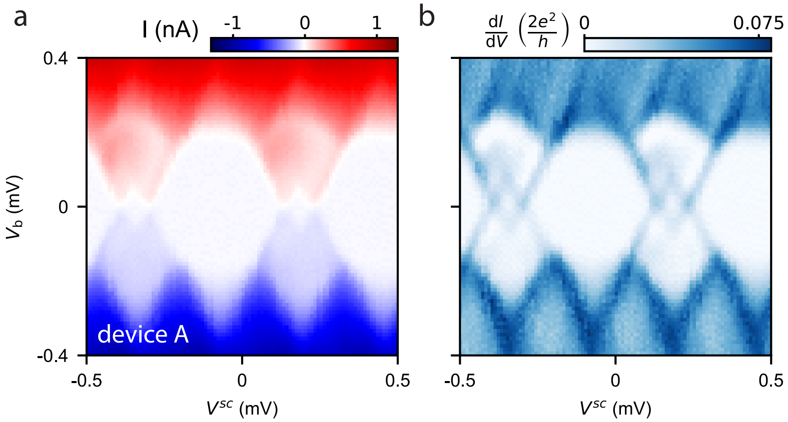

Figure 6.S2 – **Coulomb blockade measurements of the superconducting island in device A.** Left panel: current data, right panel: differential conductance obtained by taking the numerical derivative of the current data.

6.4.2. Simulation of the charge stability diagrams

In this section, we discuss the phenomenological model used to simulate the charge stability diagrams shown in Fig. 3 of the main text. We start with the Hamiltonian of the QD-SC system

$$H = H_C + H_{\mathrm{BCS}} + H_T, \tag{6.S1}$$

where H_C describes the charging energy of the combined system, H_{BCS} the superconductivity on the island and the induced superconductivity in the dot, and H_T the coupling between the two systems. Note that we neglect the level spacing in both systems. For the superconducting island, this is justified since its estimated level spacing is on the order of several mK. However, for the QD, where $\delta \approx 100$ µeV, this is a large simplification. We model the charging term by $H_C = H_C^{\mathrm{QD}} + H_C^{\mathrm{SC}} + H_{C_m}$

$$H_C^{\mathrm{i}} = \sum_{n^i} E_C^i \left(n^i - n_g^i\right)^2 \tag{6.S2}$$

$$H_{C_m} = \sum_{n^{\mathrm{SC}},n^{\mathrm{QD}}} E_{C_m} \left(n^{\mathrm{SC}} - n_g^{\mathrm{SC}}\right)\left(n^{\mathrm{QD}} - n_g^{\mathrm{QD}}\right) \tag{6.S3}$$

where $i = \mathrm{QD}, \mathrm{SC}$ labels the system; E_C^i is the charging energy, n_g^i the gate charge, and n^i labels the charge state.

We approximate the BCS Hamiltonian by assuming that only the lowest single particle state with energy E_0 is relevant

$$H_{\mathrm{BCS}} \approx \begin{cases} 0 & n^i \text{ is even} \\ E_0^i & n^i \text{ is odd.} \end{cases} \tag{6.S4}$$

Note that $E_0 = \Delta$ in case there are no subgap states present on the SC. Usually, $E_0^{\mathrm{QD}} = 0$, we included this term to be able to model induced superconducting correlations in the quantum dot when the QD-SC coupling is strong.

Lastly, for the tunneling Hamiltonian, we include both $1e$ and $2e$ charge-transfer processes: $H_T = H_T^{1e} + H_T^{2e}$ with

$$H_T^{1e} = \sum_{n^{\mathrm{SC}},n^{\mathrm{QD}}} t_{1e} \left|n^{\mathrm{SC}} - 1\right\rangle \left\langle n^{\mathrm{QD}} + 1\right| + \mathrm{h.c.} \tag{6.S5}$$

$$H_T^{2e} = \sum_{n^{\mathrm{SC}},n^{\mathrm{QD}}} t_{2e} \left|n^{\mathrm{SC}} - 2\right\rangle \left\langle n^{\mathrm{QD}} + 2\right| + \mathrm{h.c.}, \tag{6.S6}$$

where t_{1e} (t_{2e}) is the tunneling amplitude for the 1e (2e) process.

To simulate the charge stability diagrams, we construct a Hamiltonian based of a finite number of charge states $|n^{\mathrm{SC}}, n^{\mathrm{QD}}\rangle = |-4,-4\rangle, |-4,-3\rangle, \ldots, |4,4\rangle$, using Kwant [163], and numerically solve for its eigenvalues and eigenvectors. We use the eigenvectors to calculate the charge expectation value of the total system which we compare to the data.

Additional information simulations

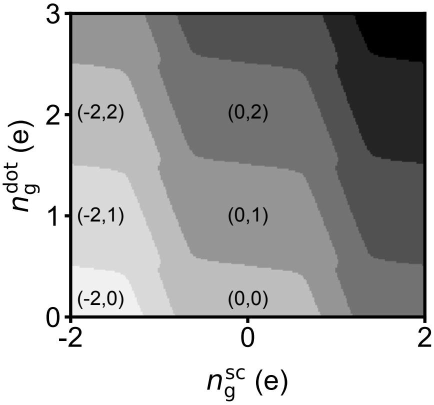

Figure 6.S3 – Simulation of the charge stability diagram of Fig. 2 of the main text. The gray scale indicates the total charge in the hybrid double dot.

Table 6.S1 – Overview of the parameters used in the simulations. All values are in μeV.

Simulation	E_C^{SC}	E_C^{QD}	E_{C_m}	E_0^{SC}	E_0^{dot}	t_{1e}	t_{2e}
Fig. 3a	72	230	50	88	0	9	0
Fig. 3c	72	230	60	88	18	176	308
Fig. 6.S3	112	500	50	72	0	35	0

7

Quantized conductance and large g-factor anisotropy in InSb quantum point contacts

InSb plays an important role in research on Majorana zero modes because of its strong spin-orbit interaction and large Landé g-factor. To further explore the novel properties of these Majorana quasiparticles, hybrid devices based on quantum wells have gained interest as an alternative approach to nanowires. In this work, we report a pronounced conductance quantization of quantum point contacts in InSb/InAlSb quantum wells. By rotating the magnetic field, we observe a large anisotropy between the in-plane ($|g_1| = 26$) and out-of-plane ($|g_1| = 52$) g-factor. Additionally, we investigate crossings of subbands with opposite spins, and extract the effective electron mass from magnetic depopulation of the one-dimensional subbands.

This chapter is based on F. Qu, J. van Veen, F. K. de Vries, A. J. A Beukman, M. Wimmer, W. Yi, A. A. Kiselev, B-M. Nguyen, M. Sokolich, M. J. Manfra, F. Nichele, C. M. Marcus, and L. P. Kouwenhoven, Quantized conductance and large g-factor anisotropy in InSb quantum point contacts, *Nanoletters* **16**, 7509-7513 (2016).

7.1. Introduction

One-dimensional (1D) InSb structures are promising for spintronics [164] and topological quantum computation [165, 166]. InSb has the smallest effective electron mass and the highest room-temperature mobility among the binary III-V semiconductors [167]. It further exhibits strong spin-orbit interaction (SOI) and the largest Landé g-factor ($|g| = 51$ for the bulk). These properties arise because of the strong coupling between conduction- and valence band resulting from the small band gap [167–169]. A magnetic field applied perpendicular to the spin-orbit field of these nanowires opens a Zeeman gap and creates helical states [170]. Now, a 1D topological superconductor, with Majorana zero modes (MZMs) at its boundaries, can form when a superconducting gap is induced through the proximity effect. These MZMs possess non-Abelian exchange statistics. However, an exchange between MZMs requires a quasi two-dimensional (2D) network of topological superconductors [15, 16, 38, 81]. The Majorana box qubit, introduced in section 2.4.1, is an example of such a network and consists of two parallel topological wires connected by a trivial superconductor. Although, crossed nanowires have been developed [171, 172], simultaneously applying magnetic fields parallel to different branches of these nanocrosses is difficult. Furthermore, scaling nanowire-based systems for topological quantum computing might be challenging[1]. Alternatively, these networks could be realized using a top-down approach; starting from 2D quantum wells, wires and networks can be defined by etching or electrostatic gating. As a first step towards MZM physics in quantum wells, control over nanostructures such as quantum point contacts (QPCs) and quantum dots should be established. In this chapter, we report on ballistic transport through QPCs in an InSb 2D electron gas (2DEG). We study the Zeeman spin splitting of the energy bands as a function magnetic field direction and observe a large in-plane/out-of-plane g-factor anisotropy. Additionally, we deduce the electron effective mass using magnetic depopulation of the subbands.

InSb quantum wells have several advantages over InSb nanowires. Their mobility[2] can exceed 200,000 cm^2/Vs [175–177], corresponding to a mean free path larger than 1.4 µm. This is a factor 5 to 10 larger than typical mobilities in InSb nanowires [98]. Moreover, the 2DEG functions as an ideal contact which naturally solves the interface problem for nanowires [98]. Although the calculated and reported Rashba SOI parameter α ranging between 0.03 and 0.15 eVÅ [178–183] is smaller than that reported in nanowires [168, 184], a 2D heterostructure enables tuning of SOI strength by engineering asymmetric doping, barrier modulation, and electrical gating [178, 179, 181–183, 185]. Moreover, the confinement of 1D structures defined on an InSb 2DEG may enhance α towards the values for nanowires. Despite these advantages, only one work reported on the observation of quantized conductance in InSb 2DEG QPCs thus far [186]. In contrast, ballistic transport in

---

[1] Recently, (proximitized) InAs nanowires have developed using the bottom-up method called selective area growth [173, 174]. This scalable technique could offer a different route (as compared to 2DEGs) to complex nanowire networks.

[2] The Hall bar measurments on our InSb wafer indicate a maximum mobility of roughly 180,000 cm^2/Vs (Fig. 7.1a).

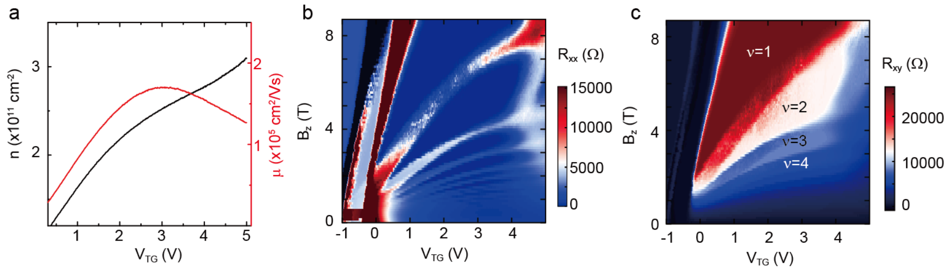

Figure 7.1 – Characterization of an InSb Hall bar. **a** Density (black) and mobility (red) as a function of top gate voltage V_{TG}. The mobility drops around V_{TG} = 3 V due to occupation of the second subband. **b** Longitudinal resistance R_{xx} and **c** Hall resistance R_{xy} as a function of both V_{TG} and out-of-plane magnetic field B_z. At high magnetic field, the integer quantum Hall effect is observed; R_{xx} reaches zero (dark blue region in **b**) and quantized Hall plateaus form (marked by the filling factors in **c**). These results are similar as for Hall bars made with HfO_2 as dielectric on the same wafer [175].

InSb nanowires has already been established [187–189]. This discrepancy arises because the gate leakage problem, which prevented successful gate depletion of InSb 2DEGs, has only recently been solved [175, 190]. Our hall bar measurements show well-developed integer quantum hall plateaus together with the longitudinal resistance dropping to zero (Figs. 7.1b,c), indicating proper gating without gate leakage, or creation of parallel conduction channels.

7.2. Fabrication and methods

The InSb/InAlSb heterostructure used in this work is grown on a GaAs (100) substrate using a fully relaxed $In_{1\text{-}x}Al_xSb$ buffer (x = 0.08). The quantum well consists of a 30 nm InSb layer sandwiched between $In_{1\text{-}x}Al_xSb$ barriers. Single-side Si δ-doping sits 20 nm above the InSb well in the top barrier. Details of the material growth, and the full gate depletion of the 2DEG in Hall bar devices with HfO_2 as dielectric have been reported earlier [175]. These results have been reproduced using SiN_x as dielectric (Fig. 7.1). To fabricate the QPC device studied here, a narrow constriction (≈280 nm wide) on a 20 μm wide mesa is wet etched ≈100 nm deep (see Fig. 7.2a). The InSb 2DEG at both sides of the constriction functions as an in-plane side gate (SG). Next, the Ohmic contacts are formed > 20 μm away from the QPC by etching into the InSb layer using an Argon ion etch, and the subsequent in-situ deposition a Ti/Au layer. Finally, the top gate is made using a 100 nm thick SiN_x dielectric layer followed by evaporating a 100 nm wide Ti/Au electrode. We also fabricated fully gate-defined QPCs, in which, instead of etching, the constriction is defined by two split Ti/Au gates on top of a SiN_x dielectric layer, and a global Ti/Au top gate on a second SiN_x layer.

Transport measurements are carried out on the two types of QPCs in both a cryo-free dilution refrigerator with a 6-2-1 T vector magnet and a ^{3}He system with a single axis magnet of 9 T. Standard low-frequency lockin techniques are employed in a 2-

terminal or 4-terminal measurement configuration; The differential conductance $G = \mathrm{d}I/\mathrm{d}V = I_{ac}/V_{ac}$ is measured by applying a small AC excitation voltage V_{ac}, and measuring the resulting AC current I_{ac}. The series resistances from the wires, measurement equipment, and adjacent InSb 2DEG have been subtracted to match the quantized conductance for the data reported below, unless otherwise stated. For the source-drain bias spectroscopy, the voltage drop on the QPC is corrected accordingly. By comparing the two types of QPCs, we find that the etch-defined QPC shows pronounced quantized conductance plateaus at zero magnetic field, while the fully gate-defined type requires a small perpendicular magnetic field to suppress backscattering and interference. Therefore, we focus on the former in the following, and briefly present the results on the latter in Fig. 7.S1 of the Supplemental Material.

7.3. Results

7.3.1. Quantized conductance and spin splitting

Figure 7.2b shows G as a function of side gate voltage V_{SG} with a fixed top gate voltage V_{TG} = 0.3 V at different temperatures. Quantized conductance plateaus at nG_0 are observed resulting from the ballistic transport in the 1D constriction, where n = 1, 2 and 3, and $G_0 = 2e^2/h$ with h Planck's constant and e the elementary charge. At T = 26 mK, small conductance fluctuations indicate finite backscattering and interference processes around the QPC. The rest of the reported data are all measured at 26 mK. As shown in Fig. 7.2c, G can be controlled by the top as well as the side gates, confirming their proper functioning. Figure 7.2d displays the numerically calculated derivative of G with respect to the side gate voltage, i.e. the transconductance $\mathrm{d}G/\mathrm{d}V_{SG}$, versus V_{SG} and V_b (see Fig. 7.S2 of the Supplemental Material for the raw data). As indicated by the green arrows, the subband spacings E_{2-1} and E_{3-2} are roughly equal ≈4.6 meV, suggesting a near-parabolic confinement potential. Here, E_{i-j} represents the energy spacing between the ith and jth subband.

We examine the spin splitting of the 1D subbands in a magnetic field. Figure 7.3a shows G as a function of V_{SG} and B_x (along current flow). As B_x increases from 0 T, half-integer plateaus resulting from Zeeman spin splitting appear and widen in V_{SG}, while the integer plateaus narrow down. The evolution of the spin resolved subbands with B_x is illustrated in the right panel of Fig. 7.3b, ignoring SOI. At B_x = 3 T, only the half-integer plateaus survive because the spin-down band from the ith subband ($i \downarrow$) crosses the spin-up band from the $(i+1)$th subband ($(i+1)\uparrow$), as indicated by the green curve in the left panel of Fig. 7.3b. When B_x > 3 T, after the crossing of the spin split subbands, the spin-up bands $1\uparrow$ and $2\uparrow$ are the lowest two bands in energy, and the current is fully spin-polarized for $1G_0$. The combination of a large g-factor and a modest subband separation enables such clear crossing at a moderate magnetic field [187, 191]. When two 1D subbands of opposite spins cross, a spontaneous spin splitting and the emergence of the so-called 0.7 analog at the 1.5 plateau have been reported in GaAs 2DEGs [191], which, as well as the $0.7G_0$ feature, are absent in our InSb QPCs.

In contrast to the case of B_x, at large B_z > 1 T (out-of-plane), all plateaus widen due to Zeeman splitting and magnetic depopulation of 1D subbands (Fig. 7.4a).

This effect will be discussed in more detail below. For the case of B_y (in-plane but perpendicular to current flow), the behavior is similar to that in B_x, although here the measured magnetic field range is smaller (see Fig. 7.4b).

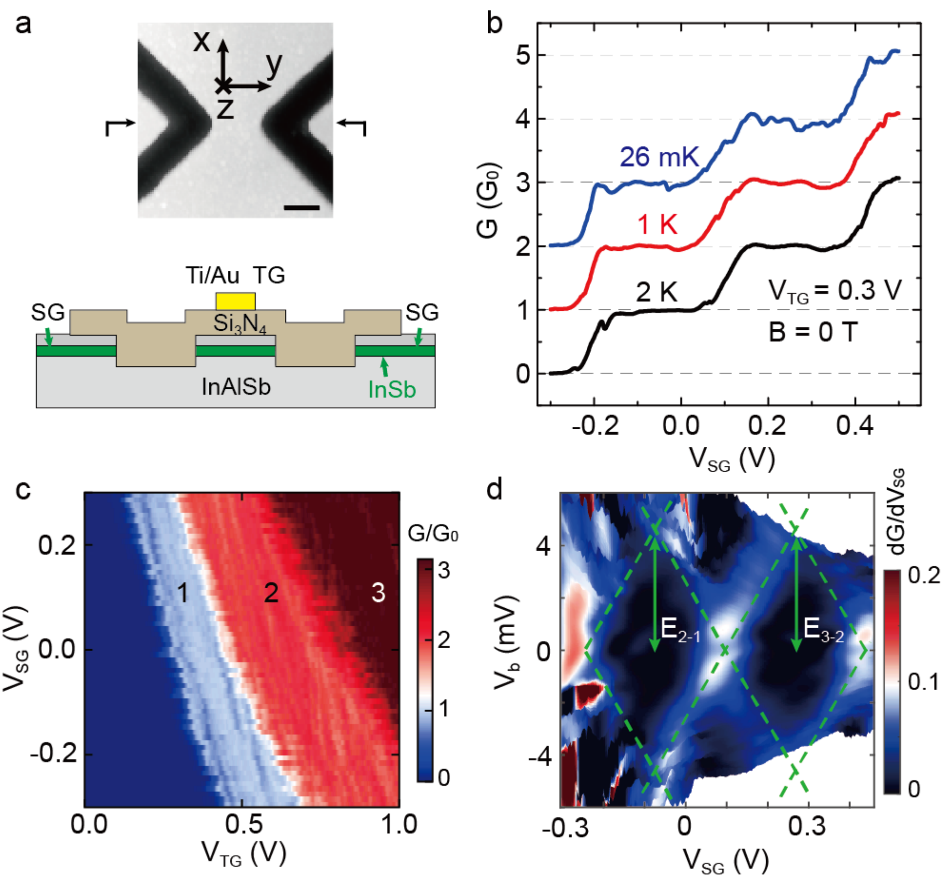

Figure 7.2 – Quantized conductance in an etch-defined InSb QPC. a Image and schematics of the etch-defined QPC. The top panel shows an atomic force micrograph of the constriction after the mesa etch (before depositing the SiN_x and Ti/Au layers). The black region is roughly 100 nm deep. The scale bar is 200 nm. The axes illustrate the vector magnet orientations. The bottom panel displays the cross-section of the device along the plane marked by the two arrows in the top panel. The constriction is controlled by two etch-defined in-plane side gates (SG) and a 100 nm wide top gate (TG). **b** Differential conductance G versus V_{SG} curves at a fixed V_{TG} = 0.3 V for different temperatures. The traces are offset by $1G_0$ ($G_0 = 2e^2/h$) for clarity. **c** G as a function of both V_{TG} and V_{SG}, demonstrating the proper working of both gates. **d** Numerically calculated transconductance $\mathrm{d}G/\mathrm{d}V_{SG}$ as a function of V_{SG} and V_b at V_{TG} = 0.3 V. The green dashed lines are guides-to-the-eye and the green solid arrows indicate the subband spacings.

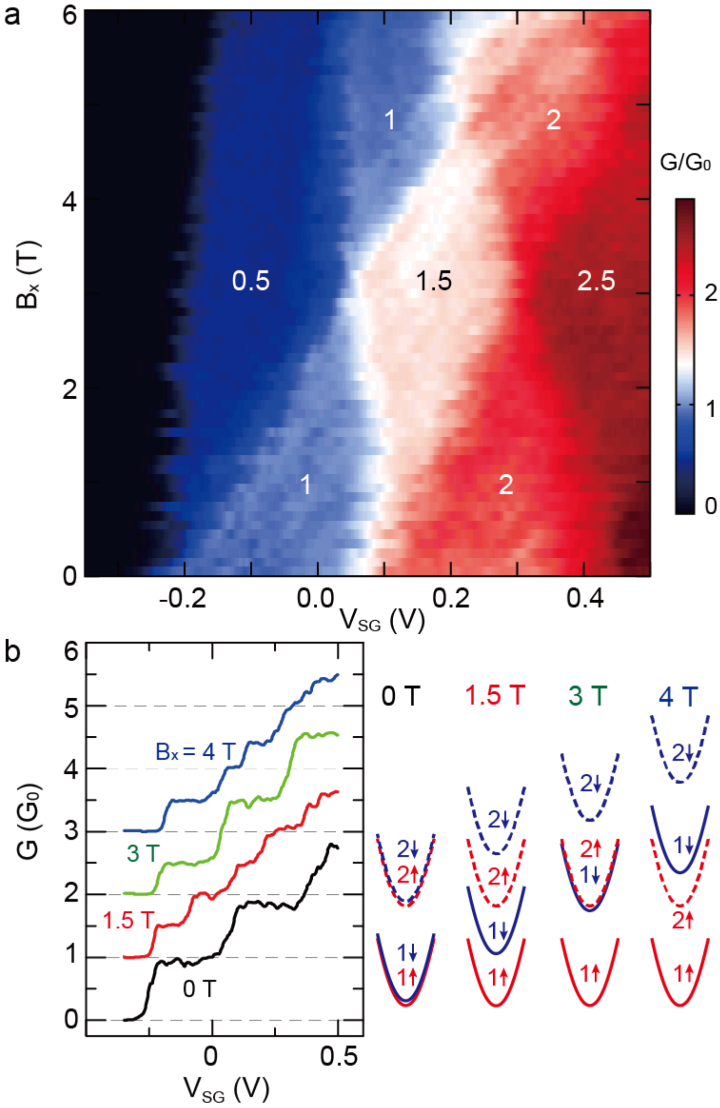

Figure 7.3 – Crossings of electron subbands with opposite spins. **a** G versus V_{SG} and B_x (along current flow) at V_{TG} = 0.3 V with n labeling the quantized conductance plateaus at nG_0. **b** The left panel shows linecuts taken from **a** at different magnetic fields. Traces are offset by $1G_0$ for clarity. The right panel displays band dispersions at different B_x, sketching the evolution of the spin-resolved subbands.

7.3.2. g-factor anisotropy

Next, we inspect the evolution of the spin splitting in different magnetic field directions, by rotating the field in the $x - z$ plane (Fig. 7.4c) and the $x - y$ plane (Fig. 7.4d), while keeping the amplitude fixed at 1.8 T and 1 T respectively. The magnetoresistance from the adjacent InSb 2DEG increases as the B_z component rises. Consequently, after subtracting a constant series resistance at $B_z = 0$, the calculated conductance at finite B_z is lower than the actual value, and the conductance plateaus labeled by 0.5 and 1 in Fig. 7.4c drop below their respective values (see Supplemental Material Fig. 7.S4a). Interestingly, when the B_z component increases by rotating the field both the 0.5 and the 1 plateau widen in V_{SG}. Assuming a constant gate voltage to energy conversion (i.e lever arm), the Zeeman splitting in the first subband, $E_{1\downarrow-1\uparrow} = |g_1|\mu_B B$ with μ_B the Bohr magneton, is proportional to the width of the 0.5 plateau along the gate voltage axis. Figure 7.4c thus shows a g-factor anisotropy up to a factor of two between the z and x directions (see Supplemental Material Fig. 7.S4b). In contrast, the in-plane ($x - y$ plane) g-factor is nearly isotropic as follows from the roughly constant width of the 0.5 plateau in Fig. 7.4d (see Supplemental Material Fig. 7.S5a).

To determine the magnitude of the g-factor quantitatively, source-drain bias spectroscopy is performed. Figures 7.5a, b, and c show the numerically calculated transconductance $\mathrm{d}G/\mathrm{d}V_{SG}$ as a function of V_{SG} and V_b at B_z = 2 T, B_z = 1.5 T, and B_x = 2 T respectively, with a fixed V_{TG} = 0.5 V. The green dashed lines are guides-to-the-eye and help to read the energy spacings as marked by the green solid arrows. From $E_{1\downarrow-1\uparrow} = |g_1|\mu_B B$, the effective g-factor for the first subband can be extracted to be $|g_{1,z}| \approx 51$ (B_z = 2 T), $|g_{1,z}| \approx 53$ (B_z = 1.5 T), and $|g_{1,x}| \approx 26$ (B_x = 2 T), exhibiting an anisotropy, as already anticipated by Fig. 7.4c. We would like to emphasize that the difference in absolute values between $|g_{1,z}|$ and $|g_{1,x}|$ of $\approx$26 is large. Consistent with Fig. 7.4d, the extracted $|g_{1,y}| \approx 28$ is close to $|g_{1,x}|$, showing a nearly isotropic in-plane g-factor (see Supplemental Material Fig. 7.S5). In 2D quantum wells, the effective electron g-factor becomes anisotropic due to lower symmetry introduced by the heterostructure. It is also renormalized (usually reduced) due to subband confinement and strain [192–195]. The 1D constriction may further modify the effective g-factors. Still, the extracted anisotropy is larger than expected based on theoretical calculations [192, 193]. The effective g-factor for the second subband can also be obtained from $E_{2\downarrow-2\uparrow}$ giving $|g_{2,z}| \approx 38$ (B_z = 1.5 T) and $|g_{2,x}| \approx 23$ (B_x = 2 T), both smaller than the first subband, in qualitative agreement with experimental results on quantum dots in InSb nanowires [168].

The extracted g-factor anisotropy of $|g_{1,z}|/|g_{1,x}| \approx 2$ from the bias spectroscopy agrees well with the anisotropy suggested by the width of the 0.5 plateau (ΔV_{SG}) in Fig. 7.4c, in line with the assumption of a constant lever arm. Therefore, we can use ΔV_{SG} to deduce the g-factor at different angles in the x-z plane. Figure 7.6a shows the transconductance $\mathrm{d}G/\mathrm{d}V_{SG}$ of Fig. 7.4c, where the white-red color represents the transition between conductance plateaus. The green arrow illustrates the width of the 0.5 plateau ΔV_{SG}. The g-factor for the first subband $|g_1|$ can be now obtained from $|g_{1,z}| \times \Delta V_{SG}(\text{angle})/\Delta V_{SG}(\text{angle} = 90^{\circ})$ with $|g_{1,z}| \approx 52$. Figure 7.6b presents the angular dependence of $|g_1|$.

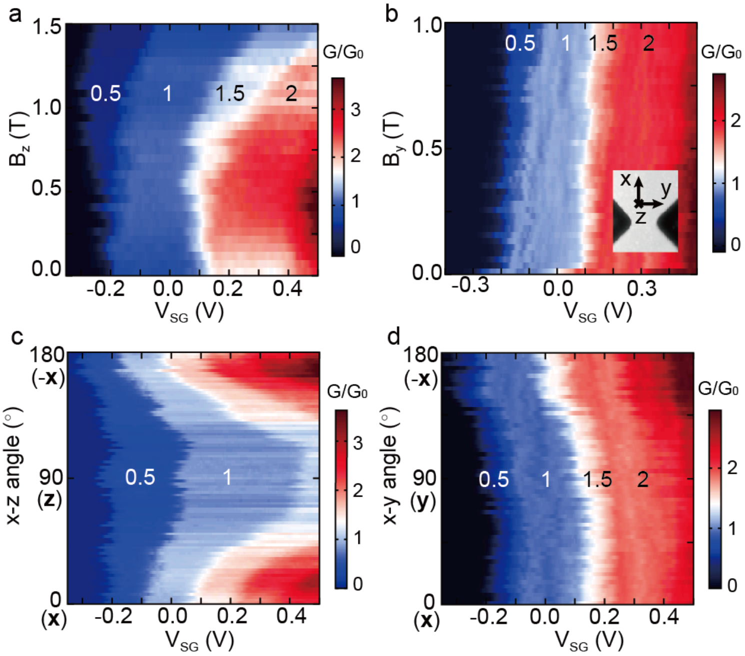

Figure 7.4 – Spin splitting in different magnetic field directions. **a** G versus V_{SG} and B_z, **b** G versus V_{SG} and B_y with numbers n marking quantized conductance at nG_0 (V_{TG} = 0.3 V). **c** and **d** G as a function of V_{SG} and the $x-z$ angle at a fixed magnetic field amplitude of 1.8 T **c**, and the $x-y$ angle at a fixed magnetic field amplitude of 1 T **d**. The $x-z$ angle = 0, 90, and 180 degrees correspond to magnetic field along x, z, and $-x$, respectively. Accordingly, in the $x-y$ plane these three angles stand for the x, y, and $-x$ directions.

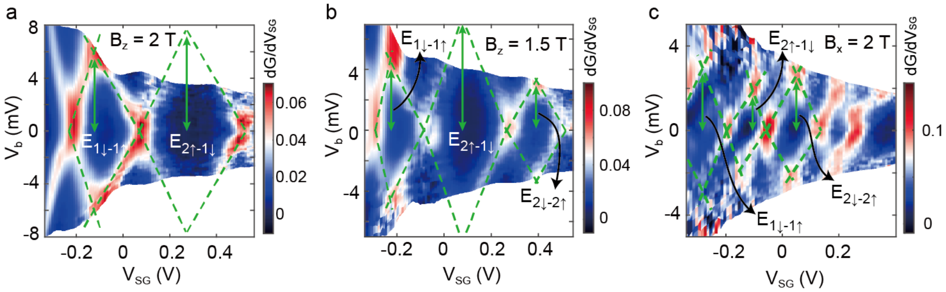

Figure 7.5 – Bias spectroscopy and g-factors. Transconductance dG/dV_{SG} as a function of V_{SG} and V_b at **a** B_z = 2 T, **b** B_z = 1.5 T, and **c** B_x = 2 T with a fixed V_{TG} = 0.5 V. The larger dG/dV_{SG} (red color) represents transitions between quantized conductance plateaus. Green dashed lines are guides-to-the-eye, and green solid arrows indicate the subband spacings.

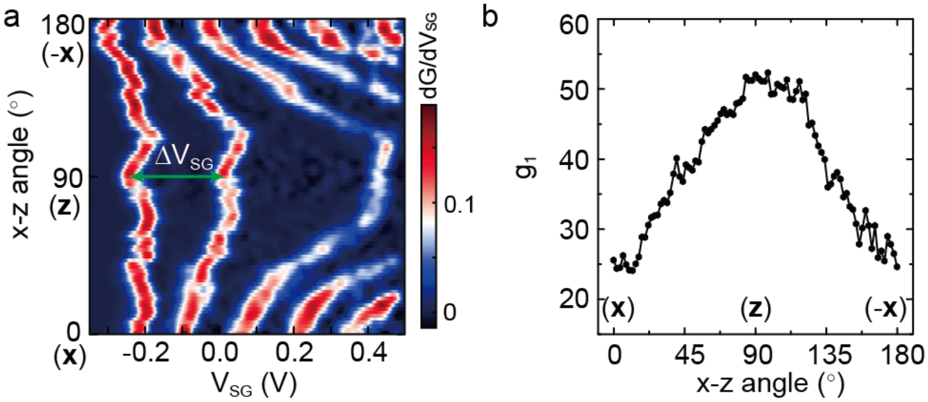

Figure 7.6 – **Anisotropic g-factors.** **a** Transconductance $\mathrm{d}G/\mathrm{d}V_{SG}$ extracted as the numerical derivative of the data in Fig. 7.4c. The green arrow indicates the width of the 0.5 plateau ΔV_{SG}. **b** First subband g-factor $|g_1|$ in the $x-z$ plane calculated based on ΔV_{SG}.

7.3.3. Magnetic depopulation

Next, we turn to magnetic depopulation to extract the effective electron mass. At $B = 0$, the parabolic confinement from the gates (as indicated by the fact that $E_{2-1} \approx E_{3-2}$ in Fig. 7.2d) results in a constant subband spacings of $\hbar\omega_0$ (with $\hbar = h/2\pi$). When a perpendicular magnetic field (along z) is applied, an additional magnetic parabolic potential enhances the level separation to $\hbar\sqrt{\omega_0^2 + \omega_c^2}$, where $\omega_c = eB_z/m^*$ is the cyclotron frequency with m^* is the effective mass [196–198]. Hence at finite B_z, m^* can be extracted from the subband spacing

$$E_{2-1}\left(B_z\right) = \frac{1}{2}\left(E_{1\downarrow-1\uparrow} + 2E_{2\uparrow-1\downarrow} + E_{2\downarrow-2\uparrow}\right) = \hbar\sqrt{\omega_0^2 + \omega_c^2}. \tag{7.1}$$

Neglecting the orbital effect of B_x, we find $\hbar\omega_0 \approx 4.7$ meV ($\omega_c = 0$) using the energy intervals in Fig. 7.5c at $B_x = 2$ T ($E_{1\downarrow-1\uparrow} \approx 3.0$ meV, $E_{2\uparrow-1\downarrow} \approx 1.9$ meV, and $E_{2\downarrow-2\uparrow} \approx 2.6$ meV). Consequently, applying the energy separations at $B_z = 1.5$ T and 2 T, the effective mass is calculated to be $m^* \approx 0.017m_e$ and $0.019m_e$, respectively, with m_e the electron rest mass. For an InSb quantum well, confinement enhances the effective mass, and the nonparabolicity of the band dispersion enhances it further at finite densities [193]. The average m^* of $0.018m_e$ is larger than the bulk value of $0.014m_e$ [167], but is consistent with theoretical calculations for a 30 nm thick InSb quantum well at low densities [193].

7.4. Conclusions

We have demonstrated high quality conductance quantization in QPCs on InSb quantum wells. The Zeeman spin splitting is investigated as a function of field angle, and a surprisingly large anisotropy between the in-plane and out-of-plane *g*-factor is observed. In a moderate in-plane magnetic field, clear crossings of electron subbands with opposite spins are achieved. Moreover, for the first time, the electron effective mass is extracted from magnetic depopulation of 1D subbands in InSb QPCs. Further research on carefully designed hybrid devices in InSb quantum wells is needed to pursue helical states and Majorana zero modes.

7.5. Supplemental Material

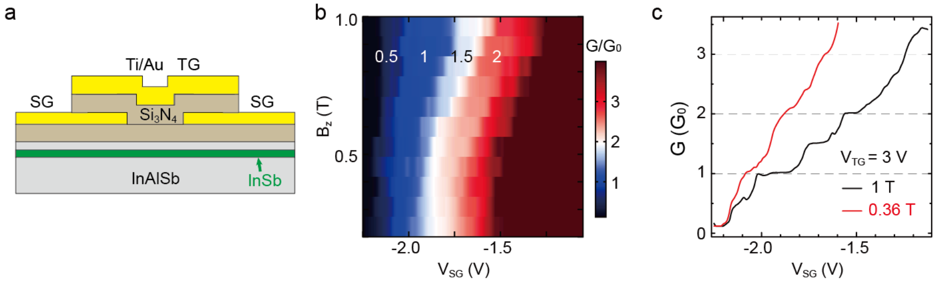

Figure 7.S1 – Results on fully gate-defined QPCs. **a** Cross-section of the fully gate-defined InSb QPC. The constriction is defined by two split side gates, separated by 400 nm on top of a $\mathrm{SiN_x}$ dielectric (100 nm thick), and a global top gate. **b** Typical color plot of G (in units of $G_0 = 2e^2/h$) versus V_{SG} and B_z at a fixed V_{TG} = 3 V (the top gate is separated by 270 nm $\mathrm{SiN_x}$ in total) and T = 0.3 K. In general, this type of QPC requires a small perpendicular magnetic field to suppress conductance fluctuations associated with backscattering and interference. **c** Linecuts taken from **b** (with the series resistance subtracted) showing quantized conductance in a finite B_z. By a comparison of the quality of quantized conductance plateaus, the etch-defined QPC shown in the main text is preferred for further research on helical states and Majorana zero modes.

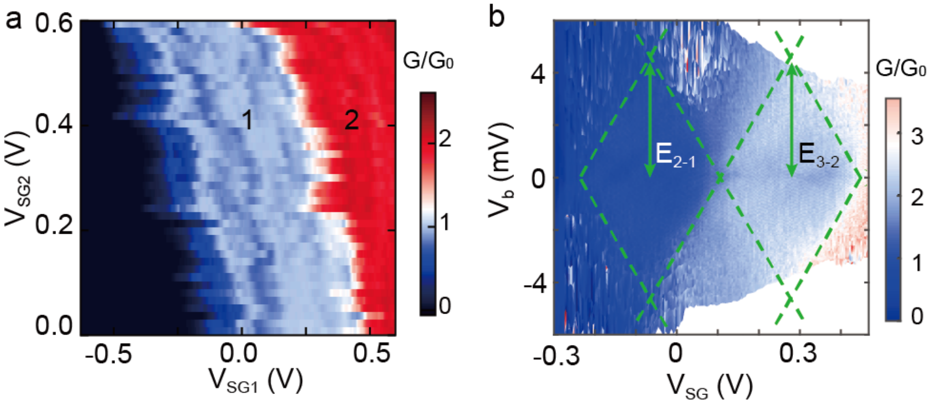

Figure 7.S2 – Differential conductance G at B = 0 for the etch-defined QPC shown in the main text. **a** G as a function of the voltage V_{SG1} and V_{SG2} on each of the two in-plane side gates, at a fixed V_{TG} = 0.5 V. **b** G versus source-drain bias voltage V_b and V_{SG} ($V_{SG} \equiv V_{SG1} = V_{SG2}$) at a fixed V_{TG} = 0.3 V. The numbers $n = 1, 2$ in **a** represent quantized conductance at nG_0. Note that the pinch-off voltage in **a** has a slope of ≈ -1 ($\Delta V_{SG2}/\Delta V_{SG1} \approx$ 0.6 V/(-0.5 V)), suggesting equal-coupled side gates. The green dashed lines in **b** are guides-to-the-eye, marking the transitions between quantized conductance plateaus. The transconductance shown in Fig. 7.2d in the main text is numerically calculated from the data in **b**. Level separations are labeled by E_{2-1} and E_{3-2}.

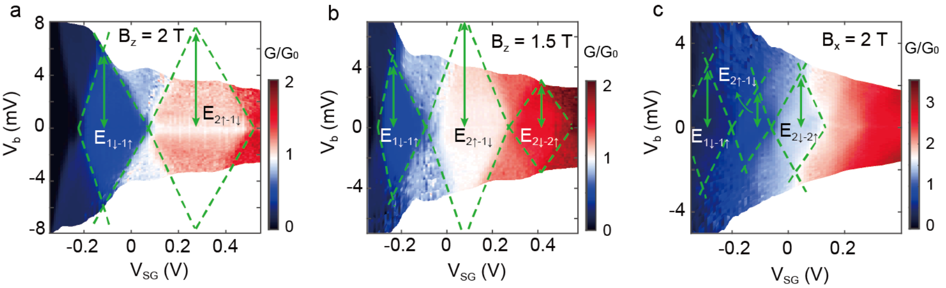

Figure 7.S3 – Differential conductance G for the etch-defined QPC shown in the main text. G as a function of V_{SG} and V_b at **a** B_z = 2 T, **b** B_z = 1.5 T, and **c** B_x = 2 T at a fixed V_{TG} = 0.5 V. The numerically calculated transconductance shown in Fig. 7.5 in the main text is calculated based on these plots. Green dashed lines are guides-to-the-eye, and green solid arrows illustrate subband spacings.

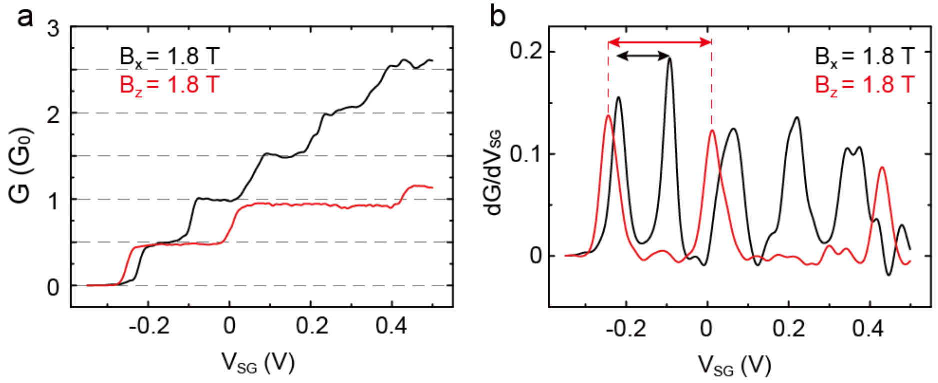

Figure 7.S4 – Linecuts taken from Fig. 7.4c in the main text. **a** Two line cuts at $x - z$ angle = 0 (along current flow, B_x = 1.8 T, black) and 90 degrees (B_z = 1.8 T, red). For the whole 2D color plot of Fig. 7.4c a series resistance of 6.5 kΩ from the adjacent InSb 2DEG is subtracted to match the quantized conductance at B_x = 1.8 T (black). However, when the B_z component increases, the magnetoresistance of the adjacent 2DEG rises and therefore the calculated conductance of the QPC drops below the actual value. As shown by the red line, the conductance at the quantized plateaus is lower than the expected value. Nevertheless, the width of the 0.5 plateau at B_z = 1.8 T is wider than that at B_x = 1.8 T, indicating a g-factor anisotropy. The exact width can be obtained from the numerically calculated transconductance $\mathrm{d}G/\mathrm{d}V_{SG}$ as shown by the red and black arrows in **b**, ΔV_{SG} = 0.256 V and 0.126 V respectively. Therefore, an out-of-plane and in-plane g-factor anisotropy of about two is inferred.

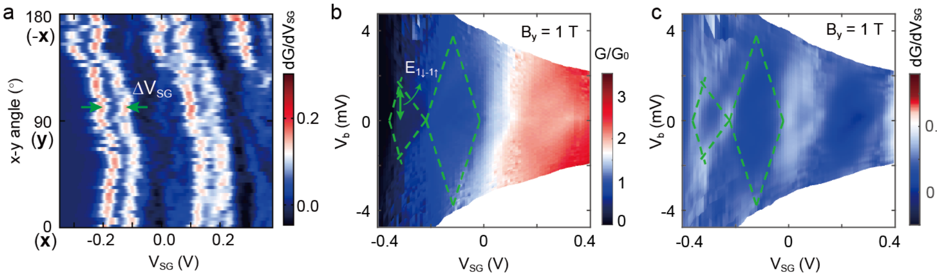

Figure 7.S5 – g-factors in B_y (in-plane but perpendicular to current flow) for the etch-defined QPC in the main text. Figure 7.5 in the main text shows the bias spectroscopy of the QPC transconductance in B_x and B_z, from which anisotropic g-factors are extracted. As shown in Fig. 7.4d in the main text, the roughly constant width of the 0.5 plateau when the magnetic field is rotated in the $z - y$ plane implies an isotropic in-plane g-factor. This figure shows **a** the numerical transconductance of Fig. 7.4d in the main text, **b** bias spectroscopy with B_y = 1 T and **c** its numerical transconductance. The high $\mathrm{d}G/\mathrm{d}V_{SG}$ in **a** (red color) represents transitions between conductance plateaus and the green arrow illustrates the width of the 0.5 plateau ΔV_{SG}, which is roughly constant. The energy separation $E_{1\downarrow-1\uparrow} \approx$ 1.6 meV is small (indicated by the green dashed and solid lines in **b** as it is limited by the low maximal field for the y component of the vector magnet. This lead to a relatively large uncertainty. Still, from $E_{1\downarrow-1\uparrow} = |g_{1,y}|\mu_B B$, we find $|g_{1,y}| \approx 28$, close to $|g_{1,x}| \approx 26$ as shown in the main text.

8

Spin-orbit interaction in a dual gated InAs/GaSb quantum well

We investigate the spin-orbit interaction in a dual gated InAs/GaSb quantum well. Using an electric field, the quantum well can be tuned between a single-carrier regime with exclusively electrons as carriers, and a two-carrier regime where electrons and holes coexist. The spin-orbit interaction in both regimes manifests itself as a beating in the Shubnikov–de Haas oscillations. In the single-carrier regime, the linear Dresselhaus strength is characterized by $\beta = 28.5\,\mathrm{meV\,Å}$, and the Rashba coefficient α can be tuned from 75 to 53 meV Å by changing the electric field. In the two-carrier regime, a quenching of the spin splitting is observed and attributed to a crossing of spin bands.

This chapter is based on A. J. A Beukman, F. K. de Vries, J. van Veen, R. Skolasinski, M. Wimmer, F. Qu, D. T. de Vries, B-M. Nguyen, W. Yi, A. A. Kiselev, M. Sokolich, M. J. Manfra, F. Nichele, C. M. Marcus and L. P. Kouwenhoven, Spin-orbit interaction in a dual gated InAs/GaSb quantum well *Physical Review B* **96**, 241401(R) (2017).

8.1. Introduction

The semiconductors InAs and GaSb have small band gaps together with a crystal inversion asymmetry resulting from their zinc-blende structure. These materials are therefore predicted to have strong spin-orbit interaction (SOI) [192, 199] which has been measured experimentally [185]. Moreover, tuning of the Rashba strength by electrostatic gating has been shown for InAs quantum wells [200, 201]. Strong and *in-situ* control over the SOI is a promising route towards novel spintronic devices [164, 199, 202], and a strong SOI together with a large g-factor and induced superconductivity are ingredients for a topological superconducting phase [24].

Combining InAs and GaSb in a quantum well gained much interest because of the type-II broken-gap band alignment [203]. As a result, the GaSb valence band maximum is higher in energy than the InAs conduction band minimum, opening a range of energies where electrons in the InAs coexist with holes in the GaSb. The spatial separation of these electron and hole gases allows for tunability of the band alignment using an electric field. Therefore, a rich phase diagram can be mapped out using dual gated devices [204, 205]. Although spatially separated, strong coupling between the materials allows for electron-hole hybridization which opens a gap in the energy spectrum when the electron and hole densities are equal [206, 207], driving the band structure topologically nontrivial [204].

Interestingly, the magnitude of this hybridization gap is spin-dependent due to the SOI [208–210]. Therefore, a spin-polarized state is seen at energies close to the hybridization gap [211], and at higher energies a dip in the spin splitting is expected [212]. The latter has yet to be observed and indicates a competition between electron-hole hybridization and the spin-orbit interaction. Here, we experimentally study SOI through the difference in density of the spin-orbit split bands of an InAs/GaSb quantum well. This zero-field density difference (Δn_{ZF}) is extracted from magnetoresistance measurements. First, the SOI is investigated in the regime where the GaSb is depleted from carriers. Rashba and Dresselhaus SOI strengths can be extracted from measurements of Δn_{ZF}. Second, SOI is investigated just above the hybridization gap where Δn_{ZF} almost vanishes, consistent with band-structure calculations.

8.2. Experimental setup

A 20-μm-wide and 80-μm-long Hall bar device is defined using chemical wet etching. A top gate is separated from the mesa by a 80-nm-thick $\mathrm{SiN_x}$ dielectric layer. The Hall bar is fabricated from the same wafer used in Refs. 205, 213. The quantum well consists of 12.5 nm InAs and 5 nm GaSb between 50 nm AlSb barriers. The doped GaSb substrate acts as a back gate. All measurements are done at 300 mK using standard lock-in techniques with an excitation current of 50 nA.

Figure 8.1 presents the longitudinal resistance of the Hall bar device as a function of top gate voltage V_{tg} and back gate voltage V_{bg}. The measurement is performed in a 2 T perpendicular magnetic field and therefore shows quantum oscillations resulting from the changing electron density. Quantum oscillations corresponding to holes are less pronounced as the mobility of holes in this system is much lower than

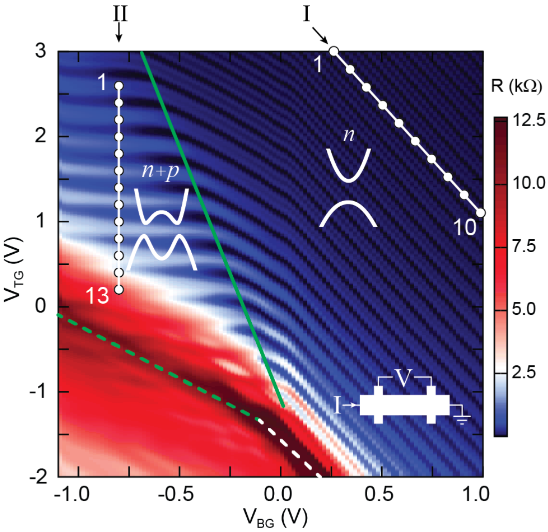

Figure 8.1 – Resistance map of the Hall bar device. Longitudinal resistance of the Hall bar device (see bottom right inset) as a function of top gate voltage (V_{tg}) and back gate voltage (V_{bg}) at 2 T out-of-plane magnetic field. Oscillations in resistance originate from Landau levels and denote lines of constant electron density. The dashed green and white lines indicate regions with the Fermi level located inside an energy gap. The solid green line separates the region with electrons as carriers (right) from a region where electrons and holes coexist (left). Line I is situated in the electron regime and Line II in the two-carrier regime. The insets show the schematic band alignment for both cases.

the mobility of electrons [205]. For lines parallel to these oscillations, such as line I in Fig. 1(a), the electron density is constant while the electric field changes. Regions of high resistance, indicated by the dashed white and green lines, correspond to having the Fermi level inside an energy gap. A detailed description of the phase diagram obtained from measurements on the same wafer was reported by Qu et al. [205].

The green solid line in Fig. 8.1 divides the phase diagram into two regimes. To the right-hand side of this line is the electron-only regime, where the GaSb is depleted. The system effectively is an asymmetric InAs quantum well with a trivial band alignment and the Fermi level residing in the conduction band (see the inset of Fig. 8.1). In this regime we investigate Δn_{ZF} along line I, where the electron mobility is highest while only the lowest subband remains occupied. The regime to the left of the green line is the two-carrier regime where electrons and holes coexist. Line II is chosen to evaluate Δn_{ZF} close to the hybridization gap (highlighted by the dashed green line). Before discussing the spin-orbit interaction in the two-carrier regime (along line II), we first study the electron-only regime (line I).

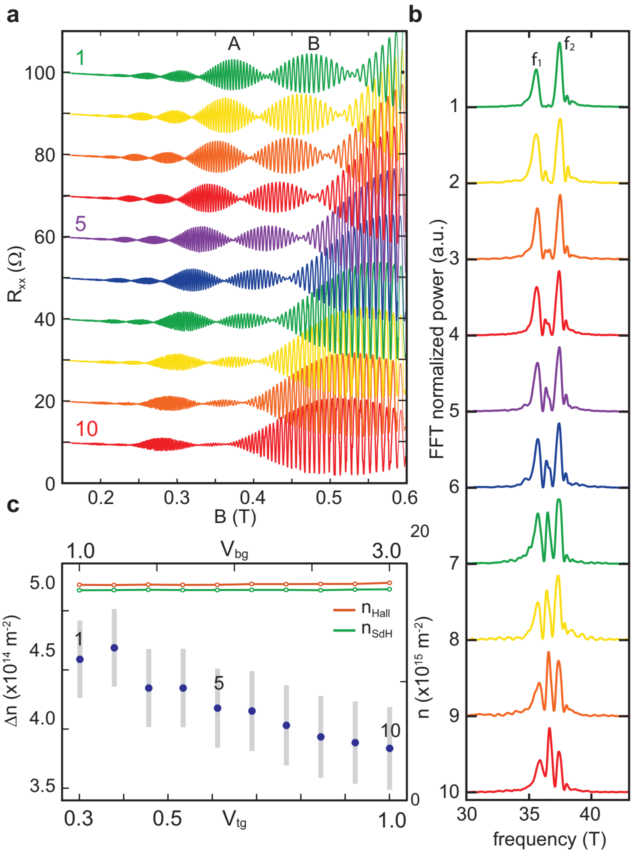

Figure 8.2 – **Spin splitting at a constant electron density in the electron regime.** **a** Magnetoresistance traces for data points 1-10 along line I indicated in Fig. 8.1, a constant background is subtracted from the traces and they are offset 10 Ω from each other. **b** Fourier power spectra $|\mathcal{F}[R_{xx}(1/B)]|^2$ of the traces in **a**. **c** Electron density extracted from Hall resistance and Shubnikov-de Haas period (right axis) together with the Δn_{ZF} at each data point along line I (left axis), with error bars in gray.

8.3. Results

8.3.1. Electron regime

Figure 8.2a shows magnetoresistance traces for 10 points along line I. The density of electrons is fixed (see Fig. 8.2c) while the electric field is changed. We first consider trace 1. Clear oscillations in the longitudinal resistance R_{xx} are observed as a function of perpendicular magnetic field B modulated by a beat pattern. These Shubnikov-de Haas (SdH) oscillations appear for each single-spin band and are periodic in $1/B$ with a frequency that relates to the carrier density via $n = e/h \cdot f$ [185, 214]. The beat modulation observed in trace 1 is caused by two slightly different SdH frequencies f_1, f_2. This is also evident from the fast Fourier transform (FFT) of the magnetoresistance trace $\mathcal{F}[R_{xx}(1/B)]$ presented in the first curve of

Fig. 8.2b (see Supplemental Material for details on the Fourier procedure Sec. 8.5). These two SdH frequencies indicate two distinct densities n_1, n_2. They must correspond to different spin species because their sum $n_1 + n_2$ equals the Hall density n_H (see Fig. 8.2c). Subsequently, one spin species has a larger density than the other, $n_1 > n_2$, implying that the system favors one spin-orbit eigenstate over to the other. The difference, $\Delta n_{ZF} = n_2 - n_1$, is a measure for the zero-field spin splitting energy, $\Delta E_{\mathrm{ZFSS}} = \Delta n_{ZF} \left(m^*/\pi\hbar^2\right)^{-1}$.

Upon moving from point 1 to 10 along line I, two trends are observed. First, an extra frequency peak emerges in the FFTs at $(f_1 + f_2)/2$. This originates from the asymmetry between adjacent beats in the SdH oscillations, visible both in amplitude and number of oscillations of beats A and B in Fig. 8.2a and Fig. 8.S1. Second, the spacing between the outer peaks in the FFT spectrum decreases, as is evident from the decreasing Δn_{ZF} over line I (Fig. 8.2c). This arises from an increasing number of oscillations in both beats A and B (Fig. 8.S1), which also pushes the beat nodes to lower magnetic fields. Before we extract the actual SOI strengths and show its electric field dependence, we first elucidate the origin of the emerging center frequency peak.

The center frequency, interestingly, does not correspond to an actual density. The sum of the densities n_1 and n_2 (corresponding to the outer peaks in the FFT) still equals the Hall density. There are, however, mechanisms involving scattering between Fermi surfaces that can result in extra frequency components. Such mechanisms are magnetic inter-subband scattering (MIS) [215, 216], magnetophonon resonances (MPR) [217, 218], and magnetic breakdown (MB) [219–221].

We exclude MIS and MPR. By changing electron density all the frequency peak positions shift with equal strength (Fig. 8.S2). However, the oscillation frequency of MIS and MPR is determined by the subband spacing and a specific phonon frequency, respectively. Both do not depend on the electron density. In contrast, for MB the spurious peak always appears in between f_1 and f_2. The MB mechanism explains this spurious central peak as carriers tunneling between spin-polarized Fermi surfaces at spin-degeneracy points. The interplay of Dresselhaus and Rashba SOIs in our heterostructure could lead to such an anisotropic Fermi surface [219, 222]. In order to confirm this hypothesis, we extract the individual Rashba and Dresselhaus contributions by comparing our data to quantum mechanical Landau level simulations that include the MB mechanism.

8.3.2. Landau level simulations

The quantum well in the electron-only regime is modeled by a Hamiltonian for a two-dimensional (2D) electron system with spin-orbit interaction subject to a perpendicular magnetic field B_z, as given by [192, 199]:

$$\begin{aligned} H = \frac{(\hat{p}_x^2 + \hat{p}_y^2)}{2m^*}\sigma_0 + \alpha(\hat{p}_y\sigma_x - \hat{p}_x\sigma_y)/\hbar + \beta(\hat{p}_x\sigma_x - \hat{p}_y\sigma_y)/\hbar \\ +\gamma(\hat{p}_y\hat{p}_x\hat{p}_y\sigma_x - \hat{p}_x\hat{p}_y\hat{p}_x\sigma_y)/\hbar^3 + \frac{1}{2}g\mu_B B_z\sigma_z. \end{aligned} \tag{8.1}$$

Where $p_i \rightarrow p_i + eA_i$ is the canonical momentum, σ_i the Pauli spin matrices, α, β, γ the Rashba, linear Dresselhaus, and cubic Dresselhaus coefficients, respectively, $\hbar$ the reduced Planck's constant, and μ_B the Bohr magneton. An electron effective mass m^* of $0.04m_0$ is measured from the temperature dependence of the SdH oscillations (Fig. 8.S3) and a g-factor of -11.5 is used in the calculations[1] [223]. We solve for the Landau level energies in a perpendicular magnetic field, and extract the resistivity as a function of magnetic field (for details see Supplemental Material Sec. 8.5).

The parameters α, β, γ in the model are estimated and fine tuned to match the node positions and the number of oscillations in a beat of the measured SdH traces. Figures 8.3a and 8.3b show the measured SdH data together with the simulated data for traces 1 and 10. Trace 1 is fitted with $\alpha_1 = 75$ meVÅ, $\beta_1 = 28.5$ meVÅ, $\gamma_1 = 0$ meVÅ^3, and trace 10 with $\alpha_{10} = 53$ meVÅ , $\beta_{10} = 28.5$ meVÅ, $\gamma_{10} = 0$ meVÅ^3. The node positions and amplitude modulation of the simulated data agrees well with the measured SdH oscillations.

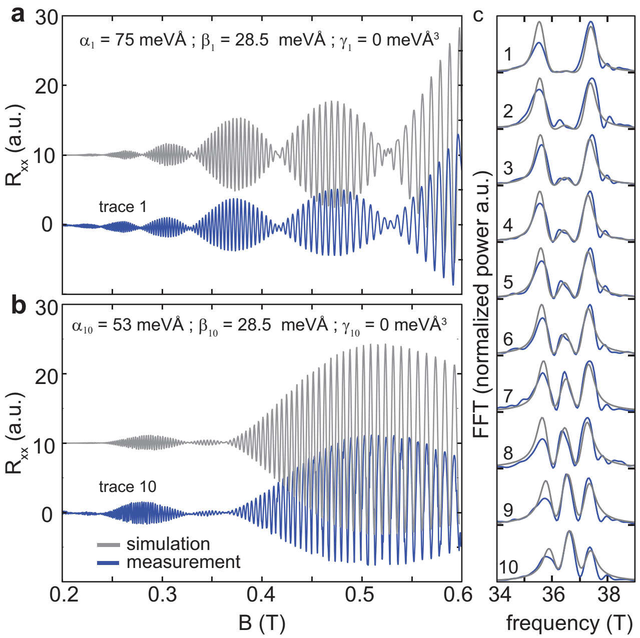

Figure 8.3 – Landau level simulations for a 2DEG with Rashba and Dresselhaus spin-orbit interactions. a and **b** depict the measured trace (blue) together with the simulated magnetoresistance trace (gray) which is offset by ten units. The values for α, β, and γ used are mentioned in the Figure. In all simulations, the Landau level broadening is set to $\Gamma = 0.45$ meV. **c** Fast Fourier transform of the simulated and measured magnetoresistance at points 1-10 along line I. All simulated magnetoresistance traces can be found in the Supplemental Material Fig. 8.S4.

---

[1] Note that this g-factor value of -11.5 is measured on a slightly different stack with an InAs layer of 11 nm thick. We have checked in the simulations that changing the g-factor to -5 or -15 has negligible influence on the SdH oscillations.

Curiously, only good fits are obtained when setting the cubic Dresselhaus term γ to zero. In 2D systems, β is related to γ via $\beta = \langle k_z^2 \rangle \gamma$, where $\langle k_z^2 \rangle \approx (\pi/d)^2$ is the expectation value of the transverse momentum [192, 199] in a quantum well of thickness d. So γ should be non-zero. Currently, we do not understand this discrepancy. A recent experimental study on a similar material system also found that the cubic Dresselhaus term could be neglected [224].

Now, we consider all traces (1-10) and show that the two trends of Fig. 8.2 (emerging center FFT peak and approaching outer FFT peaks) are reproduced by changing only the Rashba SOI strength. Figure 8.3c shows the FFTs of the simulated traces where α is linearly interpolated between α_1 and α_{10} while fixing $\beta = 28.5$ meVÅ and $\gamma = 0$ meVÅ^3. Linear interpolation is used because the electric field changes linearly along line I, and Rashba SOI strength depends linearly on electric field [192, 225, 226]. All simulated FFTs and the SdH traces (Fig. 8.S4) match the measured data very well, clearly reproducing the emerging central peak and the approaching outer peaks.

8.3.3. Two-carrier regime

In the remainder of this chapter, we switch to the two-carrier regime, located left of the solid green line in Fig. 8.1. Electrons in InAs are present alongside with holes in GaSb ($n + p$). Here, we study the influence of the hybridization between electrons with holes on Δn_{ZF} by investigating magnetoresistance traces on the points 1-13 along line II.

Before continuing with the measured magnetoresistance traces, it is insightful to examine the expected band structures at points 1 and 13, as illustrated in Fig. 8.4b. The first point of line II is located near the boundary between the two-carrier and single carrier regimes. A small amount of holes with a large amount of electrons is present. At point 13, close to the hybridization gap, the electron and hole densities are roughly equal, hence the Fermi level E_F is close to the hybridization gap. Note also that k_{cross} decreases from 1 to 13, since the electric field changes.

Figure 8.4a shows the magnetoresistance traces 1-13 along line II. Starting from trace 1 towards trace 13, we find series of traces with or without beating, depicted in blue and red, respectively. For traces 1-3, at large electron density, beating is observed from which we extract[2] $\Delta n_{ZF} = 1.7 \cdot 10^{14}$ m^{-2}. Remarkably, traces 4 and 5 do not show any beating, therefore no zero-field density difference can be extracted. For traces 6-10, the beating revives, showing strong beating. Finally, traces 11-13 show no beating. Figure 8.4c depicts the extracted Δn_{ZF} along line II, which shows a nonmonotonic behavior as a function of gate voltage along line II.

In order to understand this nonmonotonic Δn_{ZF} near the hybridization gap (points 1-10), we performed band structure calculations of our InAs/GaSb quantum well. The Δn extracted from these calculations is plotted in Fig. 8.4d, which qualitatively agree with the observed dip in Δn_{ZF} at points 4 and 5 (Fig. 8.4c). In order to understand the simulated Δn, the band structure near the hybridization gap is depicted in the inset of Fig. 8.4d (the zoom-in on Fig. 8.4b indicated by the

---

[2] We cannot directly extract the spin-orbit strength from this Δn by comparing to the single-carrier case, since the effective mass in this region is unknown.

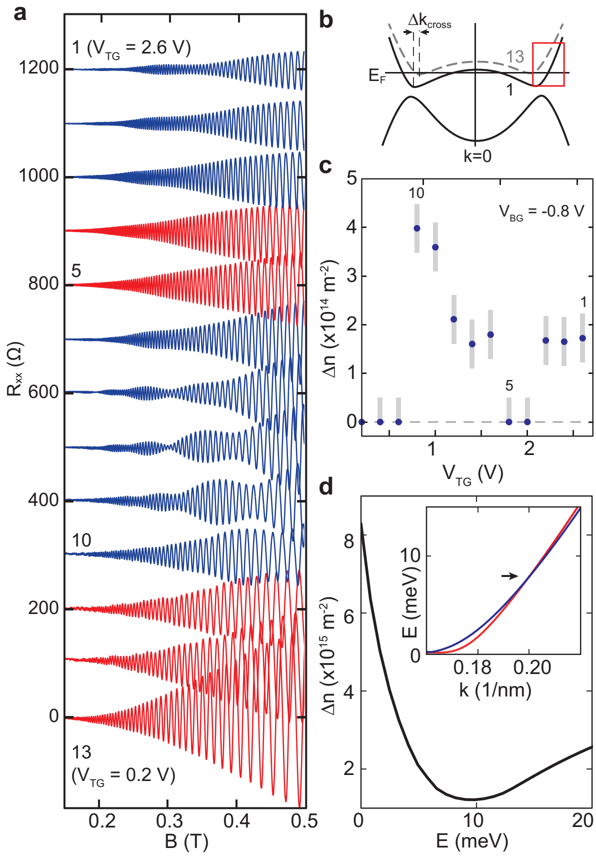

Figure 8.4 – **Spin-splitting in the two-carrier regime.** **a** Magnetoresistance traces for points 1 to 13 along line II indicated in Fig. 1. For each trace the $R_{xx}(B = 0)$ background resistance is subtracted and afterwards the traces are offset by 100 Ω. Beating is (not) observed for (red) blue colored traces. **b** Schematic band structure tuning when moving from point 1 to 13. **c** Δn_{ZF} extracted from the Fourier transform of magnetoresistance traces (see Fig. 8.S5) of **a**. Error bars are indicated by the light blue bar. **d** Δn_{ZF} extracted from band structure calculation for our InAs/GaSb quantum well at zero electric field. The inset shows the corresponding band structure in the [100] direction.

red box). The blue and red lines represent different spin bands. The bands cross at the black arrow, indicating the vanishing of Δn, such as observed in the experiment. We found this feature to be robust for different electric fields and crystal directions, see Fig. 8.S6. Interestingly, the crossing of spin bands implies a sign change in SOI strength. Opposite signs of SOI can thus be reached by adjusting the chemical potential. Usually, electric fields are applied to reach such a sign change [227].

Note that only a qualitative comparison between experiment and calculations is possible as only the Fermi energy is varied in the simulation, while in the experiment the band structure (k_{cross}) and Fermi energy are expected to change. The fact that Δn_{ZF} in Fig. 8.4d does not completely vanish is because the crossing of the spin bands in the [110] occurs at a slightly different energy than in the [100] direction.

The lack of beating of traces 11-13 is not captured with the simulation. There are two possible reasons for this deviation. First, a strong asymmetry in SdH amplitudes of the two spin species ($A_{\mathrm{up}} \gg A_{\mathrm{down}}$) determines the visibility of the beating pattern. The single spin band SdH oscillation amplitude depends on effective mass m^* and scattering time according to $A_{\mathrm{SdH}} \sim (eB/m^*)^3 \exp(-\pi/\omega_c\tau)$ [228]. Both the effective mass and scattering time for the two spin bands become very dissimilar when approaching the hybridization gap (Fig. 8.S7), resulting in a reduced visibility below the experimentally detectable value. Second, Nichele et al. [211] shows there is an energy window with only one single spin band present. In such a spin-polarized state no beating can occur. Here, we cannot discriminate between these two reasons that explain the lack of beating in traces 11-13.

8.4. Conclusions

In conclusion, we presented a study of the spin-orbit interaction in an InAs/GaSb double quantum well. The Fermi level and band structure are altered by top and bottom gates. In the electron-only regime, we find an electric field tunable spin-orbit interaction, and extract the individual Rashba and Dresselhaus terms. In the two-carrier regime, we observe a nonmonotonic behavior of the spin splitting which we trace back to the crossing of the spin bands due to the hybridization of electrons and holes.

8.5. Supplemental Material

8.5.1. Supplementary Figures

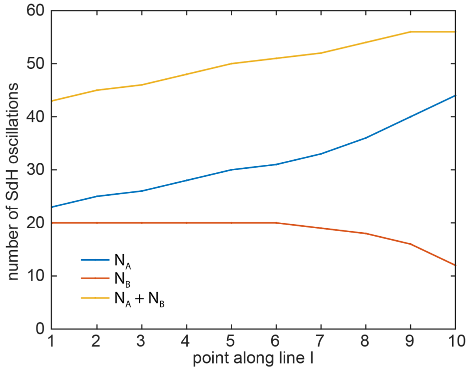

Figure 8.S1 – Number of oscillations in a beat. Number of SdH oscillations in beat A (N_A), beat B (N_B) and the sum (N_A+N_B) for each trace in Fig. 2a of the main text. The two trends discussed in the main text are clearly visible here. First, moving from point 1 to 10 the asymmetry $r = (N_A - N_B)/(N_A + N_B)$ increases. Second, the total number of oscillations $N_A + N_B$ increases.

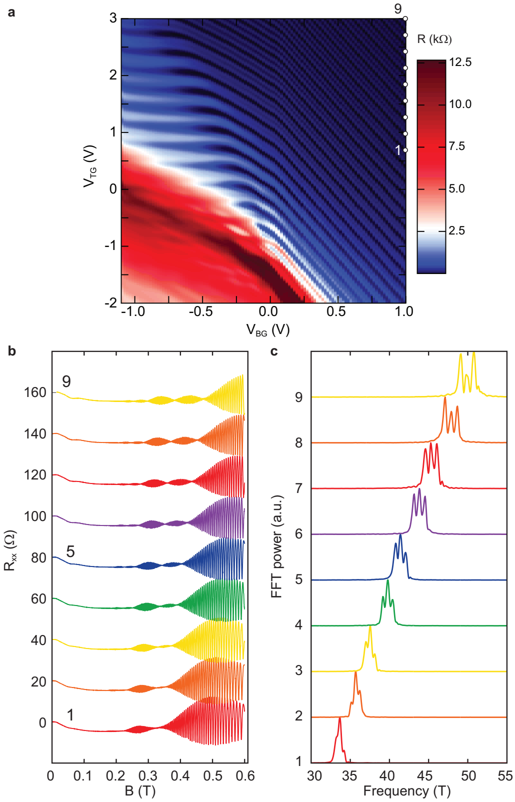

Figure 8.S2 – Peaks shift upon changing electron density. **a** Phase diagram of the InAs/GaSb quantum well at $B_{\mathrm{perp}} = 2$ T showing 9 additional data points. Moving from point 1 to 9 several SdH oscillations are crossed, hence the electron density increases from point 1 to 9. **b** Magnetoresistance traces $R_{xx}(B)$ for points 1 to 9. Traces are offset by 20 Ω. **c** Fourier transforms of the traces in **b**, showing that the center frequency shifts together with the outer frequency peaks. This density dependence of the central frequency peak excludes MIS and MPR.

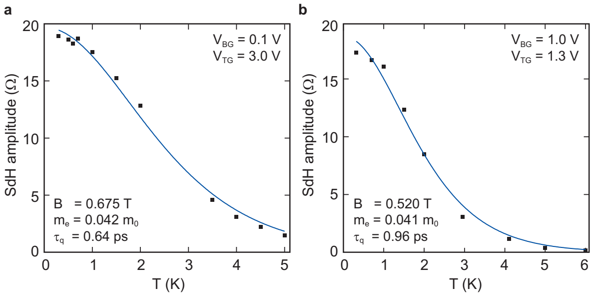

Figure 8.S3 – Dingle plot to determine the effective mass. **a, b** Temperature dependence of the SdH oscillations (Dingle plots) measured at point 1 and 10 on line I, respectively. Effective mass m^*, indicated in the Figures, is extracted by fitting these data to the Dingle formula (blue curve).

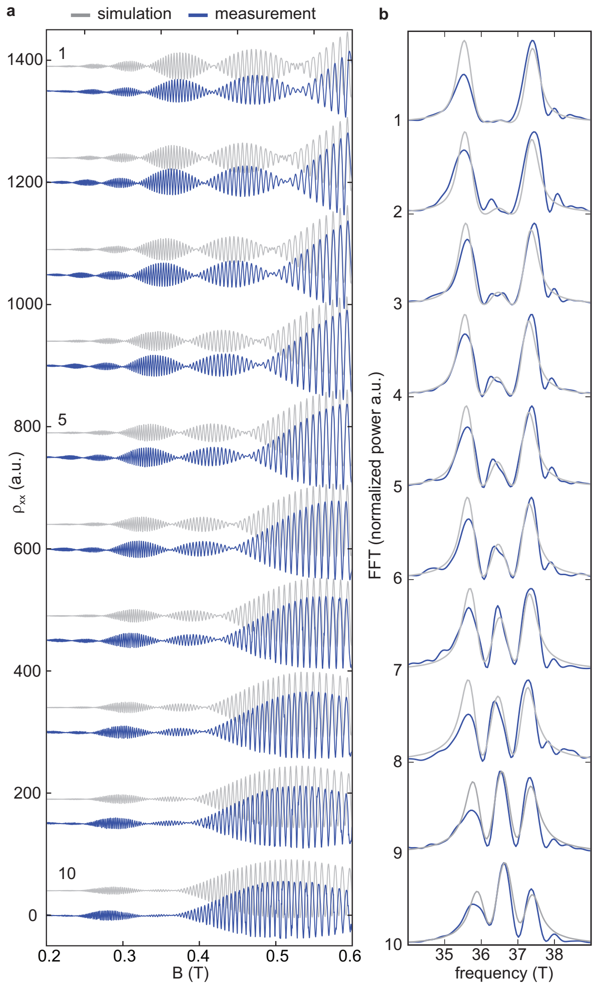

Figure 8.S4 – SdH traces of the Landau level simulations. a Measured magnetoresistance traces (blue) for points 1-10 along line I together with the simulated traces (gray). The simulated traces are offset 40 a.u. from the measured traces; the measured traces are offset by 150 a.u. from each other. The value of Rashba spin-orbit interaction strength α is linearly changed from 73 to 53 meVÅ going from trace 1 to 10. The linear and cubic Dresselhaus interaction strength are kept constant at $\beta = 28.5$ meVÅ and $\gamma = 0$ meVÅ^3. **b** Corresponding Fourier transforms of the measured traces (blue) and simulated traces (gray), i.e. a reproduction of Fig 8.3c.

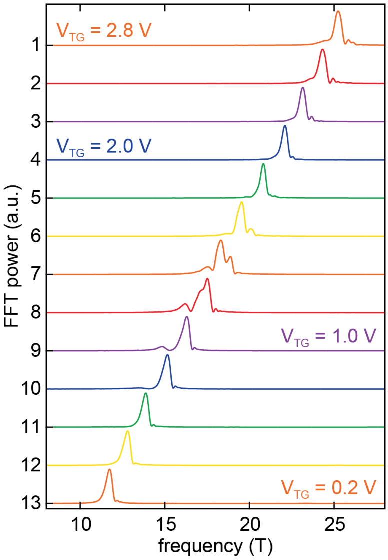

Figure 8.S5 – **Fourier transforms for the 13 points along line II in the two-carrier regime.** All traces are normalized such that the maximum is set to 0.8 a.u.

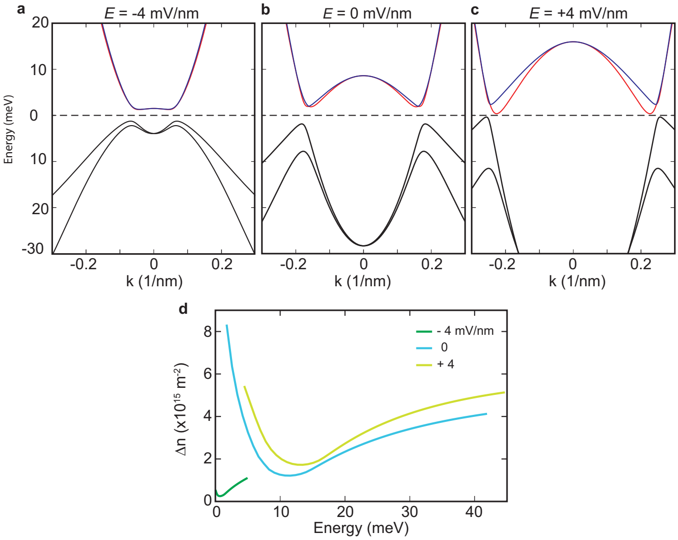

Figure 8.S6 – **Band structure calculations for multiple electric fields. a-c** Result of band structure calculations along [100] for electric fields $\vec{E} = -4$ mV/nm, 0 mV/nm and +4 mV/nm, respectively. The spin-split bands of the conduction band are colored red and blue for clarity. **d** The ZFSS extracted from these band structures. For all electric fields a minimum in spin-splitting is found, making this a robust feature of the inverted band structure.

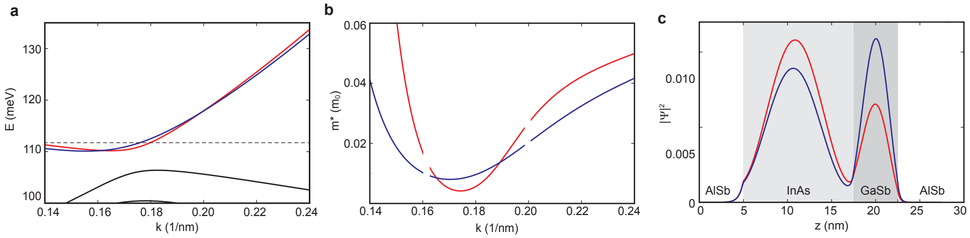

Figure 8.S7 – **Effective mass and wave function in the quantum well a** Zoom-in on the calculated band structure (at $\vec{E} = 0$) close to the hybridization gap. Red and blue correspond to different spin species. **b** Effective mass calculated from $m^* = \hbar^2 \left(\partial^2 E/\partial k^2\right)^{-1}$. The effective mass around $k = 0.16$ nm^{-1} and $k = 0.20$ nm^{-1} is omitted due to numerical artifacts. **c** Simulated normalized wave functions at the energy indicated by the dashed line in **a**. It is clear that the distribution of the wave function is spin dependent, which could result in a spin dependent scattering.

8.5.2. Fourier Transforms

The Fourier transforms in this manuscript are obtained using the following method. Starting from a magnetoresistance curve, first a magnetic field range is chosen. The lower bound is fixed at 0.15 T. The upper bound is chosen such that the interval ends at 40% of a beat maximum. Truncating the signal in this way causes minimal deviation from the true frequency components. Next, the background resistance is estimated using a 6th order polynomial fit, which subsequently is subtracted from the signal. The remaining signal is interpolated on a uniform grid in $1/B$ and padded with zeros on both sides. No extra window function is applied. A fast Fourier transform converts the signal to the frequency domain $R(\omega)$ and the power spectrum is obtained using $P(\omega) = R(\omega) \times R^*(\omega)$. All Fourier transforms are normalized such that the maximum is 0.8 a.u.

8.5.3. Details on the Landau level simulation

This section describes the calculations used to simulate the magnetoresistance traces to extract the Rashba and Dresselhaus coefficients as shown in Fig. 3a of the main text. We closely follow the method presented in Ref. 228 and Ch. 4 of Ref. 192.

For convenience, we repeat the Hamiltonian presented in Eq. 1 of the main text:

$$\begin{aligned} H = \frac{(\hat{p}_x^2 + \hat{p}_y^2)}{2m^*}\sigma_0 + \alpha(\hat{p}_y\sigma_x - \hat{p}_x\sigma_y)/\hbar + \beta(\hat{p}_x\sigma_x - \hat{p}_y\sigma_y)/\hbar \\ +\gamma(\hat{p}_y\hat{p}_x\hat{p}_y\sigma_x - \hat{p}_x\hat{p}_y\hat{p}_x\sigma_y)/\hbar^3 + \frac{1}{2}g\mu_B B_z\sigma_z. \end{aligned} \tag{8.S1}$$

For the perpendicular magnetic field $B = (0, 0, B_z)$, the symmetric gauge $\mathbf{A}(x, y) = \frac{B_z}{2}(-y, x, 0)$ is used. The canonical momentum can be written as

$$\hat{p} = -i\hbar\nabla + e\mathbf{A}. \tag{8.S2}$$

Raising and lowering operators are defined as

$$\begin{aligned} a^\dagger &= \frac{\lambda_c}{\sqrt{2}\hbar}\left(\hat{p}_x + i\hat{p}_y\right), \\ a &= \frac{\lambda_c}{\sqrt{2}\hbar}\left(\hat{p}_x - i\hat{p}_y\right), \end{aligned} \tag{8.S3}$$

where $\lambda_c = \sqrt{\hbar/eB}$ is the magnetic length. The raising operators act on the Landau levels, i.e. $a^\dagger|n,\uparrow\rangle = \sqrt{n+1}\,|n{+}1,\uparrow\rangle$. The momentum operators are rewritten in the raising and lowering operators, which are then substituted into the Hamiltonian. We take a basis of $N = 400$ Landau levels in order to capture magnetic fields $\gtrsim 0.1$ T for the electron density $n_s \simeq 17.6 \cdot 10^{15}$ m^{-2}. Solving the Hamiltonian results in the Landau level energies at a particular magnetic field $E(n, B_z)$.

Following Luo et al. [228] the conductance is written as:

$$\sigma_{xx} = \frac{e^2}{\pi^2\hbar}\sum_{n,\uparrow\downarrow}\left(n \pm \frac{1}{2}\right)\exp\left(-\frac{(E_F - E_{n,\uparrow\downarrow})^2}{\Gamma^2}\right). \tag{8.S4}$$

We assume a fixed Fermi energy at $E_F = (\pi\hbar^2 n_s)/m^*$. To obtain the resistivity we use the approximation that for quantizing magnetic fields $\sigma_{xy}^2 \gg \sigma_{xx}^2$ so that the transverse resistivity ρ_{xx} is given by [228]:

$$\rho_{xx} = \sigma_{xx}/(\sigma_{xy}^2 + \sigma_{xx}^2) \approx \sigma_{xx}/\sigma_{xy}^2 \approx \sigma_{xx}\left(B_z/en_s\right)^2 \tag{8.S5}$$

9

Outlook

Build a rocket boys!

Elbow

The experiments presented in this thesis are related to various components of the Majorana box qubit (MBQ). We developed superconducting islands (SC) and gate-based readout in proximitized InAs nanowires, and characterized InSb and InAs/GaSb 2D electron gases (2DEGs) which might be used for realizing topological superconducting networks.

In this chapter, we propose a series of experiments that further work towards realizing a MBQ, using the results presented in this thesis. The first experiment aims at distinguishing Majorana zero modes (MZMs) from quasi-Majoranas. Quasi-Majoranas are zero energy states which occur in proximitized, spin-orbit coupled nanowires in a magnetic field near a smooth potential [67, 229, 230]. They can mimic Majorana signatures such as quantized zero bias conductance, the fractional Josephson effect, and the hybridization between a quantum dot (QD) and a MZM; and may even be used to demonstrate non-Abelian statistics [67, 230]. However, they are at best partially separated in space, and hence, not immune to local perturbations. The second experiment probes the cotunneling through a Majorana island. This process is central for MBQ readout, and can already be investigated in a single nanowire. Finally, we propose to measure Majorana parity fluctuations as an initial experiment for the MBQ itself. However, before we dive into these experiments, we start with a discussion on the available material platforms.

9.1. Materials

For the experiments in this thesis, various material systems have been used. It is interesting to compare these systems among themselves and alternatives for two reasons: one, other materials might have favourable properties to induce a topological state, and two; ultimately, a nanowire network is necessary to construct a MBQ.

For the first aspect, we restrict the discussion to vapour-liquid-solid (VLS) nanowires. Here, InSb nanowires are an interesting alternative for InAs nanowires. Compared to InAs, InSb has a larger g-factor (8-15 for InAs versus 40-50 for InSb [25]) which lowers the required magnetic field to drive the wire into the topological regime. Also, the electron mobility in InSb is larger than in InAs which might prevent unwanted quantum dots in the tunnel barriers. This hypothesis is supported by the observation of quantized conductance and ballistic Majorana signatures in InSb wires [188, 231]. In addition, quantized zero bias conductance peaks have been observed in InSb wires proximitized with an aluminium shell [36]. On the other hand, nanofabrication might be more difficult on InSb, because its maximum allowed processing temperature is lower. As such, fabrication recipes cannot be directly transferred from InAs to InSb. We mainly expect difficulties for the deposition of the AlO_x layer as it occurs at elevated temperature. Besides, the selectivity for the aluminium etch might be different for the two materials.

Going forward, nanowire networks need to be developed. These networks can be defined both with top-down as with bottom-up methods. In the top-down methods, one starts with a 2D system and defines the desired structure via either gating or etching. This approach has been investigated in this thesis, and has the advantage that one can start with a clean, high mobility system as evidenced by the quantized conductance observed in Chapter 7, and low-onset field for the Shubnikov-de Haas oscillations reported in Chapter 8. Between InSb and (the electron system in) InAs/GaSb[1], the former seems a more promising platform for topological networks, because InAs/GaSb is difficult to gate due to the proximity of the hole band [205], and accumulates electrons at edges defined through etching [232]. Recently, induced superconductivity in an InSb 2DEG has been reported together with the observation of a π-junction in a parallel magnetic field, indicating significant progress towards creating a topological state [233]. Besides InSb, InAs-Al 2DEGs are interesting candidates for the top-down approach [234]. In this system, initial MZM signatures have already been demonstrated [235]. In the bottom-up approach, the network is defined when the crystal is grown, using, for example, selective area growth (SAG) [174, 236], or directed nanowire growth [172]. In this approach, no additional gates (or etching steps) are needed to define the 1D structures. However, the mobility in these structures is lower than for the 2D systems. Here, we note that it is not clear to what extent the high mobility of the 2D systems drops once 1D structures are defined.

To summarize, there are multiple routes to realize nanowire networks, and more research is needed to determine which one is most suitable for MBQs. An important aspect relates to yield, including both the yield for basic device operation such as working gates and contacts; as the yield with which the device can be tuned into the topological phase. At the moment, the shortest route for realizing a MBQ seems to be using InAs-Al 2DEGs. Signatures of MZM have already been observed in this platform (as mentioned above). Moreover, a recent study reports measurement of a superconducting island embedded in an Aharonov-Bohm loop, showing the applicability of this platform for creating complicated devices [237]. For the two wire experiments discussed below, we recommend using InSb nanowires for the better prospect in reaching the topological regime.

9.2. Current-phase relation of a SCPT

In Chapter 4, we studied the gate-charge modulation of the switching current of a single-Cooper-pair transistor (SCPT) as a function of parallel magnetic field. In this section, we propose to extend these measurements, and record the full current-phase relation (CPR) of the SCPT. This allows to distinguish a zero energy state (indicated by a $1e$-period modulation) due to Majoranas from a state due to quasi-Majoranas [238, 239].

9

Figures 9.1a and b explain the experiment in more detail. For the Majorana case, a Cooper-pair can be transferred from the left to right lead by coupling to both MZMs. First, the pair tunnels into the spatially-separated Majorana pair, after which it tunnels out of the same Majorana pair. The amplitude for this process scales with $\gamma_1^2\gamma_2^2 = 1$, and is thus independent of the Majorana parity. For quasi-Majoranas, on the other hand, a Cooper-pair in the left lead can tunnel into the island via the left quasi-Majoranas and out to the right lead via the right quasi-Majoranas. This process scales with $\gamma_1\gamma_2\gamma_3\gamma_4$, resulting in a parity-dependent sign

---

[1] Here, we do not consider the 2D topological insulator state in InAs/GaSb.

(or direction) of the supercurrent [238]. Hence, a measurement of the CPR of a SCPT as a function of gate-charge should be able to distinguish between Majoranas and quasi-Majoranas[2]. However, when the Cooper-pairs can only couple to one of the quasi-Majoranas, similar to the situation described in Ref. 230, we expect the same parity-insensitivity for quasi-Majoranas as for Majoranas. Still, the lack of a π-phase shift is a necessary condition for MZMs. Moreover, this experiment can exclude models for which both quasi-Majoranas couple to the lead.

To measure its CPR, the SCPT can be embedded in an asymmetric DC SQUID with the critical current of the reference junction much larger than the critical current of the SCPT (see Fig. 9.1c). In this case, the applied phase bias fully drops across the SCPT, and the CPR is directly measured by an I_{sw} versus phase scan. Typically, the switching current of the SCPT is 1-5 nA (see Chapter 4), requiring a switching current through the reference arm larger than 50 nA. This condition can be met using, for example, nanowires or Al/AlO$_x$ junctions [240]. Nanowires have the advantage that they can be pinched-off, so that the SCPT can also be studied without the reference arm. The conventional aluminium junctions, on the other hand, have a well-known, sinusoidal CPR which allows for determining the exact CPR of the SCPT.

Alternatively, the CPR of the SQUID can be measured by embedding it in a LC tank circuit [105, 241], see Fig. 9.1d. In this case, the Josephson inductance of the SCPT, and hence the resonance frequency of the circuit, changes due to the phase modulation of the switching current. With this approach the full CPR can be measured in a single phase sweep and a short integration time, making it easier to explore the parameter space. Also, it enables using a RF SQUID design where the reference junction is replaced by a shunt inductor.

In this follow-up experiment, the gate design of the SCPT employed in Chapter 4 can be improved by using the top gate design of the devices used in Chapters 5 and 6. These top gates have smaller cross-talk compared to the side- and global back gates used in Chapter 4, making it easier to control the SCPT.

---

[2] When Cooper-pairs can only couple to one of the Majoranas (in the long wire limit), supercurrent can still flow through the SCPT if one quasiparticle is transferred through the continuum while the other is transferred via the MZMs [239]. In this case, the supercurrent is also parity-dependent. However, now the supercurrent is symmetric around the charge degeneracy points instead of asymmetric as for the quasi-Majorana case.

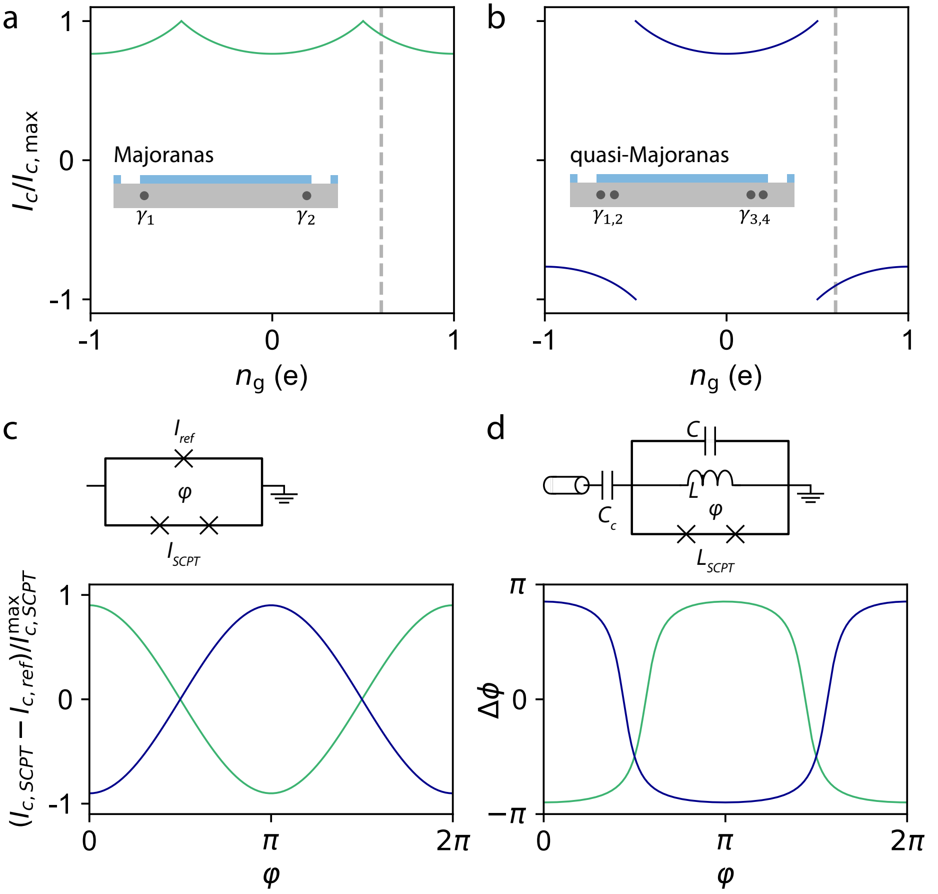

Figure 9.1 – Current-phase relation of a (quasi-)Majorana single-Cooper-pair transistor. a For Majoranas, the gate-charge modulation of the switching current is parity independent. Whereas for quasi-Majoranas **b**, there is a π-phase difference between the switching current of the different parity branches. **c** The current-phase relation (CPR) can be measured by embedding the single-Cooper-pair transistor (SCPT) in a DC SQUID. When $I_{c,ref} \gg I_{c,SCPT}$, the flux bias fully drops across the SCPT, and the flux modulation of the switching current is given by $I_{c,SCPT} - I_{c,ref} = I_{c,SCPT}^{\max} \cos(2\pi\Phi/\Phi_0)$. The lower panel of **c** shows this modulation for the Majorana (green) and the quasi-Majorana (blue) case at the gate-charge indicated by the dashed line in **a, b**. **d** The CPR can also be measured using RF reflectometry. The (flux dependent) Josephson inductance of the SCPT changes the resonance frequency of the LC tank circuit, and thereby imparts a phase shift on the reflected probe field. The lower panel of **d** shows the phase response of this circuit for the Majorana (green) and the quasi-Majorana (blue) case at the gate-charge indicated by the dashed line in **a, b**. For the simulation, we used $L = 600$ pH, $C = 100$ pF, $C_c = 5$ pF, and $I_{c,SCPT}^{\max} = 5$ nA, resulting in a bare resonance frequency of $f_0 \approx 630$ MHz. To fabricate the shunt inductor, the kinetic inductance of a NbTiN film could be used. For the shunt capacitor one could use a parallel plate geometry. Panels **a** and **b** are adapted from [238].

9.3. Double dot coupling through a Majorana island

In this section, we propose to measure the charge hybridization between two distant quantum dots through cotunneling via a Majorana island. With a conventional superconducting island, one expects that this coupling decays exponentially in the length of the SC. However, for a Majorana island, the QD hybridization is nearly length independent due to the non-local nature of the MZMs. We propose to measure this hybridization using gate-based sensing. From such an measurement, we could extract the attainable cotunnel coupling, which is an important figure of merit for MBQ readout. This experiment builds on the QD-SC experiment reported in Chapter 6, and is based on theoretical work described in Refs. 242, 243.

The eigenstates of a QD-SC-QD (see Fig. 9.2a) can be labelled with $|n_1, n_2, n_f, N\rangle$, with $n_{1,2}$ indicating the occupation of the QDs, n_f the occupation of the nonlocal fermionic state formed by the two MZMs, and N the number of Cooper-pairs on the island. For simplicity, we only consider states with an even number of particles in the combined system. In the odd Coulomb valley of the SC (e.g., around $n_g = 1$), the state of the SC is odd ($n_f = 1$ and $N = 0$), and the groundstate is a linear combination of $|0110\rangle$ and $|1010\rangle$. These states are coupled via second-order tunneling through the MZMs with $|1100\rangle$ and $|0001\rangle$ as the possible virtual states. The former, $|1100\rangle$, is reached by so-called normal tunneling where the particle in the nonlocal fermion tunnels to the empty QD. The latter, $|0001\rangle$, couples upon so-called anomalous tunneling where the particle in the nonlocal fermion condenses together with the particle in the QD into a Cooper-pair. The coupling between $|0110\rangle$ and $|1010\rangle$ remains finite in the whole odd Coulomb valley of the island, although it is suppressed by the charging energy $t \propto t_1 t_2 / E_C$, with $t_{1,2}$ the tunnel coupling from $\mathrm{QD}_{1,2}$ to $\gamma_{1,2}$. In addition, the hybridization between the dot is sensitive to the detuning, $\epsilon_1 - \epsilon_2$, between the dots. However, the coupling is independent of the length of the island due to the presence of the MZMs.

In the even Coulomb valleys of the island (e.g., around $n_g = 0$), the situation is different. Now, the ground state is a linear combination of $|0000\rangle$ and $|1100\rangle$. To couple these states, which have a different total number of particles, one should introduce a Josephson coupling by connecting the SC to ground via a Josephson junction in a three-terminal geometry (see Fig 9.2b). Now third-order processes consisting of normal, anomalous, and Josephson tunneling connect the two states. In this case, the coupling is strongest when $\epsilon_1 = -\epsilon_2$, so that $|0000\rangle$ and $|1100\rangle$ have the same energy. Moreover, the coupling is only significant in a small region around n_g = even with width $\propto E_J / E_C$ [242].

The coupling between the distant quantum dots can be measured using dispersive gate sensing. If $E_J = 0$, we expect a finite frequency shift in the odd valleys, but no frequency shift in the even valleys. Since the frequency shift is inversely proportional to the coupling, we expect the largest signal around n_g = odd where the energy gap due to charging effects is highest. For finite E_J, an additional peak in the frequency shift around n_g = even can appear. The two different peaks can be distinguished by tuning the onsite energy of the QDs; The coupling in the odd (even) valley is largest when the QD level alignment is symmetric (asymmetric). An important feature for the Majorana-mediated coupling is that it is insensitive to the

Figure 9.2 – **Majorana-mediated double dot hybridization.** With the sample geometry in **a** (and a global even parity), the QDs can be coupled when the Majorana island is in the odd Coulomb valley. **b** The Josephson coupling to a third terminal makes it possible to change the number of particles in the system. Now the QDs can also hybridize when the Majorana island is in the even Coulomb valley.

length of the island. It is therefore interesting to measure the coupling between distant QDs for various SC lengths.

In an extension of the experiment, the coherent coupling between the distant QDs can be studied in more detail using photon-assisted cotunneling, following ref. 244. Furthermore, this Majorana-mediated coupling can be use to realize long-distant coupling of spin qubits. As an initial experiment in that direction, we propose to construct a singlet-triplet qubit using the two QDs [162, 245]. Coupling between Majoranas and spin qubits could be useful for implementing arbitrary single qubit rotations on Majorana qubits [246, 247].

9.4. Majorana parity readout

Finally, we discuss an initial implementation of the MBQ for which the double QD (DQD) is only connected to one pair of MZMs [17, 18]. This configuration is also referred to as the loop qubit due to its geometry, see 9.3a. This qubit can only be readout in the $z = i\gamma_2\gamma_3$ basis which is insufficient for executing topological operations. Still, we think the loop qubit is an important milestone because it can be used to test the parity readout of MZMs. Here, we propose to employ this readout to measure the fluctuations in Majorana parity due to poisoning with quasiparticles.

To measure Majorana parity fluctuations, a large contrast between the even and odd parity signals is needed. To tune the MBQ to a good readout point, the flux dependence of the tunnel coupling of the DQD can be measured. The flux modulates the tunnel coupling with a 2π period due interference of single electrons, see Fig 9.3b. For maximum contrast, the tunnel coupling t through both arms should be equal, so that, for $\varphi - \varphi_0 = n\pi$ with integer n, there is complete constructive/destructive interfere depending on the parity of the Majorana pair, see Eq. 2.32. For the DQD measured in Chapter 5, we found a maximum signal-to-noise ratio (SNR $\approx$ 2 in 1 µs) for a tunneling amplitude of 5 GHz. For the MBQ, this translates to $t = 2.5$ GHz through both arms to achieve maximum contrast and large SNR. We note that this optimal coupling might be setup/sample dependent, and that it should be calibrated for each box qubit independently. The optimal value of $t_{co} = 2.5$ GHz seem realistic; a crude estimation using $t_{co} \approx t^2/E_C$, with $E_C \approx 100$ µeV gives $t \approx 16$ GHz, well within the range of tunnel coupling measured in chapter 5. However, we note that MZM-QD coupling could be different from QD-QD coupling [248], and experiments, such as the one proposed in the previous section, should provide a better picture of the attainable cotunneling couplings. With the readout tuned, we can measure the Majorana parity lifetime by monitoring the signal as a function of time $X(t)$. Figure 9.3d shows a typical time trace, simulated with a SNR of 2 and an integration time much shorter than the typical parity lifetime. Clearly, the signal jumps between two values $X_{e,o}$, indicating that the parity fluctuations can be resolved.

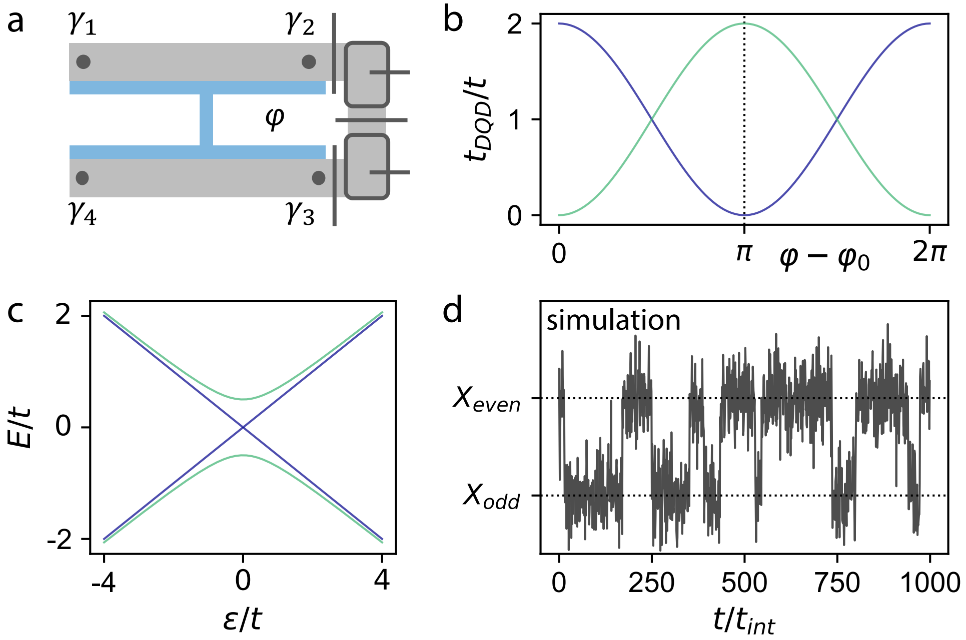

Figure 9.3 – **Majorana parity readout in a Majorana box qubit.** **a** Minimal setup to do a Majorana parity measurement using a Majorana box qubit. Because of the loop, this device is sometimes referred to as the loop qubit. **b** Tunnel coupling between the dots as a function of flux through the loop for different parity states (with even/odd in blue/green). When $\varphi - \varphi_0 = n\pi$ with integer n, the contrast between the parity states is maximal. **c** Energy spectrum of the double dot at the point of maximal contrast. **d** Time trace of the reflected signal X showing parity fluctuations. For this simulation, we used an exponential distribution for the parity switches with $\tau_{\text{even}} = 100\ t_{\text{int}}$ and $\tau_{\text{odd}} = 50\ t_{\text{int}}$, and a signal-to-noise ratio of 2.

Bibliography

[1] M. Kumar, *Quantum: Einstein, Bohr, and the Great Debate about the Nature of Reality* (W. W. Norton, 2008).

[2] A. Tonomura, J. Endo, T. Matsuda, T. Kawasaki, and H. Ezawa, American Journal of Physics **57**, 117 (1989).

[3] S. J. Freedman and J. F. Clauser, Physical Review Letters **28**, 938 (1972).

[4] R. P. Feynman, International journal of theoretical physics **21**, 467 (1982).

[5] P. W. Shor, *Algorithms for quantum computation: Discrete logarithms and factoring,* in *Proceedings 35th annual symposium on foundations of computer science* (IEEE, 1994) pp. 124–134.

[6] S. Jordan, *Quantum algorithm zoo,* (2019).

[7] H. L. Stormer, Reviews of Modern Physics **71**, 875 (1999).

[8] M. A. Nielsen and I. Chuang, *Quantum computation and quantum information,* (2002).

[9] T. D. Ladd, F. Jelezko, R. Laflamme, Y. Nakamura, C. Monroe, and J. L. O'Brien, Nature **464**, 45 (2010).

[10] L. M. K. Vandersypen, H. Bluhm, J. S. Clarke, A. S. Dzurak, R. Ishihara, A. Morello, D. J. Reilly, L. R. Schreiber, and M. Veldhorst, npj Quantum Information **3**, 34 (2017).

[11] M. H. Devoret and R. J. Schoelkopf, Science **339**, 1169 (2013).

[12] B. M. Terhal, Reviews of Modern Physics **87**, 307 (2015).

[13] K. Von Klitzing, Reviews of Modern Physics **58**, 519 (1986).

[14] C. Nayak, S. H. Simon, A. Stern, M. Freedman, and S. Das Sarma, Reviews of Modern Physics **80**, 1083 (2008).

[15] T. Hyart, B. Van Heck, I. C. Fulga, M. Burrello, A. R. Akhmerov, and C. W. J. Beenakker, Physical Review B **88**, 035121 (2013).

[16] D. Aasen, M. Hell, R. V. Mishmash, A. Higginbotham, J. Danon, M. Leijnse, T. S. Jespersen, J. A. Folk, C. M. Marcus, K. Flensberg, *et al.*, Physical Review X **6**, 031016 (2016).

[17] S. Plugge, A. Rasmussen, R. Egger, and K. Flensberg, New Journal of Physics **19**, 012001 (2017).

[18] T. Karzig, C. Knapp, R. M. Lutchyn, P. Bonderson, M. B. Hastings, C. N., J. A., K. Flensberg, S. Plugge, Y. O., C. M. Marcus, and M. H. Freedman, Physical Review B **95**, 235305 (2017).

[19] Y. Oreg, G. Refael, and F. von Oppen, Physical review letters **105**, 177002 (2010).

[20] R. M. Lutchyn, J. D. Sau, and S. Das Sarma, Physical review letters **105**, 077001 (2010).

[21] R. Aguado, La Rivista del Nuovo Cimento (2017), 10.1393/ncr/i2017-10141-9.

[22] M. Leijnse and K. Flensberg, Semiconductor Science and Technology **27**, 124003 (2012).

[23] C. W. J. Beenakker, Annu. Rev. Condens. Matter Phys. **4**, 113 (2013).

[24] J. Alicea, Reports on progress in physics **75**, 076501 (2012).

[25] R. M. Lutchyn, E. P. A. M. Bakkers, L. P. Kouwenhoven, P. Krogstrup, C. M. Marcus, and Y. Oreg, Nature Reviews Materials , 1 (2018).

[26] M. Tinkham, *Introduction to superconductivity* (Courier Corporation, 2004).

[27] P.-G. De Gennes, *Superconductivity of metals and alloys* (CRC Press, 2018).

[28] J. Bardeen, L. N. Cooper, and J. R. Schrieffer, Physical Review **108**, 1175 (1957).

[29] A. Y. Kitaev, Physics-Uspekhi **44**, 131 (2001).

[30] L. Fu and C. L. Kane, Physical review letters **100**, 096407 (2008).

[31] J. Kammhuber, *Spin-orbit interaction in ballistic nanowire devices*, Ph.D. thesis, TU Delft (2017).

[32] T. D. Stanescu and S. Tewari, Journal of Physics: Condensed Matter **25**, 233201 (2013).

[33] K. Zuo and V. Mourik, *Signatures of Majorana Fermions in Hybrid Superconductor-Semiconductor Nanowire Devices*, Ph.D. thesis, TU Delft (2016).

[34] V. Mourik, K. Zuo, S. M. Frolov, S. R. Plissard, E. P. A. M. Bakkers, and L. P. Kouwenhoven, Science **336**, 1003 (2012).

[35] M. T. Deng, S. Vaitiekėnas, E. B. Hansen, J. Danon, M. Leijnse, K. Flensberg, J. Nygård, P. Krogstrup, and C. M. Marcus, Science **354**, 1557 (2016).

[36] H. Zhang, C.-X. Liu, S. Gazibegovic, D. Xu, J. A. Logan, G. Wang, N. Van Loo, J. D. S. Bommer, M. W. A. De Moor, D. Car, *et al.*, Nature **556**, 74 (2018).

[37] D. Laroche, D. Bouman, D. J. van Woerkom, A. Proutski, C. Murthy, D. I. Pikulin, C. Nayak, R. J. J. van Gulik, J. Nygård, P. Krogstrup, *et al.*, Nature communications **10** (2017), 10.1038/s41467-018-08161-2.

[38] J. Alicea, Y. Oreg, G. Refael, F. Von Oppen, and M. P. A. Fisher, Nature Physics **7**, 412 (2011).

[39] M. Hell, J. Danon, K. Flensberg, and M. Leijnse, Phys. Rev. B **94**, 035424 (2016).

[40] S. Das Sarma, J. D. Sau, and T. D. Stanescu, Phys. Rev. B **86**, 220506 (2012).

[41] S. M. Albrecht, A. P. Higginbotham, M. Madsen, F. Kuemmeth, T. S. Jespersen, J. Nygård, P. Krogstrup, and C. M. Marcus, Nature **531**, 206 (2016).

[42] T. Ihn, *Semiconductor Nanostructures: Quantum states and electronic transport* (Oxford University Press, 2010).

[43] L. P. Kouwenhoven, D. G. Austing, and S. Tarucha, Reports on Progress in Physics **64**, 701 (2001).

[44] R. Hanson, L. P. Kouwenhoven, J. R. Petta, S. Tarucha, and L. M. K. Vandersypen, Reviews of Modern Physics **79**, 1217 (2007).

[45] J. M. Elzerman, R. Hanson, L. H. Willems van Beveren, B. Witkamp, L. M. K. Vandersypen, and L. P. Kouwenhoven, nature **430**, 431 (2004).

[46] J. R. Petta, A. C. Johnson, J. M. Taylor, E. A. Laird, A. Yacoby, M. D. Lukin, C. M. Marcus, M. P. Hanson, and A. C. Gossard, Science **309**, 2180 (2005).

[47] T. Hayashi, T. Fujisawa, H.-D. Cheong, Y. H. Jeong, and Y. Hirayama, Physical review letters **91**, 226804 (2003).

[48] S. De Franceschi, L. P. Kouwenhoven, C. Schönenberger, and W. Wernsdorfer, Nature Nanotechnology **5**, 703 (2010).

[49] M. Eich, R. Pisoni, H. Overweg, A. Kurzmann, Y. Lee, P. Rickhaus, T. Ihn, K. Ensslin, F. Herman, M. Sigrist, *et al.*, Physical Review X **8**, 031023 (2018).

[50] D. H. Cobden and J. Nygård, Physical review letters **89**, 046803 (2002).

[51] W. G. Van der Wiel, S. De Franceschi, J. M. Elzerman, T. Fujisawa, S. Tarucha, and L. P. Kouwenhoven, Reviews of Modern Physics **75**, 1 (2002).

[52] A. P. Higginbotham, S. M. Albrecht, G. Kiršanskas, W. Chang, F. Kuemmeth, P. Krogstrup, T. S. Jespersen, J. Nygård, K. Flensberg, and C. M. Marcus, Nature Phys. **11**, 1017 (2015).

[53] S. M. Albrecht, E. B. Hansen, A. P. Higginbotham, F. Kuemmeth, T. S. Jespersen, J. Nygård, P. Krogstrup, J. Danon, K. Flensberg, and C. M. Marcus, Physical Review Letters **118**, 137701 (2017).

[54] J. Shen, S. Heedt, F. Borsoi, B. Van Heck, S. Gazibegovic, R. L. M. Veld, D. Car, J. A. Logan, M. Pendharkar, G. Wang, D. Xu, D. Bouman, C. J. Geresdi A. Palmstrøm, E. P. A. M. Bakkers, and L. P. Kouwenhoven, Nature communications **9**, 4801 (2018).

[55] K. A. Matveev, M. Gisselfält, L. I. Glazman, M. Jonson, and R. I. Shekhter, Physical Review Letters **70**, 2940 (1993).

[56] D. V. Averin and K. K. Likharev, J. Low Temp. Phys. **62**, 345 (1986).

[57] D. V. Averin and Y. V. Nazarov, Physical Review Letters **69**, 1993 (1992).

[58] P. Lafarge, P. Joyez, D. Esteve, C. Urbina, and M. H. Devoret, Nature **365**, 422 (1993).

[59] P. Lafarge, P. Joyez, D. Esteve, C. Urbina, and M. H. Devoret, Physical review letters **70**, 994 (1993).

[60] P. Joyez, P. Lafarge, A. Filipe, D. Esteve, and M. H. Devoret, Physical Review Letters **72**, 2458 (1994).

[61] V. F. Maisi, S. V. Lotkhov, A. Kemppinen, A. Heimes, J. T. Muhonen, and J. P. Pekola, Physical review letters **111**, 147001 (2013).

[62] D. Chevallier, P. Simon, and C. Bena, Physical Review B **88**, 165401 (2013).

[63] F. W. J. Hekking, L. I. Glazman, K. A. Matveev, and R. I. Shekhter, Physical review letters **70**, 4138 (1993).

[64] B. Van Heck, R. M. Lutchyn, and L. I. Glazman, Physical Review B **93**, 235431 (2016).

[65] S. Vaitiekėnas, M. T. Deng, J. Nygård, P. Krogstrup, and C. M. Marcus, Phys. Rev. Lett. **121**, 037703 (2018).

[66] M. W. A. de Moor, J. D. S. Bommer, D. Xu, G. W. Winkler, A. E. Antipov, A. Bargerbos, G. Wang, N. van Loo, R. L. M. Op het Veld, S. Gazibegovic, D. Car, J. A. Logan, M. Pendharkar, J. S. Lee, E. P. A. M. Bakkers, C. J. Palmstrøm, R. M. Lutchyn, L. P. Kouwenhoven, and H. Zhang, New Journal of Physics **20**, 103049 (2018).

[67] C.-X. Liu, J. D. Sau, T. D. Stanescu, and S. Das Sarma, Physical Review B **96**, 075161 (2017).

[68] Y.-J. Doh, J. A. van Dam, A. L. Roest, E. P. A. M. Bakkers, L. P. Kouwenhoven, and S. De Franceschi, science **309**, 272 (2005).

[69] J. A. Aumentado, *The Cooper Pair Transistor*, Tech. Rep. (2010).

[70] K. M. Lang, S. Nam, J. Aumentado, C. Urbina, and J. M. Martinis, IEEE Transactions on Applied Superconductivity **13**, 989 (2003).

[71] D. Rainis and D. Loss, Phys. Rev. B **85**, 174533 (2012).

[72] M. D. Shaw, R. M. Lutchyn, P. Delsing, and P. M. Echternach, Phys. Rev. B **78**, 024503 (2008).

[73] J. Aumentado, M. W. Keller, J. M. Martinis, and M. H. Devoret, Phys. Rev. Lett. **92**, 066802 (2004).

[74] D. Ristè, C. C. Bultink, M. J. Tiggelman, R. N. Schouten, K. W. Lehnert, and L. DiCarlo, Nature communications **4**, 1913 (2013).

[75] K. Serniak, M. Hays, G. de Lange, S. Diamond, S. Shankar, L. D. Burkhart, L. Frunzio, M. Houzet, and M. H. Devoret, Phys. Rev. Lett. **121**, 157701 (2018).

[76] A. Bespalov, M. Houzet, J. S. Meyer, and Y. V. Nazarov, Physical review letters **117**, 117002 (2016).

[77] N. A. Court, A. J. Ferguson, R. M. Lutchyn, and R. G. Clark, Phys. Rev. B **77**, 100501 (2008).

[78] M. Taupin, I. M. Khaymovich, M. Meschke, A. S. Melnikov, and J. P. Pekola, Nature communications **7**, 10977 (2016).

[79] M. T. Tuominen, J. M. Hergenrother, T. S. Tighe, and M. Tinkham, Physical Review Letters **69**, 1997 (1992).

[80] J. D. Sau, D. J. Clarke, and S. Tewari, Physical Review B **84**, 094505 (2011).

[81] B. Van Heck, A. R. Akhmerov, F. Hassler, M. Burrello, and C. W. J. Beenakker, New Journal of Physics **14**, 035019 (2012).

[82] L. Fu, Physical review letters **104**, 056402 (2010).

[83] C. Schrade and L. Fu, Physical review letters **121**, 267002 (2018).

[84] M. Esterli, R. M. Otxoa, and M. F. Gonzalez-Zalba, arXiv preprint arXiv:1812.06056 (2018).

[85] R. Mizuta, R. M. Otxoa, A. C. Betz, and M. F. Gonzalez-Zalba, Physical Review B **95**, 045414 (2017).

[86] P. Scarlino, D. J. van Woerkom, U. C. Mendes, J. V. Koski, A. J. Landig, C. K. Andersen, S. Gasparinetti, C. Reichl, W. Wegscheider, K. Ensslin, *et al.*, arXiv preprint arXiv:1806.10039 (2018).

[87] A. Blais, R.-S. Huang, A. Wallraff, S. M. Girvin, and R. J. Schoelkopf, Physical Review A **69**, 062320 (2004).

[88] K. D. Petersson, L. W. McFaul, M. D. Schroer, M. Jung, J. M. Taylor, A. A. Houck, and J. R. Petta, Nature **490**, 380 (2012).

[89] T. S. Frey, *Interaction between quantum dots and superconducting microwave resonators*, Ph.D. thesis, ETH Zurich (2013).

[90] D. M. Pozar, *Microwave Engineering* (Wiley, 2004).

[91] J. M. Hornibrook, J. I. Colless, A. C. Mahoney, X. G. Croot, S. Blanvillain, H. Lu, A. C. Gossard, and D. J. Reilly, Applied Physics Letters **104**, 103108 (2014).

[92] R. Schouten, *QT designed instrumentation,* (2019).

[93] P. Krogstrup, N. L. B. Ziino, W. Chang, S. M. Albrecht, M. H. Madsen, E. Johnson, J. Nygård, C. M. Marcus, and T. S. Jespersen, Nature Mater. **14**, 400 (2015).

[94] A. E. Antipov, A. Bargerbos, G. W. Winkler, B. Bauer, E. Rossi, and R. M. Lutchyn, Phys. Rev. X **8**, 031041 (2018).

[95] W. Chang, S. M. Albrecht, T. S. Jespersen, F. Kuemmeth, P. Krogstrup, J. Nygård, and C. M. Marcus, Nature Nanotech. **10**, 232 (2015).

[96] Ö. Gül, H. Zhang, F. K. de Vries, J. van Veen, K. Zuo, V. Mourik, S. Conesa-Boj, M. P. Nowak, D. J. Van Woerkom, M. Quintero-Perez, *et al.*, Nano letters **17**, 2690 (2017).

[97] S. Takei, B. M. Fregoso, H.-Y. Hui, A. M. Lobos, and S. Das Sarma, Physical review letters **110**, 186803 (2013).

[98] Ö. Gül, D. J. Van Woerkom, I. van Weperen, D. Car, S. R. Plissard, E. P. A. M. Bakkers, and L. P. Kouwenhoven, Nanotechnology **26**, 215202 (2015).

[99] K. Flöhr *et al.*, **82**, 113705 (2011).

[100] T. company Inc., *Semiconductor and Thin Film Etchants for Microelectronic Circuits,* (2019).

[101] H. Grabert and M. H. Devoret, *Single charge tunneling: Coulomb blockade phenomena in nanostructures*, Vol. 294 (Springer Science & Business Media, 2013).

[102] L. J. Geerligs, V. F. Anderegg, J. Romijn, and J. E. Mooij, Physical Review Letters **65**, 377 (1990).

[103] T. M. Eiles and J. M. Martinis, Phys. Rev. B **50**, 627 (1994).

[104] J. Männik and J. E. Lukens, Physical Review Letters **92**, 057004 (2004).

[105] O. Naaman and J. Aumentado, Phys. Rev. B **73**, 172504 (2006).

[106] A. J. Ferguson, N. A. Court, F. E. Hudson, and R. G. Clark, Physical Review Letters **97**, 106603 (2006).

[107] D. Sherman, J. S. Yodh, S. M. Albrecht, J. Nygård, P. Krogstrup, and C. M. Marcus, Nature Nanotech. **12**, 212 (2017).

[108] E. C. T. O'Farrell, A. C. C. Drachmann, M. Hell, A. Fornieri, A. M. Whiticar, E. B. Hansen, S. Gronin, G. C. Gardner, C. Thomas, M. J. Manfra, K. Flensberg, C. M. Marcus, and F. Nichele, Physical review letters **121**, 256803 (2018).

[109] D. Litinski, M. S. Kesselring, J. Eisert, and F. von Oppen, Phys. Rev. X **7**, 031048 (2017).

[110] V. Ambegaokar, U. Eckern, and G. Schön, Phys. Rev. Lett. **48**, 1745 (1982).

[111] A. I. Larkin and Y. N. Ovchinnikov, Phys. Rev. B **28**, 6281 (1983).

[112] U. Eckern, G. Schön, and V. Ambegaokar, Phys. Rev. B **30**, 6419 (1984).

[113] R. M. Lutchyn, Phys. Rev. B **75**, 212501 (2007).

[114] R. M. Lutchyn, K. Flensberg, and L. I. Glazman, Phys. Rev. B **94**, 125407 (2016).

[115] R. M. Lutchyn and L. I. Glazman, Phys. Rev. B **75**, 184520 (2007).

[116] D. J. Van Woerkom, A. Geresdi, and L. P. Kouwenhoven, Nature Phys. **11**, 547 (2015).

[117] P. Hadley, E. Delvigne, E. H. Visscher, S. Lähteenmäki, and J. E. Mooij, Phys. Rev. B **58**, 15317 (1998).

[118] K. A. Matveev, L. I. Glazman, and R. I. Shekhter, Mod. Phys. Lett. B **08**, 1007 (1994).

[119] R. L. Kautz and J. M. Martinis, Physical Review B **42**, 9903 (1990).

[120] M. T. Tuominen, J. M. Hergenrother, T. S. Tighe, and M. Tinkhsam, Phys. Rev. B **47**, 11599 (1993).

[121] F. Setiawan, W. S. Cole, J. D. Sau, and S. Das Sarma, Phys. Rev. B **95**, 020501 (2017).

[122] P. San-Jose, J. Cayao, E. Prada, and R. Aguado, New J. Phys. **15**, 075019 (2013).

[123] S. Nadj-Perge, I. K. Drozdov, J. Li, H. Chen, S. Jeon, J. Seo, A. H. MacDonald, B. A. Bernevig, and A. Yazdani, Science **346**, 602 (2014).

[124] M. Ruby, F. Pientka, Y. Peng, F. von Oppen, B. W. Heinrich, and K. J. Franke, Phys. Rev. Lett. **115**, 197204 (2015).

[125] A. Hosseinkhani and G. Catelani, Phys. Rev. B **97**, 054513 (2018).

[126] A. Wallraff, D. I. Schuster, A. Blais, L. Frunzio, J. Majer, M. H. Devoret, S. M. Girvin, and R. J. Schoelkopf, Physical Review Letters **95**, 060501 (2005).

[127] A. C. Betz, R. Wacquez, M. Vinet, X. Jehl, A. L. Saraiva, M. Sanquer, A. J. Ferguson, and M. F. Gonzalez-Zalba, Nano Letters **15**, 4622 (2015).

[128] J. I. Colless, A. C. Mahoney, J. M. Hornibrook, A. C. Doherty, H. Lu, A. C. Gossard, and D. J. Reilly, Physical Review Letters **110**, 046805 (2013).

[129] R. Vijay, D. H. Slichter, and I. Siddiqi, Physical Review Letters **106**, 110502 (2011).

[130] P. Bonderson, M. Freedman, and C. Nayak, Physical Review Letters **101**, 010501 (2008).

[131] N. J. Lambert, A. A. Esmail, M. Edwards, F. A. Pollock, B. W. Lovett, and A. J. Ferguson, Applied Physics Letters **109**, 112603 (2016).

[132] T. Frey, P. J. Leek, M. Beck, A. Blais, T. Ihn, K. Ensslin, and A. Wallraff, Physical Review Letters **108**, 046807 (2012).

[133] M. D. Schroer, M. Jung, K. D. Petersson, and J. R. Petta, Physical Review Letters **109**, 166804 (2012).

[134] A. West, B. Hensen, A. Jouan, T. Tanttu, C. H. Yang, A. Rossi, M. F. Gonzalez-Zalba, F. E. Hudson, A. Morello, D. J. Reilly, and A. S. Dzurak, (2018), arXiv:1809.01864 .

[135] P. Pakkiam, A. V. Timofeev, M. G. House, M. R. Hogg, T. Kobayashi, M. Koch, S. Rogge, and M. Y. Simmons, Physical Review X **8**, 041032 (2018).

[136] M. Urdampilleta, D. J. Niegemann, E. Chanrion, B. Jadot, C. Spence, P.-A. Mortemousque, C. Bäuerle, L. Hutin, B. Bertrand, S. Barraud, R. Maurand, M. Sanquer, X. Jehl, S. De Franceschi, M. Vinet, and T. Meunier, (2018), arXiv:1809.04584 .

[137] T. Walter, P. Kurpiers, S. Gasparinetti, P. Magnard, A. Potočnik, Y. Salathé, M. Pechal, M. Mondal, M. Oppliger, C. Eichler, and A. Wallraff, Physical Review Applied **7**, 054020 (2017).

[138] S. Nadj-Perge, S. M. Frolov, E. P. A. M. Bakkers, and L. P. Kouwenhoven, Nature **468**, 1084 (2010).

[139] A. Das, Y. Ronen, Y. Most, Y. Oreg, M. Heiblum, and H. Shtrikman, Nature Physics **8**, 887 (2012).

[140] T. Ota, T. Hayashi, K. Muraki, and T. Fujisawa, Applied Physics Letters **96**, 032104 (2010).

[141] R. C. Ashoori, H. L. Stormer, J. S. Weiner, L. N. Pfeiffer, S. J. Pearton, K. W. Baldwin, and K. W. West, Physical Review Letters **68**, 3088 (1992).

[142] T. Duty, G. Johansson, K. Bladh, D. Gunnarsson, C. Wilson, and P. Delsing, Physical Review Letters **95**, 206807 (2005).

[143] W. G. van der Wiel, S. De Franceschi, J. M. Elzerman, T. Fujisawa, S. Tarucha, and L. P. Kouwenhoven, Reviews of Modern Physics **75**, 1 (2002).

[144] K. D. Petersson, C. G. Smith, D. Anderson, P. Atkinson, G. A. C. Jones, and D. A. Ritchie, Nano Letters **10**, 2789 (2010).

[145] M. A. Castellanos-Beltran, K. D. Irwin, G. C. Hilton, L. R. Vale, and K. W. Lehnert, Nature Physics **4**, 929 (2008).

[146] C. Macklin, K. O'Brien, D. Hover, M. E. Schwartz, V. Bolkhovsky, X. Zhang, W. D. Oliver, and I. Siddiqi, Science **350**, 307 (2015).

[147] J. Stehlik, Y.-Y. Liu, C. M. Quintana, C. Eichler, T. R. Hartke, and J. R. Petta, Physical Review Applied **4**, 014018 (2015).

[148] F. J. Schupp, N. Ares, A. Mavalankar, J. Griffiths, G. A. C. Jones, I. Farrer, D. A. Ritchie, C. G. Smith, G. A. D. Briggs, and E. A. Laird, (2018), arXiv:1810.05767 .

[149] I. Ahmed, J. A. Haigh, S. Schaal, S. Barraud, Y. Zhu, C. Lee, M. Amado, J. W. A. Robinson, A. Rossi, J. J. L. Morton, and M. F. Gonzalez-Zalba, Physical Review Applied **10** (2018), 10.1103/physrevapplied.10.014018.

[150] J. A. Van Dam, Y. V. Nazarov, E. P. A. M. Bakkers, S. De Franceschi, and L. P. Kouwenhoven, Nature **442**, 667 (2006).

[151] D. B. Szombati, S. Nadj-Perge, D. Car, S. R. Plissard, E. P. A. M. Bakkers, and L. P. Kouwenhoven, Nature Physics **12**, 568 (2016).

[152] L. Hofstetter, S. Csonka, J. Nygård, and C. Schönenberger, Nature **461**, 960 (2009).

[153] L. G. Herrmann, F. Portier, P. Roche, A. Levy Yeyati, T. Kontos, and C. Strunk, Physical review letters **104**, 026801 (2010).

[154] D. C. Ralph, C. T. Black, and M. Tinkham, Physical review letters **74**, 3241 (1995).

[155] E. J. H. Lee, X. Jiang, M. Houzet, R. Aguado, C. M. Lieber, and S. De Franceschi, Nature nanotechnology **9**, 79 (2014).

[156] A. Wallraff, D. I. Schuster, A. Blais, L. Frunzio, R.-. S. Huang, J. Majer, S. Kumar, S. M. Girvin, and R. J. Schoelkopf, Nature **431**, 162 (2004).

[157] A. A. Esmail, A. J. Ferguson, and N. J. Lambert, Applied Physics Letters **111**, 252602 (2017).

[158] M. F. Gonzalez-Zalba, S. Barraud, A. J. Ferguson, and A. C. Betz, Nature communications **6**, 6084 (2015).

[159] L. E. Bruhat, J. J. Viennot, M. C. Dartiailh, M. M. Desjardins, T. Kontos, and A. Cottet, Physical Review X **6**, 021014 (2016).

[160] E. B. Hansen, J. Danon, and K. Flensberg, Physical Review B **97**, 041411 (2018).

[161] A. Cottet, C. Mora, and T. Kontos, Physical Review B **83**, 121311 (2011).

[162] M. Leijnse and K. Flensberg, Physical review letters **111**, 060501 (2013).

[163] C. W. Groth, M. Wimmer, A. R. Akhmerov, and X. Waintal, New Journal of Physics **16**, 063065 (2014).

[164] I. Žutić, J. Fabian, and S. Das Sarma, Reviews of modern physics **76**, 323 (2004).

[165] J. D. Sau, R. M. Lutchyn, S. Tewari, and S. Das Sarma, Physical review letters **104**, 040502 (2010).

[166] J. Alicea, Physical Review B **81**, 125318 (2010).

[167] I. Vurgaftman, J. R. Meyer, and L. R. Ram-Mohan, Journal of applied physics **89**, 5815 (2001).

[168] H. A. Nilsson, P. Caroff, C. Thelander, M. Larsson, J. B. Wagner, L.-E. Wernersson, L. Samuelson, and H. Q. Xu, Nano letters **9**, 3151 (2009).

[169] S. Lamari, Journal of applied physics **91**, 1698 (2002).

[170] P. Středa and P. Šeba, Physical review letters **90**, 256601 (2003).

[171] S. R. Plissard, I. Van Weperen, D. Car, M. A. Verheijen, G. W. G. Immink, J. Kammhuber, L. J. Cornelissen, D. B. Szombati, A. Geresdi, S. M. Frolov, *et al.*, Nature nanotechnology **8**, 859 (2013).

[172] S. Gazibegovic, D. Car, H. Zhang, S. C. Balk, J. A. Logan, M. W. A. de Moor, M. C. Cassidy, R. Schmits, D. Xu, G. Wang, *et al.*, Nature **548**, 434 (2017).

[173] F. Krizek, J. E. Sestoft, P. Aseev, S. Marti-Sanchez, S. Vaitiekėnas, L. Casparis, S. A. Khan, Y. Liu, T. Stankevič, A. M. Whiticar, *et al.*, Physical Review Materials **2**, 093401 (2018).

[174] S. Vaitiekėnas, A. M. Whiticar, M.-T. Deng, F. Krizek, J. E. Sestoft, C. J. Palmstrøm, S. Marti-Sanchez, J. Arbiol, P. Krogstrup, L. Casparis, *et al.*, Physical review letters **121**, 147701 (2018).

[175] W. Yi, A. A. Kiselev, J. Thorp, R. Noah, B.-M. Nguyen, S. Bui, R. D. Rajavel, T. Hussain, M. F. Gyure, P. Kratz, *et al.*, Applied Physics Letters **106**, 142103 (2015).

[176] K. J. Goldammer, S. J. Chung, W. K. Liu, M. B. Santos, J. L. Hicks, S. Raymond, and S. Q. Murphy, Journal of crystal growth **201**, 753 (1999).

[177] J. M. S. Orr, A. M. Gilbertson, M. Fearn, O. W. Croad, C. J. Storey, L. Buckle, M. T. Emeny, P. D. Buckle, and T. Ashley, Physical Review B **77**, 165334 (2008).

[178] G. A. Khodaparast, R. E. Doezema, S. J. Chung, K. J. Goldammer, and M. B. Santos, Physical Review B **70**, 155322 (2004).

[179] G. A. Khodaparast, R. C. Meyer, X. H. Zhang, T. Kasturiarachchi, R. E. Doezema, S. J. Chung, N. Goel, M. B. Santos, and Y. J. Wang, Physica E: Low-dimensional Systems and Nanostructures **20**, 386 (2004).

[180] R. L. Kallaher, J. J. Heremans, N. Goel, S. J. Chung, and M. B. Santos, Physical Review B **81**, 075303 (2010).

[181] A. M. Gilbertson, M. Fearn, J. H. Jefferson, B. N. Murdin, P. D. Buckle, and L. F. Cohen, Physical Review B **77**, 165335 (2008).

[182] M. A. Leontiadou, K. L. Litvinenko, A. M. Gilbertson, C. R. Pidgeon, W. R. Branford, L. F. Cohen, M. Fearn, T. Ashley, M. T. Emeny, B. N. Murdin, *et al.*, Journal of Physics: Condensed Matter **23**, 035801 (2011).

[183] A. M. Gilbertson, W. R. Branford, M. Fearn, L. Buckle, P. D. Buckle, T. Ashley, and L. F. Cohen, Physical Review B **79**, 235333 (2009).

[184] I. Van Weperen, B. Tarasinski, D. Eeltink, V. S. Pribiag, S. R. Plissard, E. P. A. M. Bakkers, L. P. Kouwenhoven, and M. Wimmer, Physical Review B **91**, 201413 (2015).

[185] J. Nitta, T. Akazaki, H. Takayanagi, and T. Enoki, Physical Review Letters **78**, 1335 (1997).

[186] N. Goel, J. Graham, J. C. Keay, K. Suzuki, S. Miyashita, M. B. Santos, and Y. Hirayama, Physica E: Low-dimensional Systems and Nanostructures **26**, 455 (2005).

[187] I. van Weperen, S. R. Plissard, E. P. A. M. Bakkers, S. M. Frolov, and L. P. Kouwenhoven, Nano letters **13**, 387 (2012).

[188] J. Kammhuber, M. C. Cassidy, H. Zhang, Ö. Gül, F. Pei, M. W. A. de Moor, B. Nijholt, K. Watanabe, T. Taniguchi, D. Car, *et al.*, Nano letters **16**, 3482 (2016).

[189] M. de la Mata, R. Leturcq, S. R. Plissard, C. Rolland, C. Mageen, J. Arbiol, and P. Caroff, Nano letters **16**, 825 (2016).

[190] M. M. Uddin, H. W. Liu, K. F. Yang, K. Nagase, K. Sekine, C. K. Gaspe, T. D. Mishima, M. B. Santos, and Y. Hirayama, Applied Physics Letters **103**, 123502 (2013).

[191] A. C. Graham, K. J. Thomas, M. Pepper, N. R. Cooper, M. Y. Simmons, and D. A. Ritchie, Physical review letters **91**, 136404 (2003).

[192] R. Winkler, *Spin-orbit coupling effects in two-dimensional electron and hole systems*, Vol. 191 (Springer Science & Business Media, 2003).

[193] B. Nedniyom, R. J. Nicholas, M. T. Emeny, L. Buckle, A. M. Gilbertson, P. D. Buckle, and T. Ashley, Physical Review B **80**, 125328 (2009).

[194] A. A. Kiselev and K. W. Kim, Phys. Status Solidi B **215**, 235 (1999).

[195] E. L. Ivchenko and A. A. Kiselev, Soviet physics. Semiconductors **26**, 827 (1992).

[196] B. J. Van Wees, L. P. Kouwenhoven, H. Van Houten, C. W. J. Beenakker, J. E. Mooij, C. T. Foxon, and J. J. Harris, Physical Review B **38**, 3625 (1988).

[197] K.-F. Berggren, T. J. Thornton, D. J. Newson, and M. Pepper, Physical review letters **57**, 1769 (1986).

[198] C. W. J. Beenakker and H. van Houten, *Quantum transport in semiconductor nanostructures,* in *Solid state physics*, Vol. 44 (Elsevier, 1991) pp. 1–228.

[199] J. Fabian, A. Matos-Abiague, C. Ertler, P. Stano, and I. Žutić, Acta Physica Slovaca. Reviews and Tutorials **57** (2007), 10.2478/v10155-010-0086-8.

[200] D. Grundler, Physical Review Letters **84**, 6074 (2000).

[201] B. Shojaei, P. J. J. O'Malley, J. Shabani, P. Roushan, B. D. Schultz, R. M. Lutchyn, C. Nayak, J. M. Martinis, and C. J. Palmstrøm, Phys. Rev. B **93** (2016), 10.1103/physrevb.93.075302.

[202] S. Datta and B. Das, Applied Physics Letters **56**, 665 (1990).

[203] H. Kroemer, Physica E: Low-dimensional Systems and Nanostructures **20**, 196 (2004).

[204] C. Liu, T. L. Hughes, X.-L. Qi, K. Wang, and S.-C. Zhang, Physical Review Letters **100** (2008), 10.1103/physrevlett.100.236601.

[205] F. Qu, A. J. A. Beukman, S. Nadj-Perge, M. Wimmer, B.-M. Nguyen, W. Yi, J. Thorp, M. Sokolich, A. A. Kiselev, M. J. Manfra, C. M. Marcus, and L. P. Kouwenhoven, Physical Review Letters **115** (2015), 10.1103/physrevlett.115.036803.

[206] E. A. de Andrada e Silva, G. C. L. Rocca, and F. Bassani, Phys. Rev. B **50**, 8523 (1994).

[207] L. J. Cooper, N. K. Patel, V. Drouot, E. H. Linfield, D. A. Ritchie, and M. Pepper, Phys. Rev. B **57**, 11915 (1998).

[208] A. Zakharova, S. Yen, and K. Chao, Phys. Rev. B **64** (2001), 10.1103/physrevb.64.235332.

[209] E. Halvorsen, Y. Galperin, and K. A. Chao, Phys. Rev. B **61**, 16743 (2000).

[210] W. Xu, L. L. Li, H. M. Dong, G. Gumbs, and P. A. Folkes, J. Appl. Phys. **108**, 053709 (2010).

[211] F. Nichele, M. Kjaergaard, H. J. Suominen, R. Skolasinski, M. Wimmer, B.-M. Nguyen, A. A. Kiselev, W. Yi, M. Sokolich, M. J. Manfra, F. Qu, A. J. A. Beukman, L. P. Kouwenhoven, and C. M. Marcus, Physical Review Letters **118**, 016801 (2017).

[212] J. Li, K. Chang, G. Q. Hai, and K. S. Chan, Applied Physics Letters **92**, 152107 (2008).

[213] B.-M. Nguyen, W. Yi, R. Noah, J. Thorp, and M. Sokolich, Applied Physics Letters **106**, 032107 (2015).

[214] L. Onsager, The London, Edinburgh, and Dublin Philosophical Magazine and Journal of Science **43**, 1006 (1952).

[215] T. H. Sander, S. N. Holmes, J. J. Harris, D. K. Maude, and J. C. Portal, Phys. Rev. B **58**, 13856 (1998).

[216] A. C. H. Rowe, J. Nehls, R. A. Stradling, and R. S. Ferguson, Phys. Rev. B **63** (2001), 10.1103/physrevb.63.201307.

[217] D. C. Tsui, T. Englert, A. Y. Cho, and A. C. Gossard, Phys. Rev. Lett. **44**, 341 (1980).

[218] V. L. Gurevich and Y. A. Firsov, Soviet Physics Jetp-Ussr **13**, 137 (1961).

[219] N. S. Averkiev, M. M. Glazov, and S. A. Tarasenko, Solid State Communications **133**, 543 (2005).

[220] D. M. Symons, M. Lakrimi, R. J. Nicholas, D. K. Maude, J. C. Portal, N. J. Mason, and P. J. Walker, Phys. Rev. B **58**, 7292 (1998).

[221] D. Shoenberg, *Magnetic oscillations in metals* (Cambridge University Press (CUP), 1984).

[222] S. D. Ganichev, V. V. Bel'kov, L. E. Golub, E. L. Ivchenko, P. Schneider, S. Giglberger, J. Eroms, J. D. Boeck, G. Borghs, W. Wegscheider, D. Weiss, and W. Prettl, Phys. Rev. Lett. **92** (2004), 10.1103/physrevlett.92.256601.

[223] X. Mu, G. Sullivan, and R.-R. Du, Appl. Phys. Lett. **108**, 012101 (2016).

[224] F. Herzog, H. Hardtdegen, T. Schäpers, D. Grundler, and M. A. Wilde, New Journal of Physics **19**, 103012 (2017).

[225] Y. A. Bychkov and E. I. Rashba, Journal of physics C: Solid state physics **17**, 6039 (1984).

[226] Y. A. Bychkov and E. I. Rashba, JETP lett **39**, 78 (1984).

[227] M. Studer, G. Salis, K. Ensslin, D. C. Driscoll, and A. C. Gossard, Phys. Rev. Lett. **103**, 027201 (2009).

[228] J. Luo, H. Munekata, F. F. Fang, and P. J. Stiles, Phys. Rev. B **41**, 7685 (1990).

[229] G. Kells, D. Meidan, and P. W. Brouwer, Physical Review B **86**, 100503 (2012).

[230] A. Vuik, B. Nijholt, A. R. Akhmerov, and M. Wimmer, arXiv:1806.02801 (2018).

[231] Ö. Gül, H. Zhang, J. D. S. Bommer, M. W. A. de Moor, D. Car, S. R. Plissard, E. P. A. M. Bakkers, A. Geresdi, K. Watanabe, T. Taniguchi, *et al.*, Nature nanotechnology **13**, 192 (2018).

[232] F. Nichele, H. J. Suominen, M. Kjaergaard, C. M. Marcus, E. Sajadi, J. A. Folk, F. Qu, A. J. A. Beukman, F. K. de Vries, J. van Veen, *et al.*, New Journal of Physics **18**, 083005 (2016).

[233] C. T. Ke, C. M. Moehle, F. K. de Vries, C. Thomas, S. Metti, C. R. Guinn, R. Kallaher, M. Lodari, G. Scappucci, T. Wang, *et al.*, arXiv:1902.10742 (2019).

[234] J. Shabani, M. Kjaergaard, H. J. Suominen, Y. Kim, F. Nichele, K. Pakrouski, T. Stankevic, R. M. Lutchyn, P. Krogstrup, R. Feidenhans, *et al.*, Physical Review B **93**, 155402 (2016).

[235] F. Nichele, A. C. C. Drachmann, A. M. Whiticar, E. C. T. OFarrell, H. J. Suominen, A. Fornieri, T. Wang, G. C. Gardner, C. Thomas, A. T. Hatke, *et al.*, Physical review letters **119**, 136803 (2017).

[236] J. Gooth, M. Borg, H. Schmid, V. Schaller, S. Wirths, K. Moselund, M. Luisier, S. Karg, and H. Riel, Nano letters **17**, 2596 (2017).

[237] A. M. Whiticar, A. Fornieri, E. C. T. O'Farrell, A. C. C. Drachmann, T. Wang, C. Thomas, S. Gronin, R. Kallaher, G. C. Gardner, M. J. Manfra, *et al.*, arXiv:1902.07085 (2019).

[238] C. Schrade and L. Fu, arXiv:1809.06370 (2018).

[239] A. Zazunov and R. Egger, Physical Review B **85**, 104514 (2012).

[240] A. Proutski, D. Laroche, B. van 't Hooft, P. Krogstrup, J. Nygård, L. P. Kouwenhoven, and A. Geresdi, arXiv:1901.10992 (2019).

[241] A. Paila, D. Gunnarsson, J. Sarkar, M. A. Sillanpää, and P. J. Hakonen, Physical Review B **80**, 144520 (2009).

[242] S. Plugge, A. Zazunov, P. Sodano, and R. Egger, Physical Review B **91**, 214507 (2015).

[243] Z. C. Shi, W. Wang, and X. X. Yi, New Journal of Physics **18**, 023005 (2016).

[244] F. R. Braakman, P. Barthelemy, C. Reichl, W. Wegscheider, and L. M. K. Vandersypen, Nature nanotechnology **8**, 432 (2013).

[245] T. A. Baart, T. Fujita, C. Reichl, W. Wegscheider, and L. M. K. Vandersypen, Nature nanotechnology **12**, 26 (2017).

[246] M. Leijnse and K. Flensberg, Physical review letters **107**, 210502 (2011).

[247] M. J. Rančić, S. Hoffman, C. Schrade, J. Klinovaja, and D. Loss, arXiv:1902.10251 (2019).

[248] S. Hoffman, D. Chevallier, D. Loss, and J. Klinovaja, Physical Review B **96**, 045440 (2017)

Acknowledgements

After reading all these chapters, I’m sure you’d love to know who helped me with this work. So, here I want to express my gratitude to the people that contributed to this thesis directly or indirectly, and to those who made QuTech the pleasant and inspiring research environment that I experienced it to be.

First of all Leo! Thank you for giving this fiftieth PhD student the opportunity to do research in your lab. I admire you for your scientific intuition, and ability to always ask questions getting to the heart of a problem. And, the freedom and responsibility you gave me over my projects, though challenging at first, I really liked. I wish you good luck with the new lab, and hopefully you’ll be braiding soon!

My PhD was a bumpy ride with many different projects, this gave me the luxury of working with and learning from many bright researchers. I started in the 2D-topo team with Fanming, Arjan, Stevan, Fokko, and David. Fanming, I‘ve gotten to know you as an imperturbable and efficient researcher, but above all as a really nice guy. Thank you for endlessly explaining the basics of 2DEG nanofabrication and measurements, and all the goodies you brought back from China. Arjan, thank you for teaching me about 2DEG physics. I’m glad to hear that you’re having fun at ASML, and that you’re making good use of your graduation gift. Stevan, although our overlap was short, I really liked our interactions. Your ability to breakdown a difficult research problem will no-doubt bring you nice results in your lab in Caltech. Fokko, it’s a shame we ended up in different projects. I enjoyed attending conferences together and our shared writing retreat. Your attention to the physical picture will make you a great scientist in Zürich! David, although a Bachelor project is short, you managed to get some nice results, well done! Also, thanks to our theory collaborators Michael and Rafal, and to our collaborators in Copenhagen and at HRL.

Moving from two to one dimension, I started working with InAs nanowires kindly provided by the group of Jesper Nygård and Peter Krogstrup in Copenhagen. Starting with the switching current project, I worked together with Alex and John. Despite your own convictions, Alex, you’re not at all difficult to work with. Tough, at times, it proved to be difficult keeping up with your lunch and coffee schedule. It’s very cool how you extended our work on Cooper-pair transistors to the microwave domain. And, I admire your never-failing efforts to organise and include everybody in social activities, including topo excursions and watching football matches at Proeflokaal. John, you’re very knowledgeable, and probably the hardest working and most organized person I know. As such, I wasn’t at all surprised that they wanted to hire you at Microsoft. Thank you for all your hard work on the switching current and fusion projects, and good luck hunting zero bias peaks! Regarding the switching current adventure, I’m also grateful for the valuable input of Attila, Torsten, Dima, and Roman.

The PhD journey continued with the fusion team with Damaz, Amrita, Nicolò, Luca, and John. These were tough times with lots of hard work without much output. I'd like to thank you all for keeping the spirit high, most of the time, and I'm pleased to see that we all found more rewarding projects by now. Amrita, with your vast experience you're the go-to person for all cleanroom problems. Nicolò, I'm glad to hear that you're doing well back in Italy. I'm honored that you're traveling to Delft for my defense. Luca, you were an ideal Master student who did not need much guidance. I remember being so proud when you stayed for a PhD, I'm sure you will do just as well as before! Damaz, it was great that we could move together to the dispersive readout team (we still should find a better name), and could work together with Wolfgang on gate-based readout for double quantum dots. I liked our morning coffees and conversations. Your unmatched desire to understand, record, and automatize stuff, be it measurements, your working hours, or computer games, puts you in the position to solve basically any problem. Wolfgang, I'd advise anyone to work with you. You're open to different research directions, and enthusiastic about small improvements without getting lost in details. Lin and Christian, I wish you all the best with the superconducting islands, and the next step in your careers (may they be located on real islands).

Besides those many direct colleagues, I had the pleasure to be surrounded by many more awesome people. In particular, thank you Önder for learning me the basics of nanowire physics during my Masters with your open, yet critical attitude. And, thank you for your hospitality during my visit to Boston this year. Kun, I much valued your kind advise at the beginning of my PhD, and hope you're finding your way in Japan. Srijit, thank you for being my fresh copromotor, who is always in for late-night dart sessions (provided we can find the darts). I learned a lot from you as a very passionate researcher and debater. Michiel, your careful reasoning and vast general knowledge makes your input very valuable to me. It was great fun to organize the best QTuitje ever with you and Jelmer, Ramiro, Lisanne, and Dan. Lastly, James, it's cool to see how your resonators are now such an important part of our lab. I'm looking forward to see you defending them in kilt.

Furthermore, I'd like to thank David, Vincent, Hao, Jie, Maja, Jouri, Willemijn, Francesco, Kevin, Dom, Daniël, Ting, Adriaan (Vuik), Christian, Jakob, Stijn, Tom, Daan, Elham, Roy, and all other members of the topo team for all your input and the pleasant research environment within topo. And, at the risk of forgetting someone, thanks to Toivo, Florian, Adriaan (Rol), Norbert, Peter, Stefan, Nodar, Suzanne, Udi, JP, Tim, Guoij and Nima from QuTech for all the nice interactions we had.

Essential for any good lab work is the support staff, and QuTech is fortunate to have an excellent team! Benningshof, thank you for keeping our fridges running. We also had a really great time together with Folkert and Udi in Göteborg. Jason, king of B013, thank you for creating (some) order in this room, and for all the handy lab tricks you taught me. And, thanks to Mark, Remco, Jelle, Bram, and Siebe for keeping a viable research environment by replacing gas bottles, filling helium dewars, fixing the cooling water system and much more! In particular, Mark thank you for your work on the UTS; too bad that the junctions did not make it to this thesis. Raymond, Raymond, and Marijn thank your with all your assistance with electronics. I liked your approach of trying to teach me something, rather than just providing an (ad-hoc) solution. I'd also like to thank the cleanroom staff. Without your work, my time in the cleanroom would have been a lot more painful. Jenny, Simone, Marja, Yuki, and Chantal, thank you for helping me with all kinds of forms, and for organizing summer BBQs and Christmas parties, maintaining the QT spirit within QuTech.

Lieven, Ronald, Leo DC, and other QuTech PIs, thank you for creating a great research environment. It has been really impressive to see QuTech evolve to its current size, and I'm looking forward to hearing about many cool discoveries. Ad, Sander, and Anton, thank you for giving me the opportunity to assist various courses.

Regarding the thesis part of my PhD, I want to thank the members of the committee for their time and energy to evaluate my thesis. And, John, Wolfgang, Fokko, Alex, Damaz, and Hanna for proofreading my thesis, and giving valuable input.

Familie en vrienden, bedankt voor jullie interesse in mijn onderzoek(sproces) en het helpen relativeren van teleurstellende resultaten. Ik wil in het bijzonder Lowin en Jip bedanken als mijn paranifmen en (Jip) voor het grafisch ontwerp. Louise, (co-co-copromotor) Piet, Inge, David, Jan en Jasper bedankt voor de gezellige weekenden binnen en buiten Bilthoven. En pap, mam, Lisanne, Marlijn, Pippo en Jasper, voor al jullie lieve, afleidende, voedzame en financiële ondersteuning. En pap en mam, die me altijd vrij hebben gelaten om te kiezen wat mij interesseerde.

De laatste woorden zijn voor jou, lieve Hanna. Het was super om de afgelopen jaren in hetzelfde gebouw te mogen werken. Dank voor je geduld tijdens alle avonden en weekenden die ik in de cleanroom en het lab heb doorgebracht. Dank ook voor je creativiteit, humor, en motivatie tijdens het schrijven van mijn proefschrift. Ik hoop dat ik jou over een jaar ook zo goed kan helpen. Ik kijk uit naar al onze avonturen in de toekomst te beginnen met twee super mooie reizen!

Curriculum Vitæ

Jasper VAN VEEN

25-02-1991	Born in Berkel en Rodenrijs, the Netherlands
2003–2009	Secondary school Sint Laurenscollege, Rotterdam
2009–2012	Bachelor in Applied Physics Delft University of Technology Thesis advisor: prof. dr. G. Steele
2013–2014	Internship Max Planck Institute for Solid State Research, Stüttgart Supervisor: dr. M. Ternes
2012–2015	Master in Applied Physics Delft University of Technology Thesis advisor: prof. dr. ir. L. P. Kouwenhoven
2015–2019	PhD research Delft University of Technology Promotor: prof. dr. ir. L. P. Kouwenhoven

List of Publications

10. **J. van Veen**, D. de Jong, L. Han, C. Prosko, P. Krogstrup, J. D. Watson L. P. Kouwenhoven, W. Pfaff, Revealing charge-tunneling processes between a quantum dot and a superconducting island through gate sensing, submitted (2019)

9. D. de Jong, **J. van Veen**, L. Binci, A. Singh, P. Krogstrup, L. P. Kouwenhoven, W. Pfaff, and J. D. Watson, Rapid detection of coherent tunneling in an InAs nanowire quantum dot through dispersive gate sensing, *Physical Review Applied* **11**, 044061 (2019)

8. **J. van Veen**, A. Proutski, T. Karzig, D. I. Pikulin, J. Nygård, P. Krogstrup, A. Geresdi, L. P. Kouwenhoven, and J. D. Watson, Magnetic-field-dependent quasiparticle dynamics of nanowire single-Cooper-pair transistors, *Physical Review B* **98**, 174502 (2018)

7. F. K. de Vries, T. Timmerman, V. P. Ostroukh, **J. van Veen**, A. J. A. Beukman, F. Qu, M. Wimmer, B-M. Nguyen, A. A. Kiselev, W. Yi, M. Sokolich, M. J. Manfra, C. M. Marcus, and L. P Kouwenhoven, h/e superconducting quantum interference through trivial edge states in InAs, *Physical Review Letters* **120**, 047702 (2018)

6. A. J. A. Beukman, F. K. de Vries, **J. van Veen**, R. Skolasinski, M. Wimmer, F. Qu, D. T. de Vries, B-M. Nguyen, W. Yi, A. A. Kiselev, M. Sokolich, M. J. Manfra, F. Nichele, C. M. Marcus, and L. P. Kouwenhoven, Spin-orbit interaction in a dual gated InAs/GaSb quantum well, *Physical Review B* **96**, 241401(R) (2017)

5. H. Zhang, Ö. Gül, S. Conesa-Boj, M. P. Nowak, M. Wimmer, K. Zuo, V. Mourik, F. K. de Vries, **J. van Veen**, M. W. A. de Moor, J. D. S. Bommer, D. J. van Woerkom, D. Car, S. R. Plissard, E. P. A. M. Bakkers, M. Quintero-Pérez, M. C. Cassidy, S. Koelling, S. Goswami, K. Watanabe, T. Taniguchi, and L. P. Kouwenhoven, Ballistic superconductivity in semiconductor nanowires, *Nature communications* **8**, 16025 (2017)

4. Ö. Gül, H. Zhang, F. K. de Vries, **J. van Veen**, K. Zuo, V. Mourik, S. Conesa-Boj, M. P. Nowak, D. J. Van Woerkom, M. Quintero-Pérez, M. C. Cassidy, A. Geresdi, S. Koelling, D. Car, S. R. Plissard, E. P. A. M. Bakkers, and L. P. Kouwenhoven, Hard superconducting gap in InSb nanowires, *Nano Letters* **17**, 2690-2696 (2017)

3. F. Qu, **J. van Veen**, F. K. de Vries, A. J. A Beukman, M. Wimmer, W. Yi, A. A. Kiselev, B-M. Nguyen, M. Sokolich, M. J. Manfra, F. Nichele, C. M. Marcus, and L. P. Kouwenhoven, Quantized conductance and large g-factor anisotropy in InSb quantum point contacts, *Nano Letters* **16**, 7509-7513 (2016)

2. B-M. Nguyen, A. A. Kiselev, R. Noah, W. Yi, F. Qu, A. J. A. Beukman, F. K. de Vries, **J. van Veen**, S. Nadj-Perge, L. P. Kouwenhoven, M. Kjaergaard, H. J. Suominen, F. Nichele, C. M. Marcus, M. J. Manfra, and M. Sokolich, Decoupling Edge Versus Bulk Conductance in the Trivial Regime of an InAs/GaSb Double Quantum Well Using Corbino Ring Geometry, *Physical Review Letters* **117**, 077701 (2016)

1. F. Nichele, H. J. Suominen, M. Kjaergaard, C. M. Marcus, E. Sajadi, J. A. Folk, F. Qu, A. J. A. Beukman, F. K. de Vries, **J. van Veen**, S. Nadj-Perge, L. P. Kouwenhoven, B-M. Nguyen, A. A. Kiselev, W. Yi, M. Sokolich, M. J. Manfra, E. M. Spanton, and K. A. Moler, Edge transport in the trivial phase of InAs/GaSb, *New Journal of Physics* **18**, 083005 (2016)